# FACULTY OF SCIENCE AND TECHNOLOGY

# MASTER'S THESIS

| | |
|---|---|
| Study programme / specialisation:<br>**MSc in Marine and Offshore Technology/ Marine and Subsea Technology** | The **spring** semester, **2023**<br><br>Open / ~~Confidential~~ |
| Author:<br>**Hassan Hasan Yousef** | ----------------------------<br>(Signature author) |
| Supervisor at UiS:<br>**Professor Yihan Xing**<br><br>Co-supervisor:<br>**Yucong Ma** | |
| Thesis title:<br>**Design and analysis of a hybrid timber-steel floating substructure for a 15 MW semisubmersible-type FWT** | |
| Credits (ECTS): **30** | |
| Keywords:<br>**Offshore Floating Wind Turbine**<br>**IEA Wind 15-MW FWT**<br>**Glued Laminated Timber**<br>**Finite Element Analysis**<br>**Design of Experiment**<br>**Response Surface Methodology** | Pages: 93<br>+ appendix: 18<br><br><br>Stavanger, **15th June, 2023** |

# Abstract

Wind energy has developed to be among the most promising sources of renewable energy. Furthermore, floating offshore wind turbines have presented the opportunity for higher power production in intermediate (45-150 m) and deep water ($> 150$ m). However, the manufacturing, installation, and operation of wind turbines in general, and floating wind turbines in particular, can result in significant amounts of greenhouse gas emissions (GHG).

This thesis proposes a novel design of a hybrid timber-steel floating substructure for the IEA 15 MW floating wind turbine. The new design presents a modified version of the UMaine VolturnUS-S semisubmersible platform that was initially developed for the same turbine. The main objective of the new design is to reduce the turbine's overall $CO_2$ footprint. This objective is achieved by replacing structural steel with glued laminated timber, a more sustainable material known for its environmental benefits.

Firstly, a robust design methodology is introduced. Secondly, Ansys workbench 2020 R1 is utilized to compare and then select between three preliminary hybrid timber-steel models based on a set of criteria that are extracted from relevant standards for both timber and steel. Compared to the UMaine VolturnUS-S semisubmersible platform, the selected hybrid configuration provides a considerable reduction in the steel mass (around 590 t). Subsequently, fully coupled aero-hydro-servo-elastic dynamic analysis is carried out using OpenFAST to validate the selected model. Only the ultimate limit state design (ULS) for the turbine under extreme and normal operating conditions is considered. The results from the numerical analysis show that the selected model fulfills all design criteria with a utilization factor that varies between 74-94% for the different design load cases. In the end, the work concludes that the glulam-based supporting structure offers an effective load-bearing solution for the IEA 15 MW turbine, contributing to the development of floating wind energy with minimal cost and $CO_2$ footprint. However, a series of tasks and suggestions are proposed to enhance the process of developing an optimal timber-steel design.

# Acknowledgment

# Publication

The following paper is written during the thesis:

Yousef, H. H., Xing, Y., Patel, K. S., & Ma, Y. (2023). A novel design of a hybrid glulam-steel substructure for the IEA 15-MW floating wind turbine. Fourth Conference of Computational Methods & Ocean Technology (CoTech 2023)

# Table of content

# List of Figures

# List of Tables

# Nomenclature

**Glued laminated Timber**

| Symbol | Description |
| --- | --- |
| $b$ [m] | Beam width |
| $E_{0,mean}$ [Mpa] | Mean value of the modulus of elasticity parallel to the grain |
| $E_{0,05}$ [Mpa] | Fifth percentile value of the modulus of elasticity parallel to the grain |
| $E_{90,mean}$ [Mpa] | Mean value of the modulus of elasticity perpendicular to the grain |
| $E_{90,05}$ [Mpa] | Fifth percentile value of the modulus of elasticity perpendicular to the grain |
| $f_{m,d}$ [Mpa] | Design bending strength |
| $f_{m,k}$ [Mpa] | Characteristic bending strength |
| $f_{m,j,k}$ [Mpa] | Characteristic bending strength of the finger joint |
| $f_{m,y,d}$ [Mpa] | Design bending strength about the principal y-axis |
| $f_{m,z,d}$ [Mpa] | Design bending strength about the principal z-axis |
| $f_{t,0,d}$ [Mpa] | Design tensile strength parallel to/along the grain |
| $f_{t,0,k}$ [Mpa] | Characteristic tensile strength parallel to/along the grain |
| $f_{t,0,|,k}$ [Mpa] | Characteristic tensile strength of the outer laminations |
| $f_{t,90,k}$ [Mpa] | Characteristic tensile strength perpendicular to the grain |
| $f_{c,0,d}$ [Mpa] | Design compressive strength parallel to/along the grain |
| $f_{c,0,k}$ [Mpa] | Characteristic compressive strength parallel to/along the grain |
| $f_{c,90,k}$ [Mpa] | Characteristic compressive strength perpendicular to the grain |
| $f_{v,k}$ [Mpa] | Characteristic shear strength |
| $f_{r,k}$ [Mpa] | Characteristic rolling shear strength |
| $G_{mean}$ [Mpa] | Mean value of the shear modulus |
| $G_{05}$ [Mpa] | Fifth percentile value of the shear modulus |
| $G_{r,mean}$ [Mpa] | Mean value of the rolling shear modulus |
| $G_{r,05}$ [Mpa] | Fifth percentile value of the rolling shear modulus |
| $h$ [m] | Beam depth |
| $k_{crit}$ | Factor used for lateral buckling |
| $k_{c,z}, k_z$ | Instability factors |
| $k_m$ | Factor considering re-distribution of bending stresses in a cross-section |
| $k_{mod}$ | Modification factor for the duration of load and moisture content |
| UF | beam's utilization factor |
| $X_d$ | Design value of a strength property |
| $X_k$ | Characteristic value of a strength property |
| $\gamma_m$ | Partial factor for material properties, also accounting for model uncertainties and dimensional variations |

| $\rho_k \ [\frac{kg^3}{m}]$ | Characteristic density |
| $\rho_{l,k} \ [\frac{kg^3}{m}]$ | Characteristic density of the laminations |
| $\rho_{mean}$ | Mean density |
| $\ell_{ef}$ | Effective length |
| $\lambda_{rel,m}$ | Relative slenderness for bending |
| $\lambda_{rel,z}$ | Relative slenderness ratio corresponding to bending about the z-axis |
| $\lambda_z$ | Slenderness ratio corresponding to bending about the z-axis |
| $\sigma_{c,0,d}$ [Mpa] | Design compressive stress along the grain |
| $\sigma_{t,0,d}$ [Mpa] | Design tensile stress along the grain |
| $\sigma_{m,crit}$ [Mpa] | Critical bending stress |
| $\sigma_{m,d}$ [Mpa] | Design bending stress |
| $\sigma_{m,y,d}$ [Mpa] | Design bending stress about the principal y-axis |
| $\sigma_{m,z,d}$ [Mpa] | Design bending stress about the principal z-axis |

**Aerodynamics**

| Symbol | Description |
| --- | --- |
| A $[m^2]$ | Rotor area |
| $C_D$ [-] | Drag coefficient |
| $C_L$ [-] | Lift coefficient |
| $C_Q$ [-] | Torque coefficient |
| $C_T$ [-] | Rotor thrust coefficient |
| D [N] | Drag force |
| $f$ [Hz] | Wind frequency |
| L [N] | Lift force |
| Q [N] | Moment force |
| $S_{uu} \ [\frac{(m/s)^2}{Hz}]$ | Kaimal wind energy spectrum |
| T [N] | Thrust force |
| V [m/s] | Free stream velocity |
| $\bar{V}$ [m/s] | Mean wind velocity |
| $V_{hub}$ [m/s] | Mean wind velocity at hub height |
| $\psi$ [deg] | Rotor azimuth angle |
| $L_k$ | Integral length scale |
| $\sigma_U$ | Wind standard deviation |
| $\rho \ [\frac{kg^3}{m}]$ | Air density |

**Hydrodynamics**

| Symbol | Description |
|---|---|
| $A_0 [m2]$ | Waterplane area of the floating structure |
| $A_k \left[\frac{N.s^2}{m}\right]$ | Added mass coefficient |
| $a \left[\frac{m}{s^2}\right]$ | Acceleration of a regular wave |
| $B, B_k$ [kg/s] | Damping coefficient |
| $C \left[\frac{N}{m}, N.m\right]$ | Restoring or stiffness coefficient |
| $C_a$ | Added mass coefficient in Morison equation |
| $C_D$ | Drag coefficient in Morison equation |
| $f \left[\frac{N}{m}\right]$ | Transverse force per unit length |
| $F_{excit}$ [N] | Excitation force |
| $F_k$ [N] | Dynamic force in general |
| $F_{rad}$ [N] | Radiation force |
| $g \left[\frac{m^2}{s}\right]$ | Gravitational acceleration constant |
| $H_{Mor} \left[\frac{N}{m^2}\right]$ | Transfer function of the Froude-Krylov and added mass forces per unit length |
| k | Indicator for the degree of freedom |
| $H_s [m]$ | Significant wave height |
| $m_n$ | Spectral moments for ($n = 0,1,2,..$) |
| $P_{FK} \left[\frac{N^2}{m}\right]$ | Froude-Kriloff pressure |
| $S(\omega) \left[\frac{m^2 s}{rad}\right]$ | Wave spectrum |
| $S_B$ | Mean wetted surface |
| $T_m [s]$ | Spectrum mean period |
| $T_z$ [s] | Mean zero crossing period |
| $u$ [m/s] | Transverse wave particle velocity |
| $v$ [m/s] | Local transverse body velocity |
| $z_{CoB}$ | Center of buoyancy z-coordinate |
| $X_k$ | Transfer function for the wave excitation force |
| $x_{CoG}$ | Center of gravity x-coordinate |
| $y_{CoG}$ | Center of gravity y-coordinate |
| $z_{CoG}$ | Center of gravity z-coordinate |
| $\zeta$ [m] | Instantaneous wave elevation |
| $\zeta_a$ [m] | Wave amplitude |
| $\eta$ [m, deg] | Translatory or rotation platform displacement |
| $\rho \left[\frac{kg}{m^3}\right]$ | Water density |

| | |
|---|---|
| $\phi_0 \ [\frac{m^2}{s}]$ | Velocity potential for a regular incident wave |
| $\phi_D \ [\frac{m^2}{s}]$ | Velocity potential of a diffracted wave |
| $\psi \ [\frac{m^2}{s}]$ | Complex velocity potential |
| $\omega$ [rad/s] | Frequency of incident waves or frequency of oscillation |
| $\epsilon_j$ [rad] | Phase shift |
| $\gamma$ | Peak shape parameter |

# Acronyms and Abbreviations

| Abbreviations | Full description |
|---|---|
| CEN | European Committee for Standardization |
| CIE | Carbon Intensity of Electricity |
| CoB | Center of Buoyancy |
| CoG | Center of Gravity |
| DLC | Design Load Case |
| DoE | Design of Experiment technique |
| DTU | Denmark Technical University |
| FWT | Floating Wind Turbine |
| IEA | International Energy Agency |
| GHG | Greenhouse Gas |
| GLULAM | Glued Laminated Timber |
| GWP | Global Warming Potential |
| LCA | Lifecycle Performance Assessment |
| NREL | National Renewable Energy Laboratory |
| RSM | Response Surface Methodology |
| SWL | Still Water Level |

# Chapter 1- Introduction

## 1.1 General Background

Climate change is a key challenge facing humanity today. Human activities, such as deforestation and fossil fuels use which release enormous amounts of greenhouse gases (GHG) into the atmosphere, are the major causes of climate change. These gases, especially CO2, trap heat and cause a considerable rising in the average temperature of Earth. This leads to a range of negative consequences including more frequent and severe heat waves, rising sea levels, and more frequent and extreme weather conditions.

Wind is an important energy source to mitigate climate change. By capturing wind power, wind turbines generate clean and sustainable energy without producing any kind of greenhouse gas emissions or any other pollutants. This is one of the reasons that make wind energy a key factor in any comprehensive plan aiming to combat climate change. Another reason is the fact that wind energy is becoming more cost-competitive with other energy sources, making it a desirable option for countries trying to transition to a greener energy future.

The development of larger wind turbines is becoming increasingly important to meet the rising demand for energy and to support the growing economy. The total extractable power available in wind can be calculated using Eq. (1.1) and is proportional to both the rotor swept area and the wind velocity cubed. This implies that doubling the wind velocity will give an eightfold increase in power output while doubling the rotor diameter will give four times increase in power output. As a result, a significant trend has emerged towards offshore wind turbines in recent years due to their high wind potential and consistent access to undisturbed wind (lower surface roughness). Moving offshore has enabled the possibility of increasing rotor radius, leading to higher power output. Additionally, moving offshore has solved a lot of the issues associated with large-scale land-based turbines such as transportation difficulties, potential noise, environmental concerns, and other public acceptance aspects such as aesthetics (Obhrai, 2022).

$$P = \frac{1}{2} \rho\, A\, U^3 \qquad\qquad (1.1)$$

Where $\rho$ is the air density, A is the rotor swept area, and U is the wind velocity.

The most common form of offshore wind platform is bottom fixed, which is the most common choice for up to 50 m water depth. However, for deeper water above 100-150 m, bottom fixed

wind turbines are no longer feasible due to technical and environmental considerations. Instead, wind turbines are usually carried over a floating base that allows the turbines to be easily relocated to different locations to open up new areas for wind energy development.

While Floating Wind Turbines (FWT) have become a popular choice for generating renewable energy, there are many challenges associated with their manufacturing, installation, and maintenance that must be addressed:

- Harsher environment loads on the foundations such as current, waves, wave breaking, and wave slamming
- More restrictions for marine operations posed by oceanic conditions such as wave heights and wind gusts
- Accessibility for maintenance activities is limited to periods when wave heights are below 1.5 m
- Corrosive and harsh environment
- Higher overall costs for constructing the foundations, installing the cabling, and connecting to the grid
- $CO_2$ footprint reduction

## 1.2 Objectives

The objectives of this thesis are to:

- Propose a new robust hybrid timber-steel floater design, see Figure 1.1, to support the IEA 15 MW reference wind turbine developed by International Energy Agency (IEA) (Gaertner et al., 2020). The new design aims to replace steel with glued laminated timber (glulam) and offers a modified version of the UMaine VolturnUS-S semisubmersible platform that was initially developed for the IEA 15 MW turbine.
- Provide a comprehensive design methodology.
- Provide a comprehensive evaluation of the structural performance of the hybrid floater using numerical simulations, thus contributing to the development of an innovative and environmental-friendly solution for offshore wind energy generation.
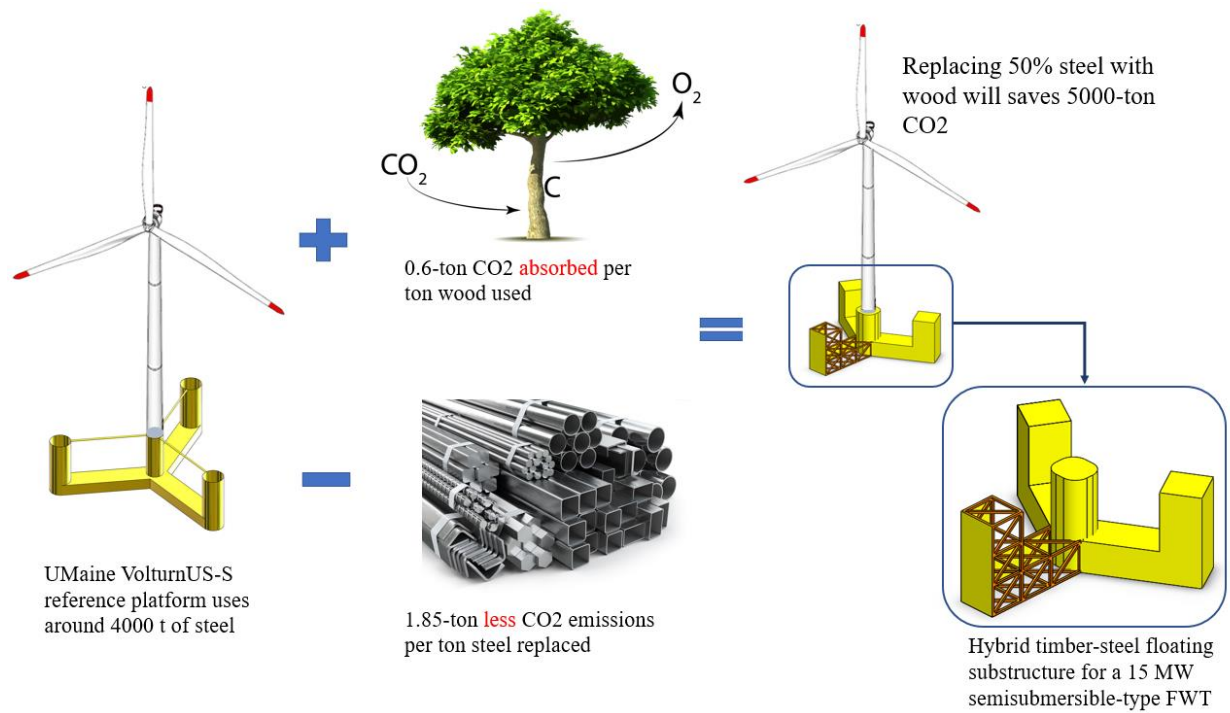
Figure 1.1: The environmental impact of using wood as a replacement for steel

Overall, the results of this thesis are represented to pave the way for further optimization work and to provide insights into the potential benefits and drawbacks of using glulam, thus helping to inform future decisions regarding material selection for similar floating structures.

## 1.3 Thesis Scope and Overview

To achieve the ultimate goals of this work, this study will limit its scope to the IEA 15 MW FWT with a focus on the global and local analysis of the system in its installed and operating conditions. The installation process will not be covered within the scope of this thesis. The analyzed system consists of sets of glulam beams and joints that are used to support the floater pontoons. This work will investigate the ultimate limit state of the beams only without neglecting the importance of the joints in deciding the total strength of the structure, especially for the serviceability limit state case.

To reduce the computational time, the columns of the floater are assumed to be rigid bodies and the focus will be merely on the pontoons. For the same reason, more restrictions are applied to the numbers of the models and the environmental loading cases that are covered in this thesis.

This work is divided into 8 chapters. The study starts by reviewing the existing literature on floating wind turbine and their environmental life cycle impact in Chapter 2. Chapter 2 gives a review of the existing literature on glulam before providing some basic knowledge about its

structure, production, types, strength classes, and mechanical properties. The chapter is ended with a brief introduction to the selected reference wind turbine and what kind of environmental loading is expected to act on such a wind turbine. Chapter 3 is the chapter where a systematic design procedure and all related standards and design criteria are introduced. In Chapter 4, a robust model of a glulam-based pontoon is selected based on a comparison between three proposed designs that are developed by the author using Ansys Workbench 2020 R1. In Chapter 5, the model's hydrodynamic properties are obtained. In chapter 6, a fully coupled aero-hydro-ealstic-servo analysis is carried out using OpenFAST. The results for different design load cases (DLC) are then employed for further local investigation/analysis in Chapter 7. Conclusions are summarized in Chapter 8, and although an optimal design is not identified, trends are captured and suggestions for further improvements are made.

# Chapter 2- Theoretical Background

## 2.1 Literature Review

Climate change and $CO_2$ emissions are among the most critical topics discussed in the Paris Agreement. Therefore, the establishment of offshore wind farms is strategically important to the European Union (European Commission, 2019, 2020a, 2020b, 2021). By 2050, offshore wind capacity is expected to reach 300 GW according to the EU Strategy of Offshore Renewable Energy (European Commission, 2020). Furthermore, projects in non-EU countries such as Norway and the United Kingdom can rise the total European offshore wind capacity close to 450 GW by 2050 (WindEurope, 2019). Around one-third of the continent's power demand can be met by this. In comparison, offshore wind capacity in Europe reached 25 GW by the end of 2020, accounting for around 3% of total power consumption (WindEurope, 2021).

Offshore wind turbines are divided into two types, bottom fixed turbines which are the most common form of offshore wind turbines in shallow water, and floating turbines which, to today's date, are still limited to a few pilot and demonstration projects (ETIPWind, (2020). Offshore wind turbines have enormous potential. According to the International Energy Agency (IEA), floating wind turbine contributes around 80% of offshore wind potential worldwide (International Energy Agency (IEA), 2019). The floating wind potential is around 336 000 TWh, which is 12 times more than the world power consumption in 2018. By 2050, it is expected that around one-third of the offshore capacity installed in Europe will be floating. The floating technology must be further developed and matured as a requirement for extending offshore wind energy from the shallow water of the North Sea to the rest of Europe, including far-from-shore places and deep-water regions. It also provides a significant export market for technology and solutions, as FWT is the only viable solution in some regions due to the large water depth.

The potential for floating turbines in European waters is predicted to be 4540 GW, with at least 3000 GW coming from seas and oceans with water depths ranging from 100 to 1000 m. The Baltic Sea and the North Sea have the most wind potential, but the Mediterranean Sea and the Atlantic Ocean also have prospects to benefit from wind energy (European Commission, 2020b). Europe's goals are lofty, with 450 GW of installed offshore wind power by 2050, at least 48 GW of which is planned for the Mediterranean (WindEurope, 2019). The Interreg-MED MAESTRALE project's website shows that the wind speeds in the Mediterranean region range from 3 to 7 m/s (Maestrale, 2022). The lower severity and frequency of extreme weather

conditions in the Mediterranean Sea compared to the North Sea and Atlantic Ocean implies that wind farms are less susceptible to damage, meaning lower investment risk and increased security. This is very important since offshore wind farms can be easily damaged in the presence of extreme weather conditions (Diamond, 2012; Kettle, 2020; Wang et al., 2019). In addition to that, the fact that floating wind turbines can be deployed in water depths ranging from 50 to 500 meters (Pantusa et al., 2020; Pantusa & Tomasicchio, 2019) makes the Mediterranean setting technically suited for wind energy utilization despite its high bathymetric slopes and deep seas along the shore (Chipindula et al., 2018; European Commission, 2020b; Staschus et al., 2020).

Being a very promising source of green energy doesn't negate the fact that floating wind turbines produce $CO_2$ and other greenhouse gas emissions throughout their lifecycles. Table 2.1 shows the values for the Global Warming Potential (GWP) (t $CO_2$ eq) of individual turbine components and the total for two types of floating wind turbines (raft-buoy and spar-buoy, 6 MW installed power, 154 m rotor diameter). These values were calculated as a part of a study aiming to evaluate the environmental performance of the two wind turbines. According to that study, raft buoys produce 12,242 t $CO_2$ eq (612 t $CO_2$ eq per year of operation), whereas spar buoys produce 15,118 t $CO_2$ eq (756 t $CO_2$ eq per year) over their lifetime, including the cables that connect them to the mainland (Pulselli et al., 2023).

Table 2.1: Life Cycle Analysis (LCA) of the two types of floating wind turbine (6 MW raft-buoy and 6 MW spar buoy) (Pulselli et al., 2023)

| Element | Technical Specification | Raft-Buoy turbine t CO$_2$eq | Raft-Buoy turbine% | Spar-Buoy turbine t CO$_2$eq | Spar-Buoy turbine% |
|---|---|---|---|---|---|
| **Phase 1—MANUFACTURING** | | | | | |
| Turbine and Floating structure | steel | 278.7 | 45.5% | 274.5 | 36.3% |
| | concrete | — | — | 33.8 | 4.5% |
| | fiberglass | 95.8 | 15.6% | 95.8 | 12.7% |
| | cast iron | 17.6 | 2.9% | 17.6 | 2.3% |
| | aluminium | 29.3 | 4.8% | 29.3 | 3.9% |
| | plastics | 9.5 | 1.5% | 9.5 | 1.3% |
| | other materials | 3.4 | 0.6% | 3.4 | 0.4% |
| | copper | 1.2 | 0.2% | 1.2 | 0.2% |
| | lead | 1.5 | 0.2% | 1.5 | 0.2% |
| | alkyd paint | 2.1 | 0.3% | 2.1 | 0.3% |
| | wood | 0.04 | 0.01% | 0.04 | 0.005% |
| | zinc | 1.0 | 0.2% | 1.0 | 0.1% |
| | epoxy | 0.3 | 0.04% | 0.3 | 0.03% |
| | rubber | 0.05 | 0.01% | 0.05 | 0.01% |
| Subtotal | | 440.3 | 71.9% | 469.9 | 62.2% |
| Anchor System | steel (chain) | 14.3 | 2.3% | 14.3 | 1.9% |
| | steel (drag anchor/suction pile) | 3.6 | 0.6% | 26.1 | 3.5% |
| Subtotal | | 17.8 | 2.9% | 40.4 | 5.3% |
| Submarine Power Cable (33 kV) | lead | 1.8 | 0.3% | 1.8 | 0.2% |
| | copper | 0.8 | 0.1% | 0.8 | 0.1% |
| | polyethylene (PE) | 0.6 | 0.1% | 0.6 | 0.1% |
| | steel | 3.4 | 0.5% | 3.4 | 0.4% |
| | polypropylene (PP) | 0.29 | 0.05% | 0.3 | 0.04% |
| Subtotal | | 6.9 | 1.1% | 6.9 | 0.9% |
| Total Phase 1 | | 465.1 | 76% | 517.2 | 68.4% |
| **Phase 2—TRANSPORT, ASSEMBLY and INSTALLATION** | | | | | |
| Generator | diesel | 0.5 | 0.1% | - | - |
| Crane | diesel | 0.8 | 0.1% | 0.8 | 0.1% |
| Forklift | diesel | 0.1 | 0.01% | 0.1 | 0.01% |
| Tugboat | diesel | - | - | 0.8 | 0.1% |
| Auxiliary boats | diesel | - | - | 0.4 | 0.05% |
| Transport (truck) | - | 43.3 | 7.1% | 132 | 17.5% |
| Transport (boat) | - | 1.1 | 0.2% | - | - |
| Total Phase 2 | | 45.8 | 7.5% | 134 | 17.7% |
| **Phase 3—MAINTENANCE and MATERIAL REPLACEMENT** | | | | | |
| Gearbox | cast iron | 2.6 | 0.4% | 2.6 | 0.4% |
| | steel | 2.2 | 0.4% | 2.2 | 0.3% |
| | rubber | 0.05 | 0.01% | 0.05 | 0.01% |
| Subtotal Phase 3 (materials) | | 4.9 | 0.8% | 4.9 | 0.7% |
| Transfer boat | diesel | 9.1 | 1.5% | 9.1 | 1.2% |
| FSV vessel | diesel | 49.7 | 8.1% | 49.7 | 6.6% |
| Helicopter | kerosene | 0.4 | 0.1% | 0.4 | 0.1% |
| Subtotal Phase 3 (energy) | | 59.2 | 9.7% | 59.2 | 7.8% |
| **Phase 4—END OF LIFE** | | | | | |
| Total Phase 4 | | 37.1 | 6.1% | 40.5 | 5.4% |

Figure 2.1 illustrates the study findings about the major sources of GHG emissions by life cycle phase and process. The manufacturing phase, which includes the anchoring system, material that comprise the turbines, and electric cables is the primary source of emissions: around 75% and 70 % for the raft-buoy (15.6% fiberglass and 49% steel) and spar-buoy (12.7% fiberglass and 42.1% steel), respectively. These numbers are in line with the results provided in the literature for other renewable energy sources, in which the fabrication and installation pre-dominates the impact (Sacchi et al., 2019). The manufacturing stage accounts for 81.5% of the entire impact of deep-water turbines (Chipindula et al., 2018). The obtained results also agree

with the results obtained by Raadal et al. (Raadal et al., 2014) who found that the turbine and platform/foundation materials contribute the most to overall GHG emissions (around 60- 80%). The mass balance primarily determines the difference between the two models: 4547 t for the raft buoy (83.7% steel) and 10,278 t for the spar buoy (39.3% steel and 53.5% cement). Materials such as rubble might be used instead of cement to minimize emissions released from the cement manufacturing process. The gasoline used by vessels (9.7% raft-buoy and 7.8% spar-buoy) to repair gearbox components is primarily responsible for maintenance emissions. For transportation and component assembly, fuel consumption is 7.5% and 17.7%, respectively (Pulselli et al., 2023).
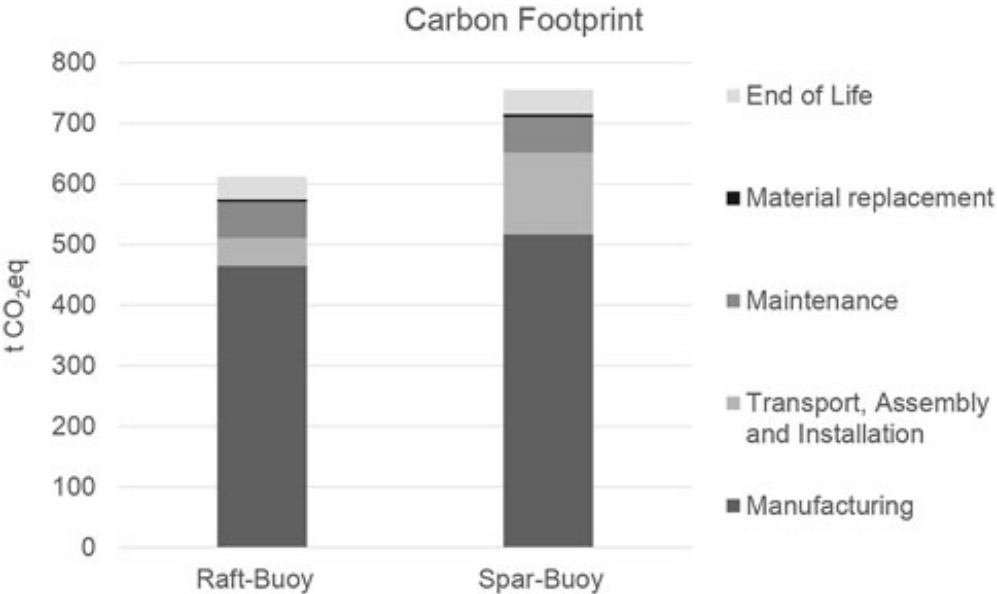


Figure 2.1: Carbon Footprint (t CO2eq) results of a 6 MW raft-buoy wind turbine and a 6 MW spar buoy wind turbine, concerning different LCA phases (Pulselli et al., 2023)

The study concluded that, compared to other renewable energy sources, floating wind turbines have good environmental performance. However, The Carbon Intensity of Electricity (CIE), which varies from 26.1 to 78.7 CO2eq/kWh1 for the studied turbines, is found to be highly dependent on the materials used during both the production and maintenance processes. The study highlights the need of developing better technologies to reduce the overall mass of steel to enhance environmental performance (Pulselli et al., 2023).

Wood/timber is one of the most ancient and complicated construction materials that can be used as a replacement for steel. By the turn of the last century, Otto Hetzer, a German structural design engineer, had filed a patent for "a bent structural component of timber for construction purposes," which became known as Glued Laminated Timber (Glulam). Glulam is a robust, stable, and corrosion-resistant material that combines economic sustainability with high

mechanical performance. In addition to all these impressive properties, glulam has the advantage of centuries of profound knowledge and extensive experience from the building and shipbuilding industries which have provided us with a better understanding of joint selection, wood limitations, and a faster yet safer method to construct and test wood products with (Porteous & Kermani, 2013). Based on that, this thesis aims to propose a new hybrid wood-steel design and illustrate that glulam can be a viable, sustainable, and cost-effective solution for the construction of any floating substructure. For this purpose, the UMaine VolturnUS-S semisubmersible platform that is used to support the IEA 15 MW FWT was selected. The selection of this platform/wind turbine was based on the fact that the IEA 15 MW with its publicly available design is a reference wind turbine that provides a solution that is applicable today as well as in the future. The IEA 15 MW outperforms the present generation of industrial wind turbines, but not so far that aggressive technological advancements are necessary (Gaertner et al., 2020).

Currently, the floating substructure uses around 4000 tons of steel due to its strength and durability (Allen et al., 2020). By replacing some of the structural steel with glulam, the turbine's overall carbon footprint can be reduced.

Figure 2.2 shows that all the technologies required to come up with such a hybrid design are already here. Figure 2.3 (a), on the other hand, shows the 18-storey Mjøstårnet building that was completed in 2019 to be the highest in the world which is made of glulam. Both glulam strength classes GL30c and GL30h were used for the structural design (Abrahamsen, 2017). Later in 2020, The first wooden wind power tower has been erected in Björkö (Sweden). The 30 m tower was erected by the development company Modvion (Modvion, 29 April 2020), see Figure 2.3 (b). In addition, two companies (Stora Enso, a biomaterials and wood construction firm, and Voodin Blade Technology GmbH, a German startup manufacturing wind turbine rotor blades) start recently collaborating to build wooden wind turbine blades as a replacement for heavier non-renewable wind turbine blades (Storaenso, 2022).
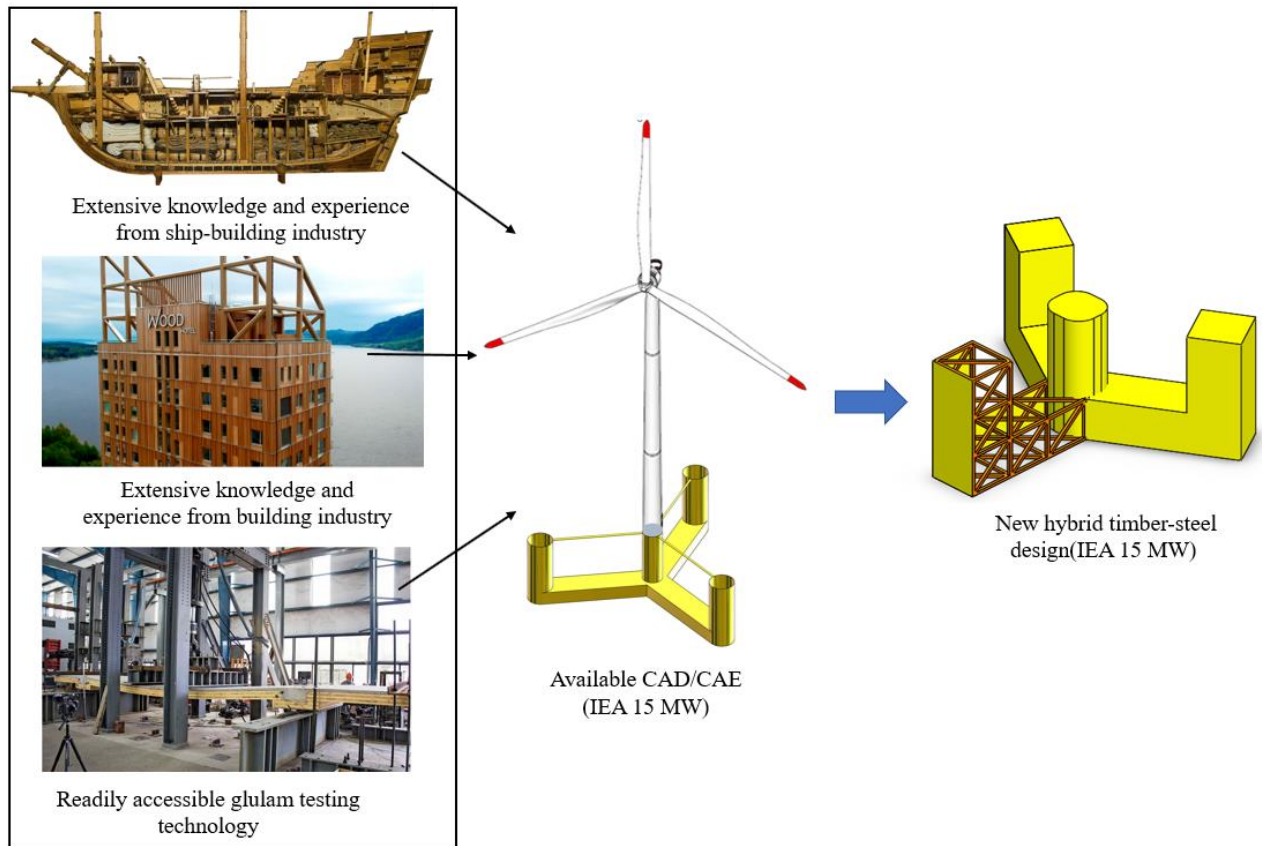
Figure 2.2: All the technologies required for the hybrid design are already available
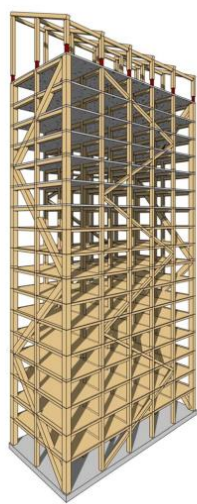


(a)                                                    (b)

Figure 2.3: Examples of wood construction; (a) Mjøstårnet building (Abrahamsen, 2017)
and (b) wooden wind turbine tower by Modvion (Modvion)

## 2.2 Glulam

The following sections provide a brief introduction to the structure of glued laminated timber, production, types, strength classes, and mechanical properties.

### 2.2.1 Introduction

Glulam is a type of laminated wood in which all of the boards are arranged parallel to the grain, see Figure 2.4. A rigid connection is established by gluing individual components, so-called lamellae over the entire contact surface with adhesives. The ability to homogenize wood as a construction material is a significant benefit of using glulam (Blaß & Sandhaas, 2017).
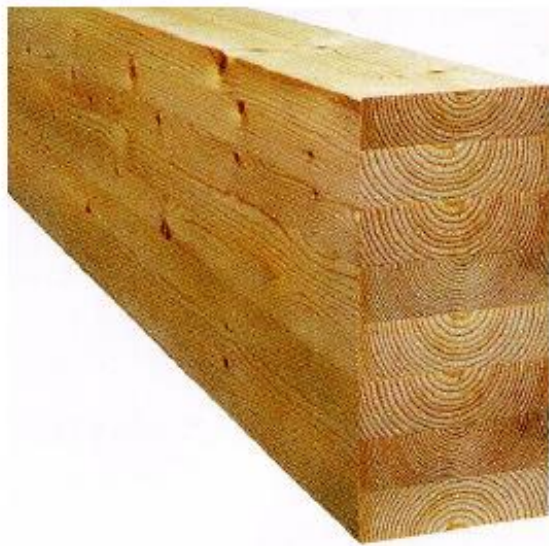


Figure 2.4: Glulam beam (Studiengemeinschaft Holzleimbau e.V., 1998)

The development of mildew-proof and waterproof synthetic resin adhesives has caused a significant increase in the development of glued timber constructions in timber engineering, making them an important material in the field of timber building. Unlike other load-bearing products like cross-laminated timber and sawn timber, Glulam allows for a larger cross-section, and therefore it is classified as an "engineered wood product" (Blaß & Sandhaas, 2017).

EN 14080 (European Committee for Standardization CEN, 2013) specifies the standards for glulam, including details of both strength class and manufacturing requirements. Guidelines are also established for each producer to manufacture its desired strength class, paving the path for particular lamella and finger-jointing qualities to be combined. In addition, EN 14080 established a new generation of European standards by integrating many distinct standards such as EN 385, EN 387, EN 390, EN 391, EN 392, and EN 1194. This implies that the restrictions

that were previously spread over many standards are now gathered together in one single standard (Blaß & Sandhaas, 2017).

## 2.2.2 Structure of glulam

The primary idea behind developing wood as a construction material and enhancing its competitiveness involves making it more homogenous and reducing the variation in its properties. When logs are utilized, the basic structure of the tree is often kept, making them stronger than sawn timber. This is because many fibers are removed during the processing.

Because wood has such a broad range of strength values, the strength of a board is defined by its weakest point, and the load-bearing capacity can only be altered by grading the logs or boards. In addition to grading, the wood properties can be improved by homogenization, where individual solid timber components are joined with one another using adhesive. If the wood components are even small fibers or particles, grading according to the strength of each component becomes impractical, and extensive homogenization is required during the manufacturing process.

Weak spots, such as knots, are less relevant inside the compound structure of a glulam beam since they no longer impact the total beam cross-section. Knotted regions have lower elastic modulus than wood above and below, exerting a force on the surrounding lamellae. The lamination effect refers to this systematic operation involving lamellae that are bonded together under pressure. Because the variation in mechanical properties in the bonded material is lower than in individual lamellae, gluing and dissecting the wood prepares the way for homogenization. Elements like pitch pockets, larger knots, and bark in-growth are eliminated. This indicates that removing a defective portion from a piece of timber must be classified according to DIN 4074 in S10. Figure 2.5, depicts a representation of how a knot region is eliminated, followed by finger-jointing to make a longboard. Boards ranging from 3 to 6 m long are often finger-jointed to produce an endless lamella during glulam production (Blaß & Sandhaas, 2017).
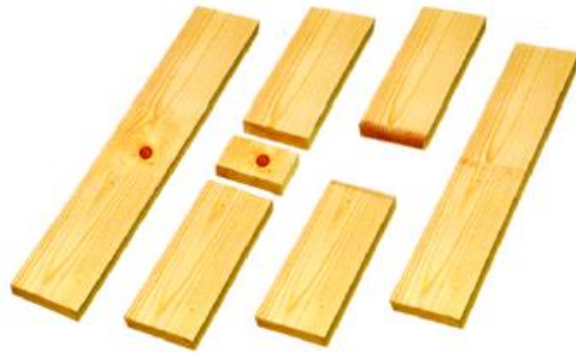
Figure 2.5: The process of knot-region removal followed by finger-jointing
(Studiengemeinschaft Holzleimbau e.V., 1998)

Glulam offers an additional advantage over squared wood. Big and pith shrinkage cracks are common in squared timber with a large cross-section, see Figure 2.6. These cracks allow wood pests or moisture to penetrate easily and limit the potential applications of wood. The kiln-drying of large cross-sections can pose a particular challenge when lengthy sections are involved. On the other hand, drying individual boards of glulam is very easy and any deformations that occur during the drying can be planned off in the manufacturing process, see Figure 2.7.



Figure 2.6: Glulam compared to squared timber with cracks (Studiengemeinschaft
Holzleimbau e.V., 1998)
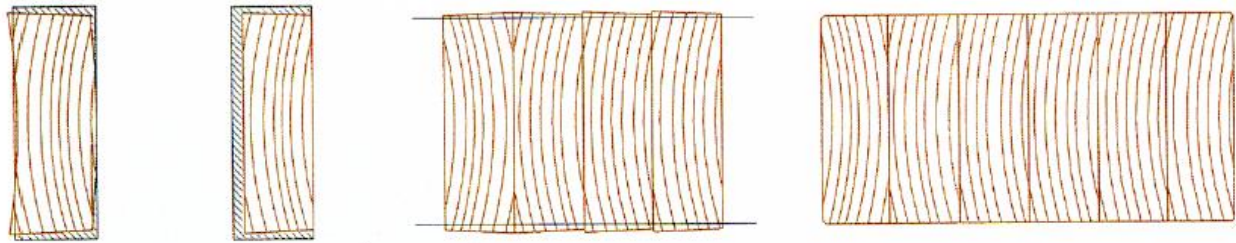
Figure 2.7: The sequence related to the transformation of a board from left to right. The board experiences shrinkage deformation as it dries. The board is planned on its large sides to create parallel areas for bonding. Gluing, the board becomes a glulam cross-section. Finally, the glulam cross-section is planned and chamfered, with only the right sides being externally exposed (Studiengemeinschaft Holzleimbau e.V., 1998)

Figure 2.6 and Figure 2.7 illustrate different principles of glulam production. According to the EN 14080 standard (European Committee for Standardization CEN, 2013), the piths of the glulam should be on the same side. However, for service class 3, the surfaces of the glulam must always be on the right sides facing the pith. As a result, the lower lamellae form a left-on-left side bond, as shown on the right side of Figure 2.6. This bonding arrangement helps in the prevention of shrinkage cracks on the glulam surface during severe weather conditions. This is because the left side of the wood experiences greater tangential shrinkage, making it more prone to cracking. The behavior of the lamellae or finished glulam cross-sections during shrinkage and subsequent processing is detailed in Figure 2.7.

With rising lamellae thickness, the risk of cracking caused by fluctuating humidity increases, and it becomes increasingly difficult to deliver the requisite pressing strength in the glue line. EN 14080 establishes limit values for lamellae cross-sections for these reasons. The maximum thickness of glulam shall be 45 mm for straight members that are not exposed to high and alternating environmental stress. However, board thicknesses less than 35 mm are suggested for members exposed to rapidly changing conditions. The board can be fitted with a relief groove in the longitudinal direction to reduce the stresses inside the board as a result of fluctuating humidity and to prevent any tendency towards warping. The end grain of the boards should be maintained properly since glulam wood sections might split due to high humidity fluctuation. Furthermore, it is also important to manage and control the humidity of the members during storage, transit, and assemble. Any further norms and requirements should be referred to EN 14080 (Blaß & Sandhaas, 2017; European Committee for Standardization CEN, 2013).

## 2.2.3 Production

A wide variety of wood species can be used to make glulam, however, spruce is nearly always (up to 95%) the first option in Germany (Blaß & Sandhaas, 2017). The usage of larch, beech, fir, Douglas fir, and pine is minimal, although the glulam made from Douglas fir and larch is appropriate when additional durability is required. The main stages in glulam production are shown in Figure 2.8 (Glulam Beams) and include:

- First, the boards are pre-graded
- Then, the boards are dried
- Strength-grading of the boards
- "Continuous lamellae" are generated via finger jointing
- Continuous lamellae are capped to the desired length
- Planing the lamellae
- Adhesive is applied
- Inserting and pressing into a pressing jig
- Planning to the final member size
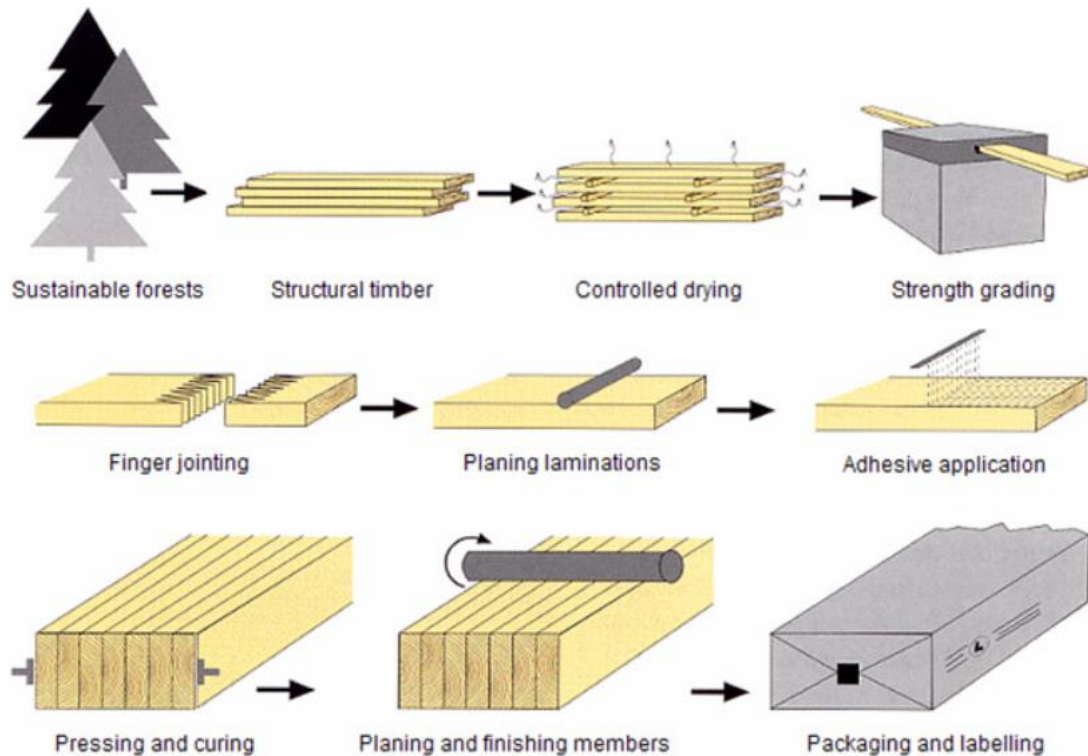


Figure 2.8: Production of glulam beams (Glulam Beams)

To manufacture glued load-bearing wood members, experienced personnel with specialized equipment are needed. Additionally, there are specific requirements that must be fulfilled, such as having covered and air-conditioned working areas, reliable measurement devices to check the moisture content in wood, an annex for kiln-drying, machines for processing adhesive surface and board ends for which butt joints are intended, devices to apply the glue and the necessary pressing force, etc.

The sawn timber used to make glulam is stored and usually kiln-dried. To avoid further shrinkage cracks, the moisture content for glue should be set at a level that corresponds to the average predicted moisture content in construction. The moisture concentration should be adjusted lower than the average moisture concentration because the tension stress perpendicular to the grain while shrinking causes more damage than compressive stress perpendicular to the grain while swelling. The boards are dried to a moisture level of around 10% (± 2%) prior to processing when used indoors. This moisture content is in the range of the equilibrium moisture content that the boards will have when installed. Maintaining this level of moisture content usually prevents additional detrimental shrinkage and helps minimize cracking. During the ordinary drying of sawn timber, the unavoidable drying stresses must be minimized to prevent the glue line from warping and splitting up. The wood is pre-planed before grading. The grading is done visually or by machine. Quality control also includes removing any boards that are overly dry or wet and sending them to be reconditioned. The mechanical and optical properties of glulam boards vary greatly. When it comes to making premium glulam beams, classification into categories (mechanical and visual) and minimizing undesirable natural wood traits are also essential. Following gluing and finger-jointing, the last step of the process comprises planning and chamfering, where the required cross-section is reached. This is followed by cutting to length, cosmetic repairs, packaging, and delivery (Blaß & Sandhaas, 2017).

## 2.2.4 Glulam Types

Figure 2.9 illustrates the difference between horizontally laminated glulam with one or multiple adjacent lamellae as specified by EN 14080 (European Committee for Standardization CEN, 2013). Alternatively, many thin glulam members (block-glued glulam) are bound together to produce a single broader element.

Glulam beams are well-suited to take bending stresses in load-bearing structures, which means that the major forces acting on the outer lamellae are tensile or compressive forces. This is why a variety of cross-section compositions with different strength classes of lamellae are usually

used, see Figure 2.10. In this situation, a difference is established between combined and homogeneous glulam (e.g., GL24c and GL24h, respectively). All of the lamellae in homogeneous glulam are boards of a certain strength class. The center lamellae of combined glulam may have a lower strength class as compared to the outer lamellae. This combined glulam configuration can be symmetrical or asymmetrical. The outer lamellae of larger glulam beams must have at least two lamellae, whereas smaller cross-sections with up to ten lamellae must have one lamellae at least. A combination may include several wood types. This is attractive when lower grade and therefore less expensive wood is considered. However, the different boards must be placed correctly in the manufacturing process, making hybrid and combined glulam production more expensive. Appropriate installation on the construction site must be assured with a label for asymmetrical cross-sections. This is especially true for the glulam members as shown in Figure 2.11. If the exterior lamellae are cut, as is done for tapered beams and three-hinged frames, special care must be given to combined glulam systems. This is because lamellae of the lower strength class tend to "shift" in the outside area (Blaß & Sandhaas, 2017).
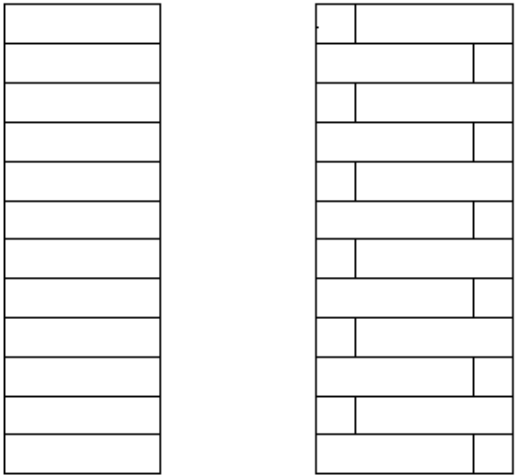


Figure 2.9: Horizontally laminated glulam with one lamellae (on left) and multiple adjacent lamellae (on right)  (Blaß & Sandhaas, 2017)
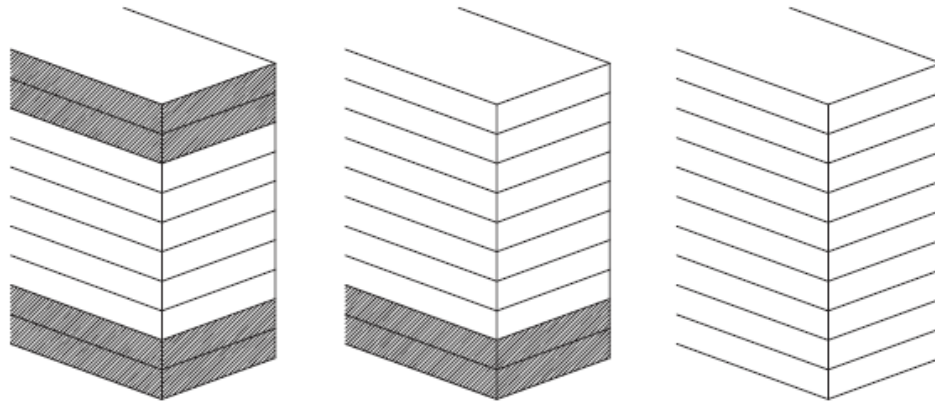
Figure 2.10:: Symmetrical, asymmetrical combined, and homogenous glued laminated timber, from left to right (Blaß & Sandhaas, 2017)
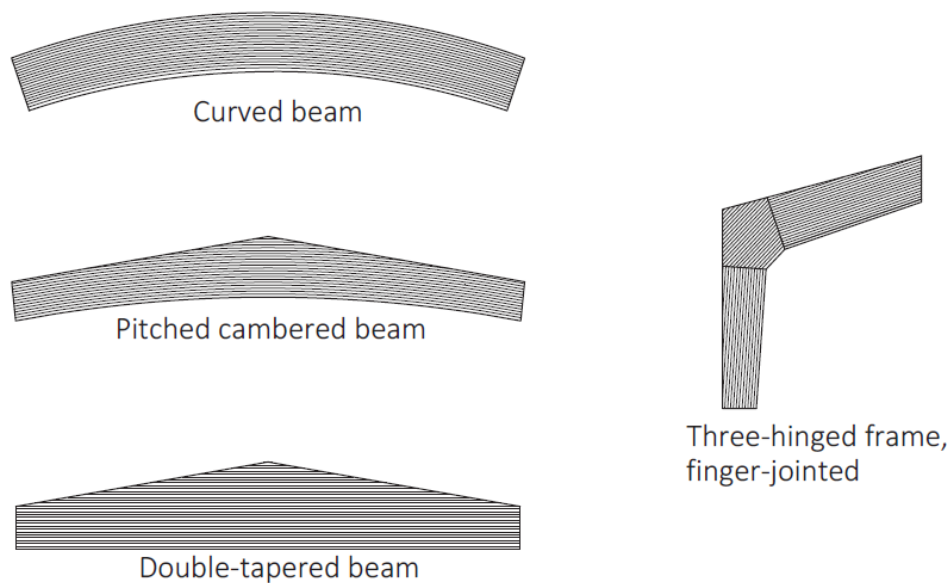


Figure 2.11: Special constructed glulam elements (Blaß & Sandhaas, 2017)

## 2.2.5 Parameters influencing the strength of glulam

This section represents information about specific parameters influencing the bending strength of the glulam members, which is primarily employed in structures that are subjected to bending stress. The following section will discuss other strength properties.

Colling and Frese showed that the strength of glulam members is influenced by the strength of finger joints and boards (Colling, 1990; Frese, 2006). When it is subjected to stresses, a glulam beam will move to reduce the stress as quickly as possible, leading to breakage. The breakage tends to occur in areas where there is a high stress-to-strength ratio such as a finger joint or a board section with knots. The failure of glulam members due to finger joints is mainly due to poor or low-quality finger joints, whereas the members with substandard planks are prone to

damage in knot regions. Therefore, achieving high-quality glulam requires a thorough consideration/examination of all the components included such as finger joints and boards. Reinforcing only one of these components is not practical since the total load-bearing capacity of the beam will ultimately be decided by the weakest component, making it impossible to fully exploit any targeted strength improvement. From the aforementioned information, the following conclusions can be drawn (Blaß & Sandhaas, 2017):

- The load-bearing capacity of glulam members cannot be improved by visual grading with stringer knot criteria for boards. This is because lowering the permitted knot degree will increase the board strength only without taking into account the strength of the involved finger joints. As a result, the finger joints are progressively triggering the failure of glulam members, preventing the full exploitation of the increased board strength.

- The strength of both finger joints and boards can be improved by applying strength grading based on the elastic modulus and/or density of the wood, resulting in stronger glulam. As a result, for high-strength glulam, the machine-strength grading of the boards is very crucial.

- It is very important to monitor the quality of the finger joints to ensure adequate strength since they are exposed to a variety of production conditions (such as the pressing power applied, the age of the adhesives, or climatic conditions in the production spaces). This becomes even more important because production-related factors are interconnected and often very difficult to manage or regulate.

## 2.2.6 Background to the CEN provisions

The mechanical properties of homogeneous glulam, depending on the finger-jointing and board properties, are calculated using the equations given in EN 14080 (European Committee for Standardization CEN, 2013).

Table 2.2 lists the valid equations for homogeneous glulam for several essential properties, while for combined glulam, they are used to calculate the properties of the different cross-sectional parts. The equations are based on a reference volume of 0.01 $m^3$ for beams exposed to tensile stresses perpendicular to the grain and on members having a height (width) of 600 mm for tension members/bending beams. In this situation, the volume effect is used to account for the fact that the strength of a brittle material decreases with increasing member size (Blaß & Sandhaas, 2017).

Table 2.2: Mechanical properties of glulam (European Committee for Standardization CEN, 2013)

| Property | Equation |
|---|---|
| Bending strength | $f_{m,k} = -2.2 + 2.5f_{t,0,\|,k}^{0.75} + 1.5\left(\dfrac{f_{m,j,k}}{1.4} - f_{t,0,\|,k} + 6\right)^{0.65}$ <br><br> if $1.4f_{t,0,\|,k}+ \leq f_{m,j,k} \leq 1.4f_{t,0,\|,k} + 12$ |
| Tensile strength | |
| ▪ parallel to the grain | $f_{t,0,k} = 0.8f_{m,j,k}$ |
| ▪ perpendicular to the grain | $f_{t,90,k} = 0.5$ |
| Compressive strength | |
| ▪ parallel to the grain | $f_{c,0,k} = f_{m,j,k}$ |
| ▪ perpendicular to the grain | $f_{c,90,k} = 2.5$ |
| Shear strength | $f_{v,k} = 3.5$ |
| Rolling shear strength | $f_{r,k} = 1.2$ |
| MOE parallel to the grain | $E_{0,mean} = 1.05E_{t,0,\|,mean}$ |
| MOE perpendicular | $E_{90,mean} = 300$ |
| Shear modulus | $G_{mean} = 650$ |
| Rolling shear modulus | $G_{r,mean} = 65$ |
| Density | $\rho_k = 1.1\rho_{\|,k}$ |

An empirical relationship based on testing and numerical research has been established to demonstrate how the bending strength of glulam depends on the bending strength of the finger joints and the tensile strength of lamellae. The increase in bending strength of glulam as compared to the tensile strength of the lamellae is caused by a number of lamination phenomena, some of which are highlighted below:

- During a standard tensile test, the load-bearing behavior of a board varies from that of a glulam member. The EN 408 tensile strength test procedure specifies a minimum test length and there is no lateral support for the test specimens. As a result, knots or areas with asymmetrical density distribution can result in lateral deformations which lead to additional bending moments and reduce the board's tensile strength. However, the boards in a glulam beam are held together by bonded neighboring lamellae, meaning that the boards in a glulam beam may have higher tensile strength than the ones tested using a free tensile test.

- The lamellae are bonded together and that allows lower-stiffness areas to transmit forces to adjacent lamellae with greater rigidity. This implies that, for example, the strain of board sections with knots can be reduced, resulting in an improvement in tensile strength.

The inclusion of individual lamellae in the structure of glulam results in a more homogeneous material with less variation in associated density. As a result, the characteristic density values given for glulam are higher as compared to individual lamellae.

## 2.2.7 Strength classes

Table 2.3 represents the strength classes for homogenous glulam according to EN 14080 (European Committee for Standardization CEN, 2013).

Table 2.3: Strength classes for homogeneous glulam according to EN 14080 (European Committee for Standardization CEN, 2013)

| Property | GL20h | GL22h | GL24h | GL26h | GL28h | GL30h | GL32h |
|---|---|---|---|---|---|---|---|
| $f_{m,k}$ | 20 | 22 | 24 | 26 | 28 | 30 | 32 |
| $f_{t,0,k}$ | 16 | 17.6 | 19.2 | 20.8 | 22.3 | 24 | 25.6 |
| $f_{t,90,k}$ | | | | 0.5 | | | |
| $f_{c,0,k}$ | 20 | 22 | 24 | 26 | 28 | 30 | 32 |
| $f_{c,90,k}$ | | | | 2.5 | | | |
| $f_{v,k}$ | | | | 3.5 | | | |
| $f_{r,k}$ | | | | 1.2 | | | |
| $E_{0,mean}$ | 8400 | 10500 | 11500 | 12100 | 12600 | 13600 | 14200 |
| $E_{0,05}$ | 7000 | 8800 | 9600 | 10100 | 10500 | 11300 | 11800 |
| $E_{90,mean}$ | | | | 300 | | | |
| $E_{90,05}$ | | | | 250 | | | |
| $G_{mean}$ | | | | 650 | | | |
| $G_{05}$ | | | | 540 | | | |
| $G_{r,mean}$ | | | | 65 | | | |
| $G_{r,05}$ | | | | 54 | | | |
| $\rho_k$ | 340 | 370 | 385 | 405 | 425 | 430 | 440 |
| $\rho_{mean}$ | 370 | 410 | 420 | 445 | 460 | 480 | 490 |

## 2.2.8 The advantages of using glulam instead of steel

As mentioned earlier, glulam is a robust, stable, and corrosion-resistant material that outperforms steel in many aspects. Some of the advantages of using glulam instead of steel are listed below:

**Reduced CO2 emissions /Enhanced sustainability**

Steel accounts for around 7% of global $CO_2$ emissions (World Steel Association, 2016), and shifting away from these emission-intensive materials will have a substantial influence on decreasing the overall carbon footprint of the floating wind turbines.

In comparison with other construction materials, wood has a considerable advantage since it is a renewable resource. This advantage can be seen during the formation of biomass (such as leaves or wood), for example, when oxygen is released into the atmosphere, carbon is absorbed into the biomass, and $CO_2$ is removed from the air via a process called photosynthesis. Because of this, timber is regarded as a $CO_2$-neutral structural material, and the only time the same amount of $CO_2$ is emitted as was initially captured is when biomass degrades, such as when the wood is burnt or rots. As a result, timber constructions absorb and accumulate $CO_2$ during their entire lifecycle which makes timber the only truly renewable construction material. It is assumed that one cubic meter of wood can sequestrate an average of 0.8 to 0.9 tonnes of $CO_2$ (Buchanan, 2007). A further advantage is that wood processing requires far less primary energy than processing other materials since wood grows naturally and is considerably easier to work with than metals like steel or aluminum, which must be manufactured. The ratio of primary energy needed to generate one cubic meter of construction material from different raw materials is shown in Figure 2.12 (Blaß & Sandhaas, 2017).
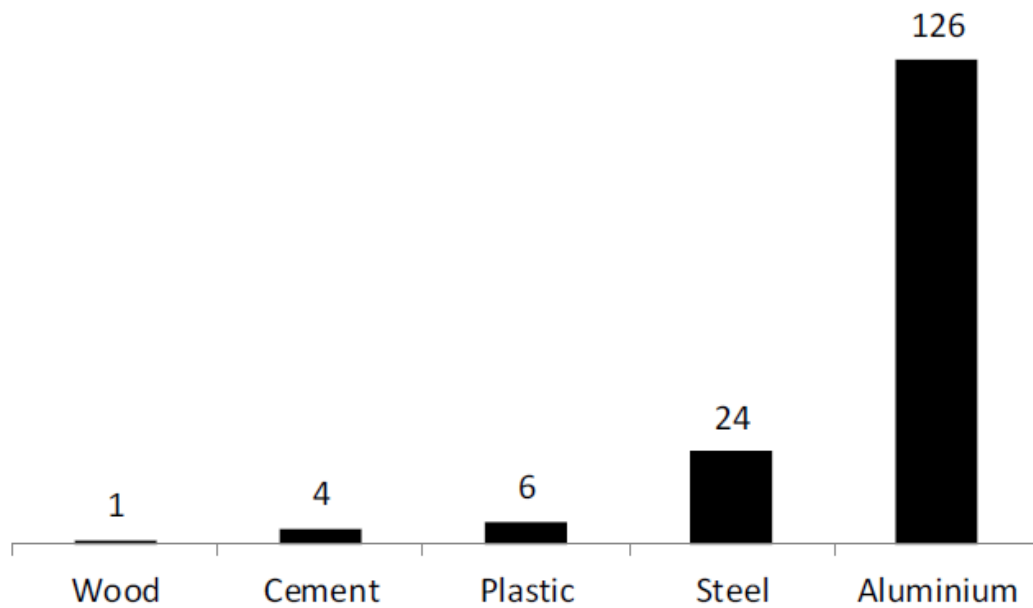
Figure 2.12: The ratio of primary energy consumption necessary to generate a cubic meter of building material from various raw materials (Blaß & Sandhaas, 2017)

**Reduced weight**

Glulam is stronger than steel for the same weight. Weight is a crucial factor since larger constructions must be designed to support both their own weight and other external loads. Strengthening requires additional material, which raises the cost.

**Cost/time reduction**

Mass wood materials are not cheap. However, they do provide many advantages in terms of cost-effectiveness. For instance, the weight of columns, beams, and panels made of mass wood is usually around one-fifth of that of steel and concrete, which results in lower transportation costs and requires less workforce for installation. In addition, construction time may be shortened by up to 25% when prefabricated panels are supplied directly to project sites, saving owners even more time and money (C.D. Smith Construction, 2021).

**Produced in Europe**

Modern practices of forestry present a continuous process of cultivating, harvesting, and replanting wood. This practice provides a sustainable source for mass timber construction. To ensure the sustainability of the forest, the harvest is performed in such a way that only alternate trees are chopped down, allowing the rest of the trees to grow twice as tall and not compete for natural resources. Furthermore, the practice of planting many saplings for every tree cut ensures

the growth and availability of forest resources in the future. This is especially true in the case of Norway and Scandinavia where mass timber is widely produced from the sustainable Scandinavian forests. Scandinavian woods are among the finest maintained in the world, with replanting and environmental concerns being prioritized (C.D. Smith Construction, 2021; Glulam Beams).

**Prefabrication possibility**

This makes the construction process quicker and more cost-effective.

**Availability and flexibility**

Glulam is available in a wide range of widths and heights.

**Other physical properties**

In addition, wood outperforms steel in terms of other physical characteristics. For instance, wood has lower heat conductivity (0.13 and 0.20 W/(mK) compared to 60 W/(mK) for steel (Blaß & Sandhaas, 2017).

## 2.3 Loads on Offshore Wind Turbine

There is a wide range of environmental loads that act on offshore wind turbines, see Figure 2.13. The wind and wave loads are the most dominant environmental loads. Therefore, It seems reasonable to perform the coupled dynamic analysis of the offshore wind turbine under wind and wave loads only. Other loads, shown in Figure 2.13, are deemed minor compared to wind and waves and therefore are neglected.
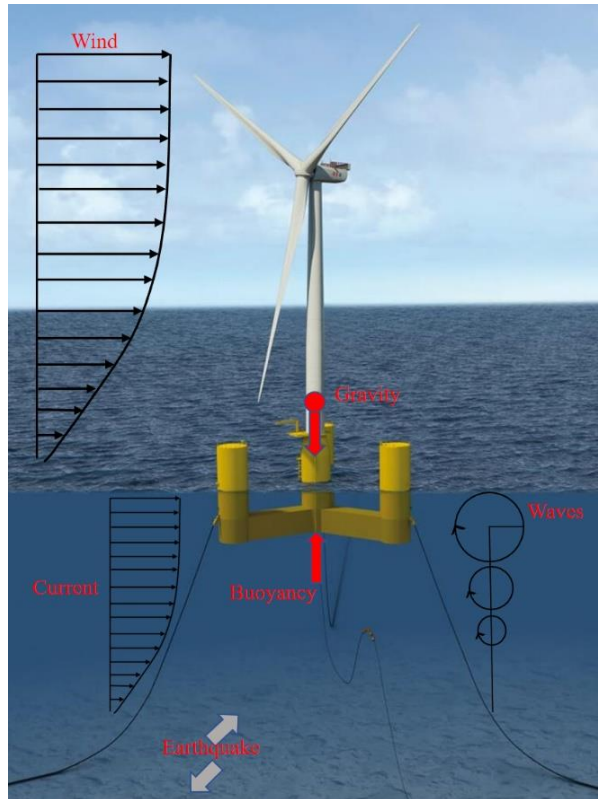
Figure 2.13: Overview of Offshore Wind Turbine Loads

## 2.3.1 Aerodynamic load

Large wind turbines have usually very flexible and light components due to economic considerations. Flexible and light components induce vibration and oscillation, which must be accounted for in the dynamic load analysis. An aerodynamic simulation evaluates the dynamic loads on a wind turbine by combining aerodynamic calculations with elastic deformations. The current section provides information on how aerodynamic theory and structural dynamics are included in the calculation process (Crozier, 2011).

**<u>Aerodynamics</u>**

Integrating the pressure distribution on the surface yields the overall forces produced by an airfoil. As shown in Figure 2.14, the aerodynamic forces are divided into two components: lift force, which is normal to the wind direction, and drag force, which is parallel to the wind direction. Lift and drag are often described as non-dimensional forces, see Eq. (2.1) and Eq. (2.2) (Manwell et al., 2010).

$$C_L = \frac{L}{\frac{1}{2} \rho A V^2} \qquad (2.1)$$

$$C_D = \frac{D}{\frac{1}{2}\rho A V^2} \qquad (2.2)$$

where $C_L$ is the lift coefficient, $C_D$ is the drag coefficient, $A$ is the rotor swept area, $\rho$ is the density of air and $V$ is the velocity of the free stream.
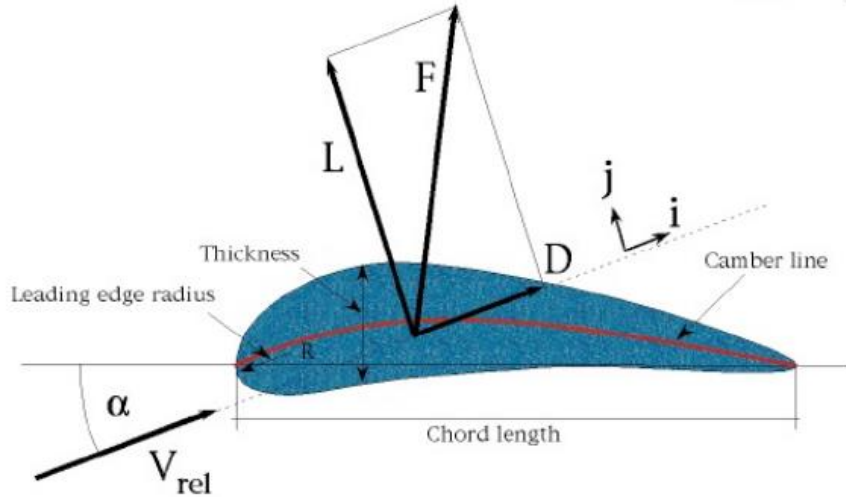


Figure 2.14: Forces on airfoil (Krogstad, 2010)

The pressure distribution, and hence the drag and lift forces experienced by the turbine blades, are defined by the airfoil's shape. The angle of attack $\alpha$, defined as the angle between chord length and wind direction, shows a linear relationship with the lift force and also specifies the point at which the stall effect occurs for a fixed shape. The lift force causes the turbine to rotate, whereas the thrust on the turbine is due to the drag force. Manwell expressed the moment force Q and thrust force T as a function of their corresponding coefficients in Eq. (2.3) and Eq. (2.4) (Manwell et al., 2010).

$$Q = \frac{1}{2}C_Q\, \rho A V^2 \qquad (2.3)$$

$$T = \frac{1}{2}C_T\, \rho A V^2 \qquad (2.4)$$

The aerodynamic calculation procedure is divided into two phases: first, calculating steady effects, and second, calculating unsteady effects. The most popular approach for calculating the steady effects of the aerodynamic forces is the blade element momentum (BEM) approach. The BEM approach is not discussed in detail in this thesis. However, more details can be found in (Manwell et al., 2010). In general, scale model testing, computational fluid dynamics (CFD), or panel approach are used to construct the curves, and the BEM approach uses these curves to

look up steady-state lift and drag coefficients for uniform airflow. Aerodynamic solvers enhance the BEM technique by utilizing a dynamic stall model that reproduces the drag and lift transients created by vortex shedding to incorporate crucial unsteady flow features like the stall phenomenon (Manwell et al., 2010).

## Structural flexibility

Modal and finite element analyses are two methodologies for dealing with structural flexibility. The modal analysis approach calculates the deflection of the structure's flexible parts using limited degrees of freedom. The modal shapes, which correspond to the element's natural frequencies, are combined linearly to generate the deflection. The number of natural frequencies used in the analysis determines the number of modes and the accuracy. As a result, the modal representation is less precise than the FE analysis, which is based on a direct numerical calculation of the deflections in each time step. Detailed information on both analysis methods can be found in (Dowling, 2007).

## Periodic force

The coordinate system for the turbine tower, rotor, and blades is shown in Figure 2.15 (Froeyd, 2009). The coordinate system of the blade is twisted over the span of the blade, with a maximum twist at the blade root and zero twists at the blade tip. Normal and parallel to the blade chord at the tip are the flap-wise and edgewise directions. When there is no movement of the blade around the z-axis, the edgewise blade direction relates to the rotor's in-plane direction, and the flap-wise direction relates to the out-of-plane rotor direction. The tower moves in two directions: forward-aft and side-to-side. Yaw is the angle of misalignment between the turbine shaft and the incoming wind direction.
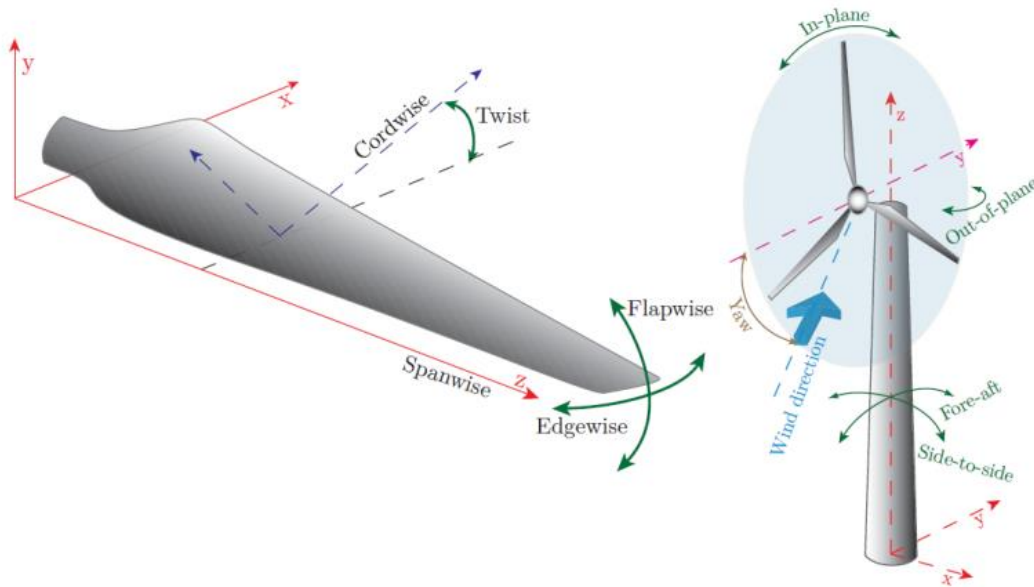
Figure 2.15: The coordinate system of the tower, rotor, and blade (Froeyd, 2009)

Because of the rotor's orientation, the loads on a wind turbine are periodic and driven by gravitational and aerodynamic forces. The oscillation induced by the time-varying loads is proportional to the rotor speed and rotor speed frequency, also known as 1P. The turbine blade will encounter a 1P periodic excitation force when traveling through the swept rotor region. Because three blades pass the tower within the same time interval, the rotor-tower excitation will have a 3P periodic loading. Some sections of the wind turbine experience other loads as a result of dynamic interactions due to periodic loads. For example, yaw motion may result in considerable gyroscopic moments in the turbine's reaction (Crozier, 2011). Below is a discussion of the gravitational load as well as the impacts on aerodynamic load caused by wind shear, shaft tilt, yaw error, and tower shading.

**Gravitational loads**

The weight of the turbine blade, which creates an edgewise bending moment at the blade's root as it sweeps over the rotor region, is the source of the gravitational load. The root edgewise moment is a function of the blade's azimuth angle $\psi$ in the in-plane rotation, and it results in a completely sinusoidal load with frequency 1P. In theory, there should be no induced gravitational load on the turbine shaft for a perfectly balanced three-bladed wind turbine operating in steady wind because each blade experiences its maximum root edgewise moment at a rotor azimuth angle of $\pm 90$ and zero root edgewise moment when pointing upwards or downwards.

**Wind shear load**

The boundary layer above the land, or the ocean surface for offshore wind turbines, causes wind shear, which is characterized by an increase in wind speed with height. The power law in Eq. (2.5) describes the wind profile, where $\alpha$ is recommended to be taken 0.14 for offshore wind turbines, according to the IEC 61400-3 standard (International Electrotechnical Commission (IEC), 2009).

$$V(z) = V_{hub} \left( \frac{z}{z_{hub}} \right)^{\alpha} \tag{2.5}$$

Figure 2.16 depicts the wind shear impact on aerodynamic loading, which may be characterized as an increase in local wind speed when the blades are oriented upwards vs downwards. This will cause a 1P cyclic loading on each blade and a 3P cyclic loading on the tower. Because of the non-linear form of the velocity profile generated by wind shear, the loading profile will not be entirely sinusoidal.
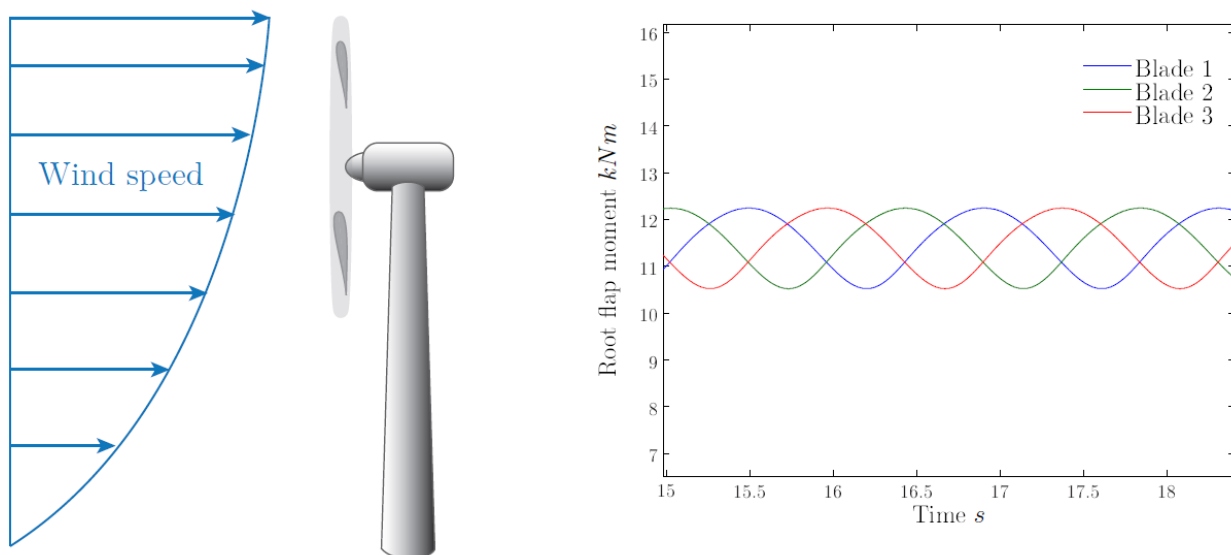


Figure 2.16: Wind shear Loading (Froeyd, 2009)

**Shaft tilt load**

The term "shaft tilt" describes the permanent mismatch between the wind velocity angle and the rotor disk, which is necessary to prevent any interference between the tower and blades during heavy loading. The impact on aerodynamic loading is the same as the impact of wind shear discussed earlier.

**Tower shadow load**

The tower shadow effect describes the alteration in the uniform flow of wind, and hence the aerodynamic loading, caused by the presence of the tower behind the rotor-swept area, see Figure 2.17. The blade of an upwind turbine experiences minimum wind each time it passes through the location directly in front of the tower. For a three-bladed wind turbine, each of the blades experiences minimum wind in one complete rotation and hence tower shadow contributes to the 3P effect.
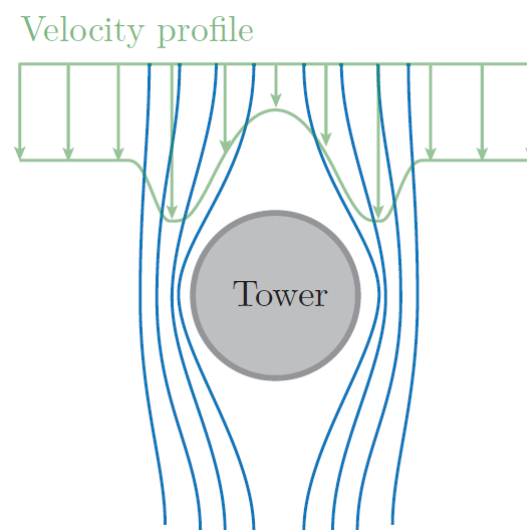


Figure 2.17: Tower shadow effect (Froeyd, 2009)

**Yaw error load**

In wind turbines, the yaw mechanism aligns the wind turbine rotor with the wind direction to enhance efficiency and avoid skewed wind inflow, which can cause torsional loading on the tower. The wind direction can vary quickly, yet the nacelle and rotor have high yaw inertia, therefore yaw motion must be restricted to avoid significant gyroscopic loadings that can contribute to the total aerodynamic loading on the tower.

**<u>Randomly fluctuating forces</u>**

Wind turbines are also subject to other randomly fluctuating aerodynamic loads caused by gust, turbulence, and dynamic effects in addition to the steady and periodic aerodynamic loads mentioned earlier. Turbulence is defined as a random variation of wind velocity in both time and space around a mean value. Turbulence varies a lot in intensity and the estimated lifetime of a wind turbine depends on the loads experienced by its blades, which are often the primary source of fatigue. Gust is the most dominating load in extreme wind conditions and is defined

as sudden changes in wind speed and direction over a short period (3–20 s) that can cause large, transient loads on wind turbine blades and other components.

**<u>Kaimal wind spectrum</u>**

According to IEC and DNV standards, it is recommended to use the Kaimal spectrum to represent wind conditions:

$$S_{uu}(f) = \frac{\sigma_U{}^2(\frac{4L_k}{\bar{V}})}{(1 + \frac{6fL_k}{\bar{V}})^{\frac{5}{3}}} \tag{2.6}$$

Where $f$ is the wind frequency, $\sigma_U$ is the wind standard deviation, $\bar{V}$ is the mean wind velocity and $L_k$ is an integral length scale that is taken as Eq. (2.7) unless the data given indicate otherwise.

$$L_k = \begin{cases} 5.67z & \text{for } z < 60\,m \\ 340.2 & \text{for } z \geq 60\,m \end{cases} \tag{2.7}$$

## 2.3.2 Hydrodynamic loads

It is very complex and challenging to represent the actual sea surface. Therefore, regular wave representation and linear wave theory is widely used in many kinds of literature, see (Faltinsen, 1993; Newman, 1977). Linear wave theory shows that the amplitudes of the wave-induced loads and motions are proportional to the amplitude of the incident waves. The frequency domain analysis of the FWT in irregular seas is done by the superposition of an infinite number of regular waves with different amplitudes, phases, and periods.

Many assumptions are made when linearizing the hydrodynamic load on floating structures. Although it is assumed that the mechanisms causing the motions are linear, non-linear effects will still exist. Slow-drift excitation and sum frequency associated with the second or higher-order effects are neglected when computing hydrodynamic loadings and, thus, are not covered in this section. However, detailed information about non-linear effects is provided in (Faltinsen, 1993; Jonkman & Sclavounos, 2006).

**<u>Sea state representation</u>**

Regular wave theory, also known as Airy wave theory, can be applied when the amplitude of the wave is much smaller than the wavelength. This theory is based on simple wave kinematics.

However, a good representation of the sea state can be obtained by superposing several regular wave components into what is called a wave spectrum. The wave spectrum and the important parameters derived from it are represented in this section. However, before that, a short overview of the equations that govern regular wave theory is given.

**Regular wave theory**

Regular wave theory is derived based on the assumption that the seabed is completely horizontal and the free surface extends infinitely in the horizontal direction. To determine the governing equations for the finite and infinite water depth cases, potential flow theory is applied. Potential flow theory assumes that seawater is homogeneous, continuous, incompressible, and inviscid and that its flow is irrotational. Based on this theory, the water velocity $\vec{V}(x, y, z, t) = (u, v, w)$ for the infinite depth case can be obtained from the velocity potential $\emptyset_0$ given in:

$$\emptyset_0 = \frac{g\zeta_a}{\omega} e^{kz} \cos(\omega t - kx) = \Re\{\psi_0(x, y, z)\, e^{i\omega t}\} \tag{2.8}$$

Here $g$ is the gravitational acceleration, $\zeta_a$ is the wave amplitude, $\omega$ is the wave frequency, $k$ is the wave number and $\psi_0$ is the complex velocity potential. $k, \omega$ can be determined using Eq. (2.9) and Eq. (2.10) and are related through the deep water dispersion relationship represented in Eq.(2.11).

$$\omega = \frac{2\pi}{T} \tag{2.9}$$

$$k = \frac{2\pi}{\lambda} \tag{2.10}$$

$$k = \frac{\omega^2}{g} \tag{2.11}$$

Where $T, \lambda$ are the wave period and the wavelength, respectively. Based on Eq. (2.11) we can write:

$$\lambda = 1.56\, T^2 \tag{2.12}$$

The instantaneous elevation of an incoming regular wave propagating in the positive x-direction and infinite water depth can generally be given as (Faltinsen, 1993):

$$\zeta(t) = \zeta_a \sin(\omega t - kx) \tag{2.13}$$

The dynamic loads can be calculated by integrating the dynamic pressure over the mean wetted surface ($S_B$).

$$\vec{F}_k(t) = -\int_{S_B} \rho \frac{\partial \emptyset}{\partial t} \vec{n}_k ds \tag{2.14}$$

Where $\vec{n}_k$ is the normal unit vector taken as $\vec{n}_k$ with $k = 1,2,3$ to obtain surge, sway, and heave forces, respectively. To obtain the moments, $\vec{n}_k$ is taken as $(\vec{n} \times \vec{r})$ when $k = 4,5,6$ corresponds to roll, pitch, and yaw moments.

**Irregular wave theory**

The instantaneous elevation of a long-crested irregular wave can be taken as the sum of an infinite number of regular waves $j$ with different frequencies $\omega_j$ and phase shifts $\epsilon_j$:

$$\zeta(t) = \sum_{j=1}^{N} A_j \sin(\omega_j t - k_j x + \epsilon_j) \tag{2.15}$$

Where $A_j$ is the amplitude of the $j^{\text{th}}$ wave and can be obtained from the wave spectrum which provides a mathematical representation of wave energy distribution over the range of wave frequencies. The correlation between wave spectrum $S(\omega)$ and its amplitudes and frequencies are given by Eq. (2.16) :

$$\frac{1}{2}A_j{}^2 = S(\omega)\Delta\omega \tag{2.16}$$

Based on (Van Der Tempel, 2006), Table 2.4 gives a list of characteristic parameters determined based on the relation between the wave elevation time series and wave spectrum. For instance, the significant wave height $H_s$ in the spectrum is defined as the average of the highest one-third of waves in the time series, which is equal to four times the standard deviation $\sigma$. The standard deviation can be calculated from the zero spectral moments. The mean zero crossing period can also be derived from the spectral moments.

Table 2.4: Definition of some wave characteristic parameters

| Parameter | Description |
|---|---|
| Spectral moments for ($n = 0,1,2,..$) | $m_n = \int_0^\infty \omega^n S(\omega) d\omega$ |
| Standard deviation | $\sigma = \sqrt{m_0}$ |
| Significant wave height | $H_s = 4\sigma$ |
| Spectrum mean period | $T_m = 2\pi \sqrt{\dfrac{m_0}{m_1}}$ |
| Mean zero crossing period | $T_z = 2\pi \sqrt{\dfrac{m_0}{m_2}}$ |

To represent the statistical distribution of wave energy for a sea state, it is recommended to use spectral density functions such as modified Pierson-Moscowitz or JONSWAP spectra. These spectra are based on Gaussian and Rayleigh distributions.

The modified Pierson-Moscowitz spectrum, as shown in Eq. (2.17) (Faltinsen, 1993), is obtained from measurements taken in the Atlantic Ocean. This spectrum is recommended by the International Towing Tank Conference (ITTC) and the International Ship Structures Committee (ISSC) to describe the wave elevation for a fully developed sea at an infinite fetch. To use the spectrum, two inputs are needed: the significant wave height, $H_s$, and the mean wave period, $T_m$.

$$\frac{S(\omega)}{H_s^2 T_m} = \frac{0.11}{2\pi} (\frac{\omega T_m}{2\pi})^{-5} exp\left[-0.44(\frac{\omega T_m}{2\pi})^{-4}\right] \tag{2.17}$$

On the other hand, the JONSWAP spectrum is a modified version of the Pierson-Moscowitz spectrum that is recommended by the 17th ITTC to account for sea states that are not fully developed under a particular wind condition. The JONSWAP spectrum has a narrower peak compared to the Pierson-Moscowitz spectrum, and its shape is defined by the peak shape parameter $\gamma$ which is usually taken as 3.3. When the $\gamma$ parameter is equal to 1, the JONSWAP spectrum is identical to the Pierson-Moscowitz spectrum. Eq. (2.18) describes the JONSWAP spectrum, which is valid for limited fetch (Faltinsen, 1993).

$$S(\omega) = 155 \frac{H_s^2}{T_m^4 \omega^5} \exp\left(\frac{-944}{T_m^4 \omega^4}\right) \gamma^r \tag{2.18}$$

$$r = \exp\left(-\left(\frac{0.191\omega T_m - 1}{2^{0.5}\sigma}\right)^2\right)$$

$$\sigma = \begin{cases} 0.07 & \text{For } \omega \leq \dfrac{5.24}{T_m} \\ 0.09 & \text{For } \omega > \dfrac{5.24}{T_m} \end{cases}$$

**Linear hydrodynamic**

Figure 2.18 illustrates the coordinate system and motions of the studied FWT. The translation displacement is given as $\eta_1$, $\eta_2$ and $\eta_3$ (i.e., surge, sway and heave). The rotational motion about the x, y, and z axes can be given as $\eta_4$, $\eta_5$ and $\eta_6$ (i.e., roll, pitch and yaw). The translation displacements of the floater are considered to be small in comparison to the size of the floater. This simplifies the hydrodynamic load analysis by separating it into two different loads: scattering and radiation. The scattering load consists of the excitation loads from the waves, i.e. Froude-Kriloff (FK) and diffraction forces and moments. The radiation force is independent of the incident waves and includes added mass and damping, see (Faltinsen, 1993).
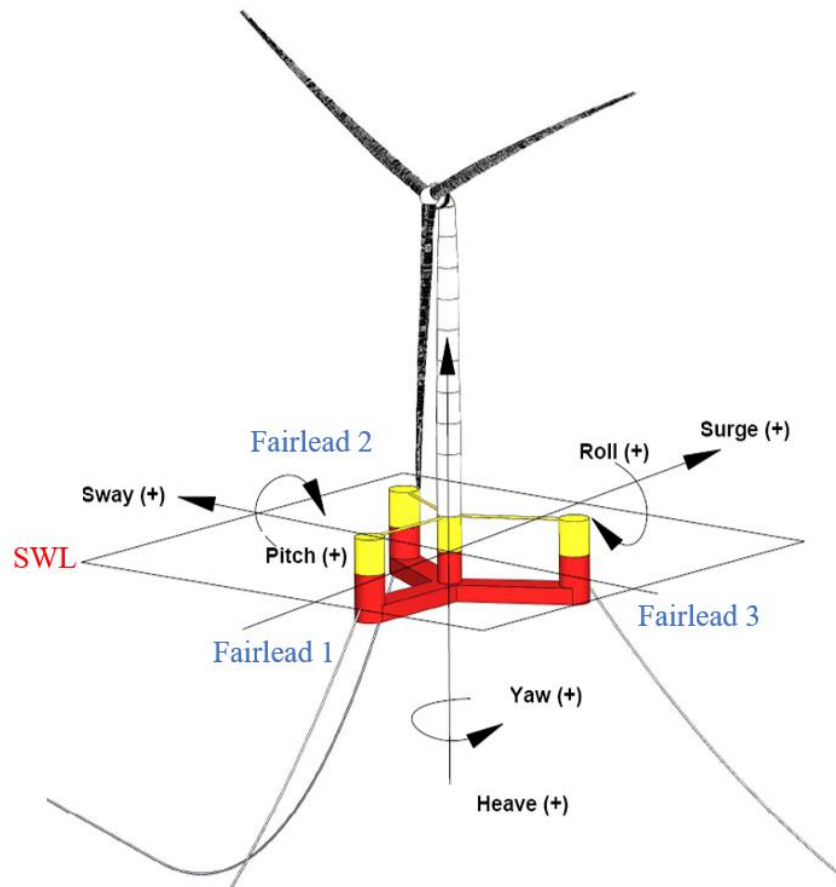


Figure 2.18: Coordinate system and modes of system motions (Gaertner et al., 2020)

**Scattering load**

When there are regular incident waves, scattering loads are the forces and moments on the turbine floater when it is restrained from oscillating. The total wave excitation loads are composed of FK and diffraction forces. The FK force is associated with an undisturbed pressure field in the presence of incident waves. For infinite water depth, the undisturbed FK pressure is written as:

$$P_{FK} = \rho \frac{\partial \emptyset_0}{\partial t} = \rho g \zeta_a \sin (\omega t - kx) \tag{2.19}$$

For this case, the presence of the structure has no effect on the velocities and pressure around it, so the forces will be the same as on a water volume of the same shape. According to (Faltinsen, 1993), the horizontal FK force acting on a structure strip is given as:

$$d\vec{F} = \vec{i} \rho \pi R^2 dz \, a_1|_{x=0} \tag{2.20}$$

Where $a_1|_{x=0}$ is the fluid acceleration in the x-direction at x = 0. There is no contribution to the horizontal force from the phase $\sin(\omega t)$, and thus is ignored.

In practice, the undisturbed pressure field does not exist, so a diffraction force causes changes in the pressure field. The velocity potential can be used to represent the total wave excitation loads, see Eq. (2.21) and Eq.(2.23) (Faltinsen, 1993).

$$\emptyset = \emptyset_0 + \emptyset_D \tag{2.21}$$

Where $\emptyset$, $\emptyset_0$ and $\emptyset_D$ are the velocity potential of the scattered, incident, and diffracted waves, respectively.

$$\frac{\partial \emptyset_D}{\partial n} = -\frac{\partial \emptyset_0}{\partial n} \tag{2.22}$$

The total wave excitation force is given by integrating Eq. (2.22)

$$\vec{F}_{exc,k}(t) = -\int_{S_B} \rho \frac{\partial \emptyset_0}{\partial t} \vec{n}_k ds - \int_{S_B} \rho \frac{\partial \emptyset_D}{\partial t} \vec{n}_k ds \tag{2.23}$$

The first term represents the FK force, and the second represents the diffraction force. When using frequency domain analysis, the total excitation force is presented more conveniently in a complex form, see Eq. (2.24) (Faltinsen, 1993).

$$\vec{F}_{exc,k}(t) = \Re\left\{-\int_{S_B} \vec{\imath}\omega e^{i\omega t}\rho(\psi_0 + \psi_D)\vec{n}_k ds\right\} = \zeta_a\Re\{X_k(\omega)\} \qquad (2.24)$$

Where $|X_k(\omega,\beta)| = |F_{exc,k}|/\zeta_a$ is the transfer function for the wave excitation force in the direction $\beta$.

**Radiation force**

When there are no incident waves, the structure is forced to oscillate with the wave frequency, resulting in added mass and damping loads. The oscillatory motion of the structure in its six degrees of freedom is given as (Faltinsen, 1993):

$$\eta_k(t) = \eta_k\cos(\omega t) = \Re\{\eta_k e^{i\omega t}\} \qquad (2.25)$$

Where $\eta_k$ is the amplitude of oscillation in the $k^{th}$ degree of freedom. Outgoing waves develop when the structure oscillates. The radiation velocity potential in the complex notation can be given as (Faltinsen, 1993):

$$\psi_R = \Re\left\{\sum_{k=1}^{6} \dot{\eta}_k\,\psi_k\right\} \qquad (2.26)$$

When the structure is forced to oscillate with the wave excitation frequency, fluid particles around the structure start to oscillate, and the corresponding radiation force in matrix form can be given as (Faltinsen, 1993):

$$F_{k,rad}(t) = \sum_{k=1}^{6}\{-A_k\ddot{\eta}_k - B_k\dot{\eta}_k\} \qquad (2.27)$$

Where $A_k$ and $B_k$ are the $(6\times6)$ added mass and damping matrices. Only the diagonal elements have non-zero coefficients when the forward speed is zero and no current is present. The relation between added mass and damping coefficient is given by (Faltinsen, 1993):

$$A_k - \frac{i}{\omega}B_k = \rho\int_{S_B} n_k\psi_k ds \qquad (2.28)$$

**Haskind relation**

The Haskind relation provides the link between diffraction and radiation force. It allows us to calculate the total excitation force using the radiation velocity potential rather than the diffraction velocity potential (Faltinsen, 1993). The excitation force can be given as:

$$\vec{F}_{exc,k}(t) = \Re\left\{-\int_{S_B} \bar{\iota}\omega e^{\bar{\iota}\omega t}\rho(\psi_0 \frac{\partial\psi_k}{\partial n} - \psi_k \frac{\partial\psi_0}{\partial n})ds\right\} \qquad (2.29)$$

Eq. (2.29) is useful for applying strip theory. However, it cannot be used when the diffraction force is used to obtain the excitation force.

**Restoring loads**

The buoyancy and restoring force from the waterplane and center of buoyancy (CoB) constitute the hydrostatic load. The buoyancy force is equal to the weight of the fluid displaced by the structure and is given as $\rho g \nabla$. The change in waterplane area and the CoB affect the hydrostatic force and moments and it is represented by restoring matrix. The non-zero hydrostatic and inertial restoring coefficient is given in Eq. (2.30) to Eq. (2.34).

$$C_{33,H\&I} = \rho g A_0 \qquad (2.30)$$

$$C_{44,H\&I} = \rho g \int\int_{A_0} y^2 dA + \rho g V_0 z_{CoB} \qquad (2.31)$$

$$C_{55,H\&I} = \rho g \int\int_{A_0} x^2 dA + \rho g V_0 z_{CoB} \qquad (2.32)$$

$$C_{53,H\&I} = -\rho g \int\int_{A_0} x dA \qquad (2.33)$$

$$C_{35,H\&I} = -\rho g \int\int_{A_0} x dA \qquad (2.34)$$

**Morison's equation**

For slender structures, Morison's equation is usually applied instead of the potential flow theory. Morison's equation is valid as long as the diameter-to-wave length ratio is small ($D < \lambda/5$) (Faltinsen, 1993). Eq. (2.35) provides the transverse force per length ($f$) on a cylindrical section.

$$f = \rho\pi\frac{D^2}{4}\dot{u} + \rho C_a\pi\frac{D^2}{4}(\dot{u} - \dot{v}) + \frac{1}{2}\rho C_D D(u - v)|u - v| \qquad (2.35)$$

Where $u, v$ are the transverse wave particle velocity and the local transverse body velocity, respectively, $C_D$ is the drag coefficient and $C_a$ is the added mass coefficient. The first component in Eq. (2.35) corresponds to the FK force, while the second component accounts for the added mass effects. The last component, on the other hand, accounts for the viscous drag

38

forces. Based on linear wave theory's deep water limit, the water particle acceleration at a specific position $(x, y, z)$ where $z$ axis is directed vertically upward, is determined using Eq.(2.36).

$$\dot{u} = \omega^2 \zeta e^{kz} \cos(\omega t - kx) \tag{2.36}$$

If the local transverse body acceleration $\dot{v}$ is neglected, then the transfer function ($H_{Mor}$) of the FK and added mass forces applied on a length element $dl$ positioned at the center relative to the axis can be obtained using Eq.(2.37).

$$H_{Mor} = \frac{f}{\zeta} \approx \rho V (1 + C_a) \omega^2 e^{\left(\frac{\omega^2 z}{g}\right)} \tag{2.37}$$

In time-domain dynamic analysis, it is usual to utilize a combination of Morison's equation and potential flow theory. For slender elements, a full Morison's equation is needed, while the potential flow solution is applied mostly to larger volume bodies. Large-volume bodies can also be subjected to viscous damping based on Morison's equation with appropriate coefficients.

# Chapter 3- Design Methodology

The design methodology/plan for this project is illustrated in Figure 3.1. Each of the blocks in the figure represents a chapter or a sub-chapter in this thesis. The first stage of this project presents a description of the selected wind turbine. Based on that, the maximum expected load acting on the supporting platform can be roughly assumed. The next stage includes proposing a new preliminary design based on a comparison between three different configurations. The configurations are realistic and inspired by similar and already-existing frame structures like the ones used in lifting cranes. Hydrodynamic properties are obtained in the $3^{rd}$ stage. Subsequentially, a fully coupled analysis is carried out to obtain the actual loads acting on the floater. Last, a local analysis is performed to check that the ultimate limit state is not breached for both glulam beams and steel plates. Optimization and testing are not covered within the scope of this thesis but are encouraged to be performed.
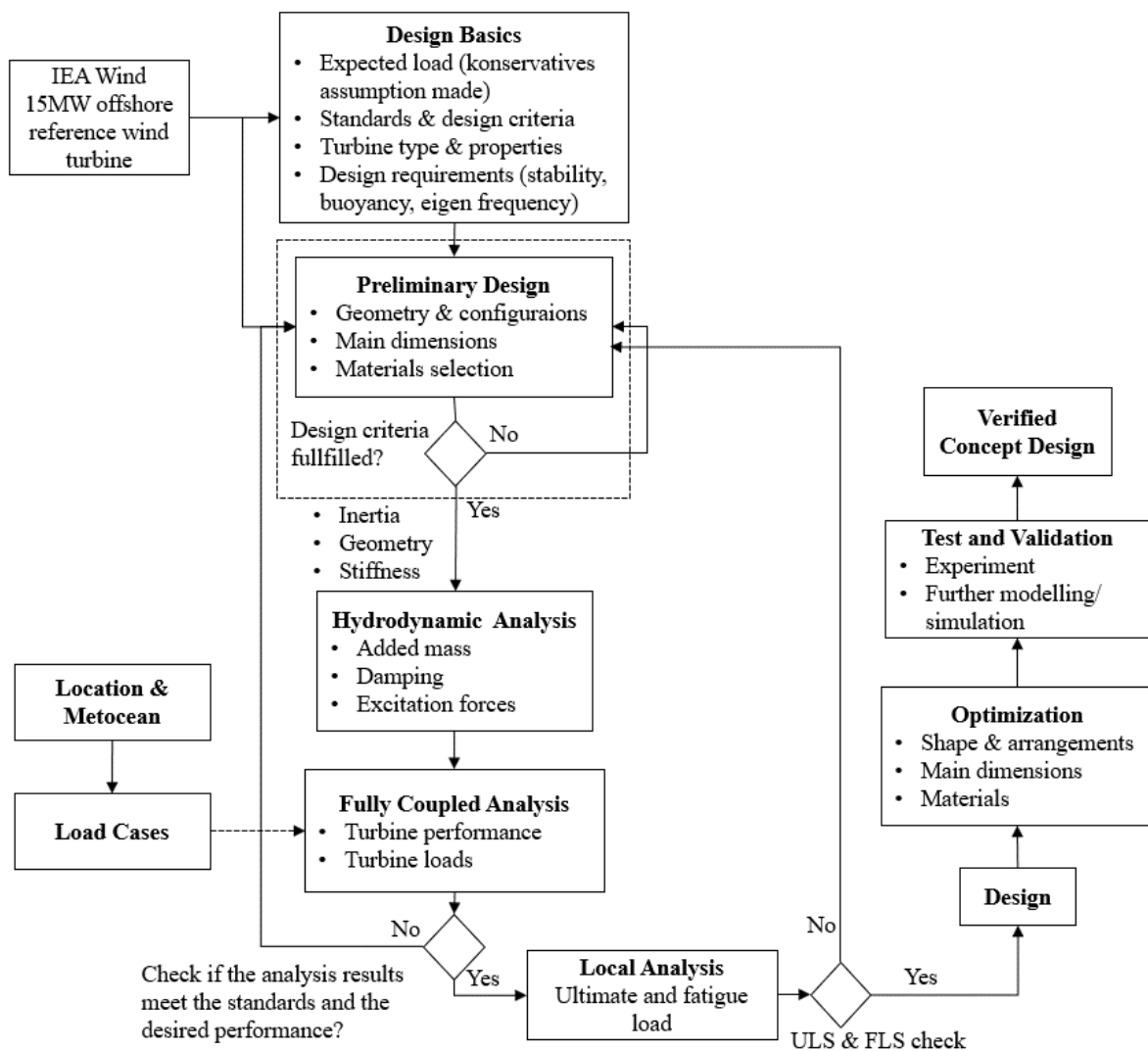


Figure 3.1: Design methodology

## 3.1 System Description

### 3.1.1 The selection of the IEA Wind 15-MW FWT

Due to its publicly available design, the IEA Wind 15-Megawatt offshore reference wind turbine that was developed by International Energy Agency (Gaertner et al., 2020) is chosen as a baseline for the design methodology in this work.

Reference wind turbines in general can be traced back to the early 2000s when the National Renewable Energy Laboratory (NREL) established the Wind Partnership for Advanced Component Technology (WindPACT) turbine series. This series comprised turbines with power ratings of 0.75 MW, 1.5 MW, and 3 MW. These turbines were only available for use within national laboratories in the US with the intention to advance wind turbine technology and enhance turbine performance and reliability (Bywaters et al., 2004). The NREL 5-MW turbine was the first reference turbine accessible to the international community and is still utilized by numerous researchers till today's date (Jonkman et al., 2009). Subsequently, the Technical University of Denmark (DTU) introduced a 10 MW offshore wind turbine (Bak et al., 2013). These two turbines have been complemented by additional turbines, including the 8-MW turbine in the European Union FP7 project LEANWIND (Desmond et al., 2016) and the Sandia National Laboratories' studies of 100-meter blades (Griffith & Ashwill, 2011).

The IEA Wind Task 37 recently issued upgraded 3.35-MW land-based and 10-MW offshore reference turbines (Bortolotti et al., 2019). These designs have been introduced fast after one another as the industry has significantly raised the power rating and size of its products.

To be applicable today and in the future, new reference wind turbines must outperform the present generation of industrial wind turbines, but not so far that aggressive technological advancements are necessary. The existing set of reference wind turbine designs is insufficient to fulfill the demands of the research community and industry to improve the floating foundation design, blade scaling, wind farm control, and logistic studies, to name a few. This necessitated the need for a reference wind turbine that is over 10 MW but less than 20MW, and which served as the driving force behind the development of the IEA-15-240-RWT.

The IEA-15-240-RWT is a class IB direct-drive turbine with a 240 m rotor diameter and a 150 m hub height. The design is the result of a collaboration between NREL, which is funded by the US Department of Energy, and DTU, which is funded by the European Union's H2020 program, as part of the second work package of IEA Wind Task 37 on Wind Energy Systems

Engineering: Integrated RD&D. The IEA-15-240-RWT consists of a floating-specific tower, a chain catenary mooring system, modified floating controller tunning and the UMaine VolturnUS-S floating semisubmersible platform (Allen et al., 2020) developed by the university of Maine in collaboration with the U.S. Department of Energy (Viselli et al., 2014; Viselli et al., 2015; Viselli et al., 2016). The overall key design parameters for the IEA Wind 15-MW-240-RWT are listed in Table 3.1.

Table 3.1: General parameters of IEA Wind 15-MW RWT (Allen et al., 2020; Gaertner et al., 2020)

| Parameter | Value | Units |
|---|---|---|
| Power rating | 15 | MW |
| Rotor orientation, configuration | Upwind, 3 blades | - |
| Control | Variable speed, collective pitch | - |
| Drivetrain | Low-speed, direct drive | |
| Cut-in, rated, cut-out wind speed | 3, 10.59, 25 | m/s |
| Rotor, hub diameter | 240, 7.94 | m |
| Hub height | 150 | m |
| Hub overhang | 11.35 | m |
| Design tip-speed ratio | 9 | - |
| Minimum rotor speed | 5 | rpm |
| Maximum rotor speed | 7.56 | rpm |
| Maximum tip speed | 95 | m/s |
| Platform type | semisubmersible | |
| Freeboard | 15 | m |
| Draft | 20 | m |
| Water depth | 200 | m |
| Mooring system | Three-line chain catenary | |
| Total system mass | 20,093 | t |
| Platform mass | 17,839 | t |
| Rotor nacelle assembly mass | 991 | t |
| Tower mass | 1,263 | t |
| Tower base diameter | 10 | m |

## 3.1.2 Definition of the UMaine VolturnUS-S reference platform

The UMaine VolturnUS-S system, as it is shown in Figure 3.2, is a steel semisubmersible platform that consists of 3 buoyant columns spread radially around a fourth central column that passes through the tower's vertical axis. General properties regarding the UMaine VolturnUS-S reference platform are listed in Table 2, while the main dimensions are illustrated in Figure 1. The UMaine platform will serve as a starting point to establish the new hybrid design.
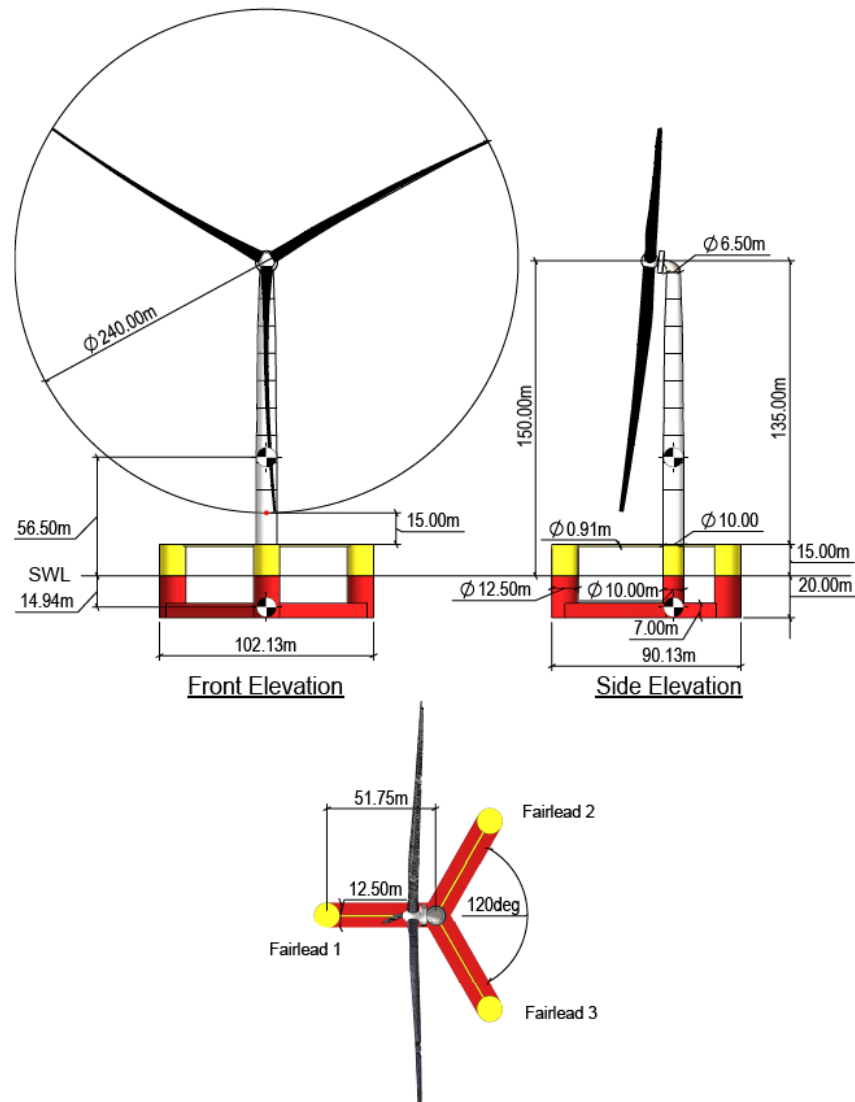
Figure 3.2: General arrangement. Figure courtesy of the University of Maine (Allen et al., 2020)

Table 3.2: Semisubmersible Platform Properties (Allen et al., 2020)

| Parameter | Value | Units |
|---|---|---|
| Hull displacement | 20,206 | $m^3$ |
| Hull steel mass | 3,914 | t |
| Tower interface mass | 100 | t |
| Ballast mass (fixed/fluid) | 2,540/11,300 | t |
| Vertical center of gravity from SWL | -14.94 | m |
| Vertical center of buoyancy from SWL | -13.63 | m |
| Roll inertia about the center of gravity | 1.251E+10 | Kg. $m^2$ |
| Pitch inertia about the center of gravity | 1.251E+10 | Kg. $m^2$ |
| Yaw inertia about the center of gravity | 2.367E+10 | Kg. $m^2$ |

### 3.1.3 Mooring System Properties

The mooring system is made up of three chain catenary lines, each of which is 850 meters long. At a depth of 14 meters below the SWL, each of these lines is connected to the fairlead of one of the platform's three outer columns. The lines are spaced radially to anchors which are evenly spaced at 120 degrees in the surge-sway plane at a depth of 200 meters and at a distance of 837.60 meters from the tower's centerline. For all lines, a studless R3 chain with a nominal diameter of 185 (mm) is used. The mooring line added mass and drag coefficients are determined based on DN VGL-RP-C205 (Det Norske Veritas (DNV), 2010b) and DNV GL-OS-301 (Det Norske Veritas (DNV), 2018). Table 3.3 provide all the details of the mooring system's properties and configuration needed for this thesis (Allen et al., 2020).

Table 3.3: Mooring system's properties (Allen et al., 2020)

| Parameter | Value | Units |
|---|---|---|
| System type & number of lines | Chain Catenary & 3 Lines | - |
| Line type | Studless R3 Chain | - |
| Line breaking strength | 22.286 | kN |
| Fairlead depth | 14 | m |
| Dry line linear density | 685 | kg/m |
| Extensional stiffness | 3270 | MN |
| Line unstretched length | 850 | m |
| Fairlead pretension | 2,437 | kN |
| Fairlead angle from SWL | 56.4 | deg |

### 3.2 Design Basics

### 3.2.1 Standard & regulations

Due to the limited development of floating offshore wind power, there is a scarcity of regulations and instructions that specify the construction requirements of these structures. Furthermore, and to today date, standards that define the requirements for using glulam in the construction of offshore platforms do not exist. Therefore, the design criteria for this work are based on combining glulam standards on one hand with the main design standards for both floating and general (bottom fixed) wind turbines on the other. Table 3.4 show the main design standards used in this work.

Table 3.4: The main standards followed in the project

| Standard | Number | Usage |
|---|---|---|
| Design of floating wind turbine structures | DNV-OS-J103 | Requirements for column-stabilized structures and load factors for the ULS case |
| Wind energy generation systems -Part 1: Design requirements (IEC-61400-1, 2005) | IEC 61400-1 | Design load cases (DLC) |
| Design of offshore steel structures, general (LRFD method) (Det Norske Veritas (DNV), 2011) | DNV-OS- C101 | Guidelines and requirements for the design of offshore steel structures |
| Buckling strength of plated structures (Det Norske Veritas (DNV), 2010a) | DNV-RP-C201 | Guidelines for buckling and ultimate strength assessment of plated structures. |
| Glued laminated timber and glued solid timber Requirements (European Committee for Standardization CEN, 2013) | NS-EN 14080:2013+NA:2016 | Characteristic strength and stiffness properties |
| Eurocode 5: Design of timber structures - Part 1-1: General (European Committee for Standardization CEN, 2006) | EN 1995-1-1:2004+A1 | Guidelines and requirements for the design of timber structures |

## 3.2.2 Key design parameter

Designing a semisubmersible platform's pontoon is a very complex process that involves various technical considerations, and it is essential to adhere to a multitude of both international and Norwegian standards and regulations to ensure the safety and reliability of the entire structure. The initial step is to identify the crucial requirements and key parameters that carry the most weight in the design process. This includes:

## Stability

The stability of a structure is important to maintain its upright position, also referred to as stable equilibrium. The structure must be able to withstand disturbances such as forces and moments caused by excitation and return to equilibrium once the excitation has ceased. DNV-OS-J103 (Det Norske Veritas DNV-GL, 2013) is the design standard that outlines the stability requirements for floating offshore wind turbines. According to this standard, the floating structure must maintain the wind turbine's stability at the wind speed that produces the largest rotor thrust. Additionally, it should sustain stability during severe storm conditions, including rotor standstill, and have sufficient stability for temporary phases such as assembly and tow-out to the site. The power generated by the wind turbine is related to the angle between the wind inflow and the rotor plane. A change in this angle, caused by pitch rotation, reduces the turbine's power production by approximately the cosine of the pitch angle. Therefore, the restoring stiffness of the structure around the y-axis should be as large as possible to reduce rotation around this axis.

## Eigen frequency

The eigenfrequency, also referred to as natural frequency is an important design parameter that defines how the dynamic response of the platform due to external loads (waves, wind, current, etc.) will be. To prevent resonance and large responses, the natural period must fall outside of the wave spectrum, which is recommended to be between 5 and 25 seconds for floating wind turbines, according to section 2.1.3 in the DNV-OS-J103 standard (Det Norske Veritas DNV-GL, 2013). It is also important to ensure that there is a clear difference between the periods of heave and pitch to prevent coupled vibration.

## Assembly procedure

The assembly procedure is an important aspect to consider in the design of a pontoon. The assembly procedure involves the sequence of steps and methods used to construct the pontoon, and it can affect the final quality, safety, and performance of the entire wind turbine. During the assembly process, various components of the pontoon are assembled (welded or fastened) to form a cohesive structure. The assembly procedure should be designed to ensure proper fit and alignment of the components and to minimize the potential for defects or errors in the welding or fastening process. The assembly procedure also impacts the cost and schedule of the project. An efficient and well-planned assembly procedure can help to reduce the overall cost and construction time of the pontoon.

**<u>Dimensions and geometry</u>**

The dimensions and geometry of the substructure are essential to ensure a safe and effective performance of the entire wind turbine. The dimensions and geometry of the pontoon and its supporting structure determine their strength, stiffness, and buckling capacity, which are vital in carrying the weight of wind turbines and resisting environmental loads such as wind and waves. In addition to that, larger dimensions or more complex geometries require more material, which in turn will have a significant impact on the cost, dynamic performance, and environment.

**<u>Mass</u>**

The structural mass of the platform is an important design parameter due to many reasons. Firstly, the structural mass of the platform can affect its function, dynamic performance, and integrity. Secondly, the structural mass is a major cost driver since it determines the actual material cost, the manufacturing time, and the lifting and transportation expenses. Finally, reducing the structural mass can have many positive environmental impacts, as it decreases the magnitude of the resources needed for production, transportation, and lifting operations, as well as the total carbon footprint. Therefore, when proposing a new platform design, it is important to optimize the mass to achieve the desired dynamic performance, cost-effectiveness, and environmental impact.

**<u>Cost</u>**

The competitiveness of floating offshore wind as an energy solution is determined by its cost per produced energy unit compared to other energy sources, particularly non-renewable sources. To be competitive, the cost must be low, and the energy output must be large.

To analyze the cost of wind turbines, three important terms are used: Capital Expenditure (CAPEX), Operational Expenditure (OPEX), and Levelized Cost of Energy (LCOE). CAPEX refers to the investment cost of physical components such as the turbine, installation, anchors, moorings, platform, and decommissioning, which will be used for more than a year. OPEX refers to the costs of running the operations, which for offshore wind turbines include maintenance and operation of the structure. LCOE is the average cost of producing one unit of energy for a wind turbine, typically measured in kWh, and includes both CAPEX and OPEX over its lifetime The calculation of LCOE can be done using Eq. (3.1):

$$LCOE = \frac{\text{Total lifetime cost}}{\text{Total lifetime output}} \qquad (3.1)$$

## 3.2.3 Expected load

To propose a new design, the initial step involves examining the various loads that affect the floater. As illustrated in Figure 2.13, FWTs are exposed to a wide range of environmental loads that have been covered in Chapter 2. However, to simplify the complexity of the design process and make it more manageable, certain assumptions and simplifications were made, see Figure 4.4:

- Aerodynamic loads:
  - The steady aerodynamic load generated by the mean wind speed is the most dominant, and the thrust force at rated wind velocity will cause a bending moment acting on all 3 pontoons.
  - Periodic aerodynamic loads such as wind shear, rotor rotation, and tower shadow are negligible.
  - Random aerodynamic loads induced by gusts, turbulence, and dynamic effects are negligible.
- Hydrostatic pressure effects are considered at draft=20 m.
- Hydrodynamic loads are negligible (only for the preliminary stage of the design)

In addition, it is assumed that the columns of the floater are rigid bodies and the focus will be merely on the pontoons.

It is worth noting that these assumptions are made solely for the sake of simplicity to establish an initial design and may result in over- or under-conservative results.

## 3.3 Design Criteria in Ultimate Limit Design

## 3.3.1 Ultimate limit state check for timber design (Partial Factor Method):

According to EN 1995-1-1 (European Committee for Standardization CEN, 2006), the design value $X_d$ of a strength property shall be calculated based on the Partial Factor Method (PFM) as the following:

$$X_d = k_{mod} \frac{X_k}{\gamma_m} \tag{3.2}$$

Where $X_k$ is the characteristic value of a strength property, $\gamma_m$ is the partial factor for a material property and resistance and is recommended to be 1.25 for glulam, and $k_{mod}$ is a modification factor considering the effect of the duration of load and the moisture content. The value of $k_{mod}$ for glulam can be found in EN 1995-1-1 standard. The wind load is recommended to be chosen as a short-term load according to the same standard. The service class can be chosen as 3 since the operating environment of FWT is characterized by climate conditions leading to higher moisture content than other classes. Based on that, $k_{mod}$ can be taken as 0.7, see Table 3.5 (European Committee for Standardization CEN, 2006).

Table 3.5: Values of $k_{mod}$ according to load-duration class (European Committee for Standardization CEN, 2006)

| Material | Service Class | Permanent action | Long term action | Medium-term action | Short term action | Instantaneous action |
|----------|---------------|------------------|------------------|--------------------|-------------------|----------------------|
|          | 1             | 0.6              | 0.7              | 0.8                | 0.9               | 1.1                  |
| glulam   | 2             | 0.6              | 0.7              | 0.8                | 0.9               | 1.1                  |
|          | 3             | 0.5              | 0.55             | 0.65               | 0.7               | 0.9                  |

Based on that,

$$X_d = 0.7 \frac{X_k}{1.25} = 0.56\, X_k \tag{3.3}$$

## Combined bending and axial tension check

To ensure that glulam beams are strong enough for this case, the following expressions shall be satisfied:

**Criteria 1**
$$\frac{\sigma_{t,0,d}}{f_{t,0,d}} + \frac{\sigma_{m,y,d}}{f_{m,y,d}} + k_m \cdot \frac{\sigma_{m,z,d}}{f_{m,z,d}} \leq 1 \tag{3.4}$$

**Criteria 2**
$$\frac{\sigma_{t,0,d}}{f_{t,0,d}} + k_m \cdot \frac{\sigma_{m,y,d}}{f_{m,y,d}} + \frac{\sigma_{m,z,d}}{f_{m,z,d}} \leq 1 \tag{3.5}$$

Where $\sigma_{t,0,d}$ is the design tensile stress along the grain, $f_{t,0,d}$ is the design tensile strength along the grain. $\sigma_{m,y,d}$ and $\sigma_{m,z,d}$ are the design bending stresses about the principal axes, $f_{m,y,d}$, $f_{m,z,d}$ are the corresponding design bending strengths. The factor $k_m$ makes allowance for the re-distribution of stresses and the effect of inhomogeneities of the material in a cross-section. For glulam with a rectangular section $k_m = 0.7$.

## Combined bending and axial compression check

To ensure that glulam beams are strong enough for this case, the following expressions shall be satisfied:

**Criteria 3**
$$\left(\frac{\sigma_{c,0,d}}{f_{c,0,d}}\right)^2 + \frac{\sigma_{m,y,d}}{f_{m,y,d}} + k_m \cdot \frac{\sigma_{m,z,d}}{f_{m,z,d}} \leq 1 \tag{3.6}$$

**Criteria 4**
$$\left(\frac{\sigma_{c,0,d}}{f_{c,0,d}}\right)^2 + k_m \cdot \frac{\sigma_{m,y,d}}{f_{m,y,d}} + \frac{\sigma_{m,z,d}}{f_{m,z,d}} \leq 1 \tag{3.7}$$

Where $\sigma_{c,0,d}$ is the design compressive stress along the grain, $f_{c,0,d}$ is the design's compressive strength along the grain. The value of $k_m = 0.7$ applies.

## Beam stability due to combined bending and compression check

In the case where a combination of moment $M_y$ about the strong axis y and compressive force $N_c$ exists, lateral torsional stability must be verified using the following expression:

**Criteria 5**
$$\left(\frac{\sigma_{m,d}}{k_{crit} \cdot f_{m,d}}\right)^2 + \frac{\sigma_{c,0,d}}{k_{c,z} \cdot f_{c,0,d}} \leq 1 \tag{3.8}$$

Where $\sigma_{m,d}$ is the design bending stress, $\sigma_{c,0,d}$ is the design compressive stress parallel to the grain, $f_{c,0,d}$ is the design compressive strength parallel to the grain. $k_{crit}$ is a factor that takes

into account the reduced bending strength due to lateral buckling and can be determined from Eq. (3.9).

$$k_{crit} = \begin{cases} 1 & For \ \lambda_{rel,m} \leq 0.75 \\ 1.56 - 0.75\lambda_{rel,m} & For \ 0.75 \leq \lambda_{rel,m} \leq 1.4 \\ \dfrac{1}{\lambda_{rel,m}{}^2} & For \ 1.4 \leq \lambda_{rel,m} \end{cases} \quad (3.9)$$

Where $\lambda_{rel,m}$ is the relative slenderness for bending and should be taken as:

$$\lambda_{rel,m} = \sqrt{\frac{f_{m,k}}{\sigma_{m,crit}}} \quad (3.10)$$

Where $\sigma_{m,crit}$ is the critical bending stress calculated according to the classical theory of stability:

$$\sigma_{m,crit} = \frac{0.78b^2}{h\ell_{ef}}E_{0,05} \quad (3.11)$$

Where $b, and \ h$ are the beam width and depth, respectively, $\ell_{ef}$ is the effective length and can be taken from EN 1995-1-1 standard based on the beam type and loading type, $E_{0,05}$ is the fifth percentile value of the modulus of elasticity parallel to the grain. $k_{c,z}$ is an instability factor given by Eq. (3.12):

$$k_{c,z} = \frac{1}{k_z + \sqrt{k_z{}^2 - \lambda_{rel,z}{}^2}} \quad (3.12)$$

$$k_z = 0.5\big(1 + \beta_c\big(\lambda_{rel,z} - 0.3\big) + \lambda_{rel,z}{}^2\big) \quad (3.13)$$

Where $\beta_c = 0.1$ is taken for glulam. $\lambda_{rel,z}$ is calculated using Eq. (3.14).

$$\lambda_{rel,z} = \frac{\lambda_z}{\pi}\sqrt{\frac{f_{c,0,k}}{E_{0,05}}} \quad (3.14)$$

Where $\lambda_z, \lambda_{rel,z}$ are the slenderness ratio and the relative slenderness ratio corresponding to bending about the z-axis, respectively. $\lambda_z$ can be calculated from Eq. (3.15).

$$\lambda_z = \frac{\ell_{ef}}{R} \tag{3.15}$$

Where $R$ is the radius of gyration.

## 3.3.2 Ultimate limit check for steel design (Load and resistance factor design LRFD) :

According to DNV-OS- C101 (Det Norske Veritas (DNV), 2011), a structural element is considered safe if Eq. (3.16) is satisfied:

$$S_d \leq R_d \tag{3.16}$$

Where $S_d$ is the design load effect and $R_d$ is the design resistance. The design load effect represents the worst-case combined effect and is usually determined using Eq. (3.17).

$$S_d = q(X_{d1}, X_{d2} \dots . X_{dn}) \tag{3.17}$$

Where $q$ is the load effect function and $X_d$ is the design load which can be obtained from Eq. (3.18)

$$X_d = \gamma_f X_k \tag{3.18}$$

Where $X_k$ is characteristic load, and $\gamma_f$ is the load factor that accounts for any potential negative deviations in the loads from their characteristic values, the lower probability of the multiple loads acting at their characteristic values at the same time, and the uncertainties in the methods and analysis employed to calculate load effects.

In case the load and load effect are linearly related then $S_d$ can be written as the summation of characteristic load effects multiplied by their corresponding load factor as seen in Eq (3.19).

$$S_d = \sum_{i=1}^{n} (\gamma_{f,i} . S_{k,i}) \tag{3.19}$$

$R_d$ can be calculated as in Eq. (3.20) using the characteristic strength $R_k$ and the material factor $\gamma_m$ that accounts for any potential negative deviations in the strength of materials from their characteristic values, as well as the possibility that the overall strength of the structure may be less than the characteristic values obtained by testing individual samples of the material.

$$R_d = \frac{R_k}{\gamma_m} \tag{3.20}$$

$\gamma_m = 1.15$ is taken for plated structure.

According to DNV-OS-C101, the structural capacity of steel shall be checked for all the structural components for excessive yielding and excessive buckling.

## **Plate yielding check**

DNV-OS- C101 standard states that von Mises equivalent design stress and each of the individual design stress components for plated structures shall not exceed the design resistance, see Eq. (3.21).

$$\sigma_{j,d} = \sqrt{\sigma_{x,d}{}^2 + \sigma_{y,d}{}^2 - \sigma_{x,d}.\sigma_{y,d} + 3\tau_d{}^2} \tag{3.21}$$

$\sigma_{x,d}, \sigma_{y,d}$ are the design stresses in $x, y$ direction, respectively, $\tau_d$ is the design shear stress in the x-y plane. Eq. (3.21) can be written as:

**Criteria 6** $\qquad\qquad \gamma_m \dfrac{\sigma_{j,d}}{R_k} \leq 1 \tag{3.22}$

## **Plate buckling check**

The buckling resistance for unstiffened plates is an important aspect that must be estimated according to Chap. 6 in DNV–RP-C201 standard (Det Norske Veritas (DNV), 2010a), but will not be covered within the scope of this thesis.

# Chapter 4- Preliminary Concept Design

## 4.1. FEA Modelling

## 4.1.1 Analysis models

Initial concept design is the preliminary stage of the design process where ideas are generated and explored to create a basic outline of the design. It helps to establish the direction of the project and provides a starting point for further development or refinements. In this step, three different hybrid-substructure configurations are created and compared using Ansys Workbench 2020 R1. Each of these configurations has the same external dimensions as the UMaine VolturnUS-S semisubmersible platform, and each consists of steel plates/shells supported by different glulam frame systems that differ in their layout and the number and dimensions of the supporting beams. The thickness of the floater's steel plates is taken as 0.05 m which is reasonable for FWT's semisubmersible platforms with a draft of around 20-25 m (Roach et al., 2023; Zhao et al., 2021). Furthermore, the plate thickness is assumed to be constant in all directions.

The glulam support frames are designed to support the pontoons between the centreline of the central column and the centrelines of the three radial columns only. The columns of the substructure are assumed to be rigid bodies and left without any change from the UMaine VolturnUS-S semisubmersible platform's original design. The three configurations are shown in Figure 4.1 and will be tested for the yielding and buckling criteria mentioned in Chap. 3 to select the best model to proceed with. The layout of the cross sections of the glulam beam is represented in Figure 4.2. For more details about the design and dimensions for each configuration, see Appendix A.

**Configuration (a)**
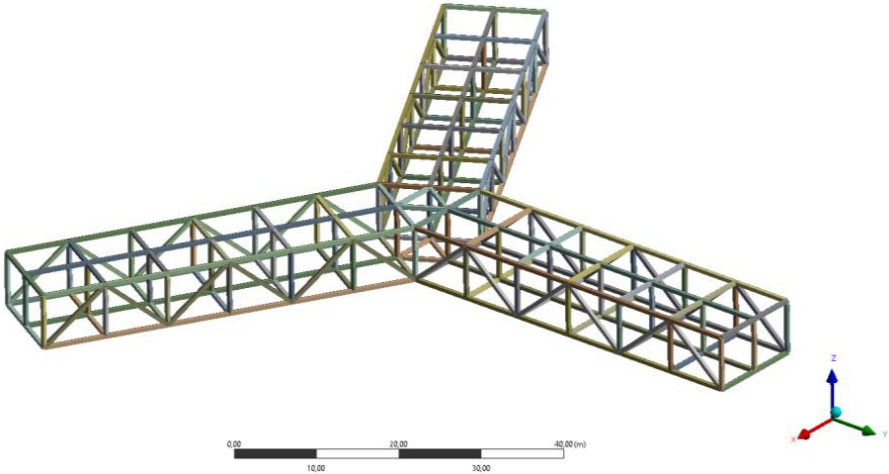


**Configuration (b)**
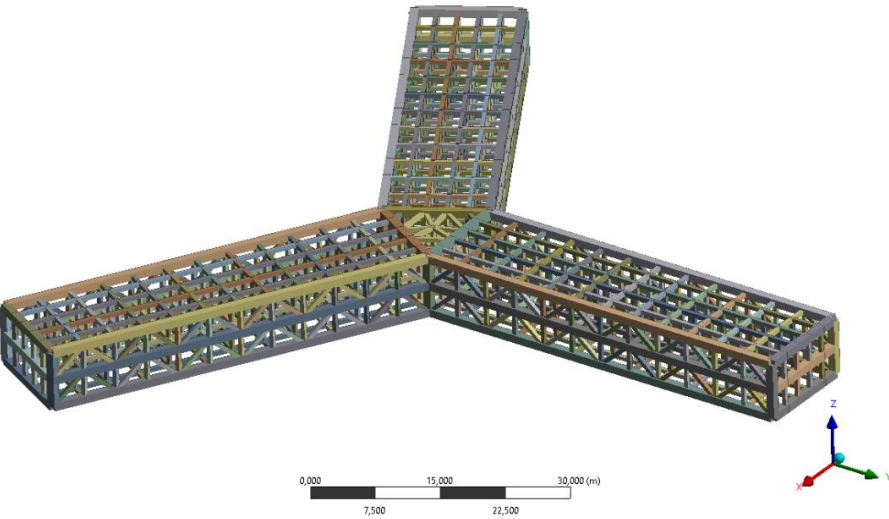


**Configuration (c)**
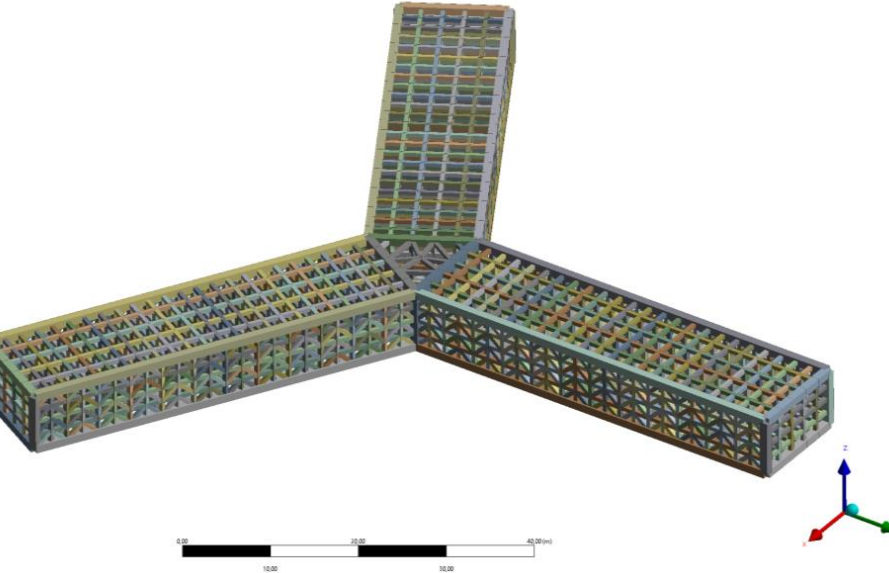


Figure 4.1: Glulam frame systems for the three proposed configurations

0.5 m

0.5 m

1 m

1 m

Cross section (a)                    Cross section (b)
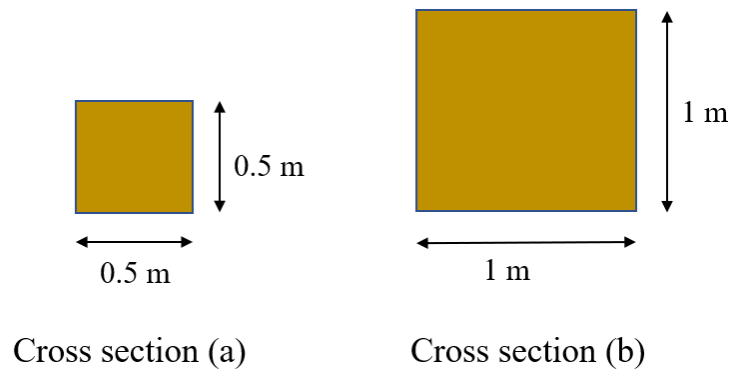
Figure 4.2: Cross sections of the glulam beams

All the timber beams in configuration (a) have the same cross-section (a). On the other hand, configurations (b) and (c) have a combination of both (a) and (b) cross-sections, see Figure 4.1, where all the internal beams have a smaller cross-section (a), and all the main bounding beams are chosen with a greater cross-section (b) since larger combinations of loads are expected to act on these beams.

The 3D model consists of shell and beam elements for all three configurations. All the details regarding loads, boundary conditions, material properties, mesh and mesh convergence studies are provided in the following sections.

### 4.1.2 Loads and boundary conditions

For the preliminary stage of the design, all the analyzed models are studied with the assumption that the floater is fully ballasted at 20 m draft. Each model is subjected to hydrostatic pressure together with the transferred loads generated from the maximum aerodynamic steady load acting on the hub as mentioned in Sect. 3.2.3, see Figure 4.3. To ensure robustness, additional bending moments are applied at the tower base (0,0,15) around x- and z-axes which account for 10% of the maximum aerodynamic bending moment.

Figure 4.4 (left) shows the power and thrust curve for the 15MW FWT which is utilized to extract the maximum expected steady load on the wind turbine. Figure 4.4 (right) shows that one pinned support (constraint) was applied to one of the radial columns to simulate the behaviour of the floater. Furthermore, the evaluation of the design is performed only on the other unconstrained pontoons, while the supported pontoon is excluded during the evaluation process.
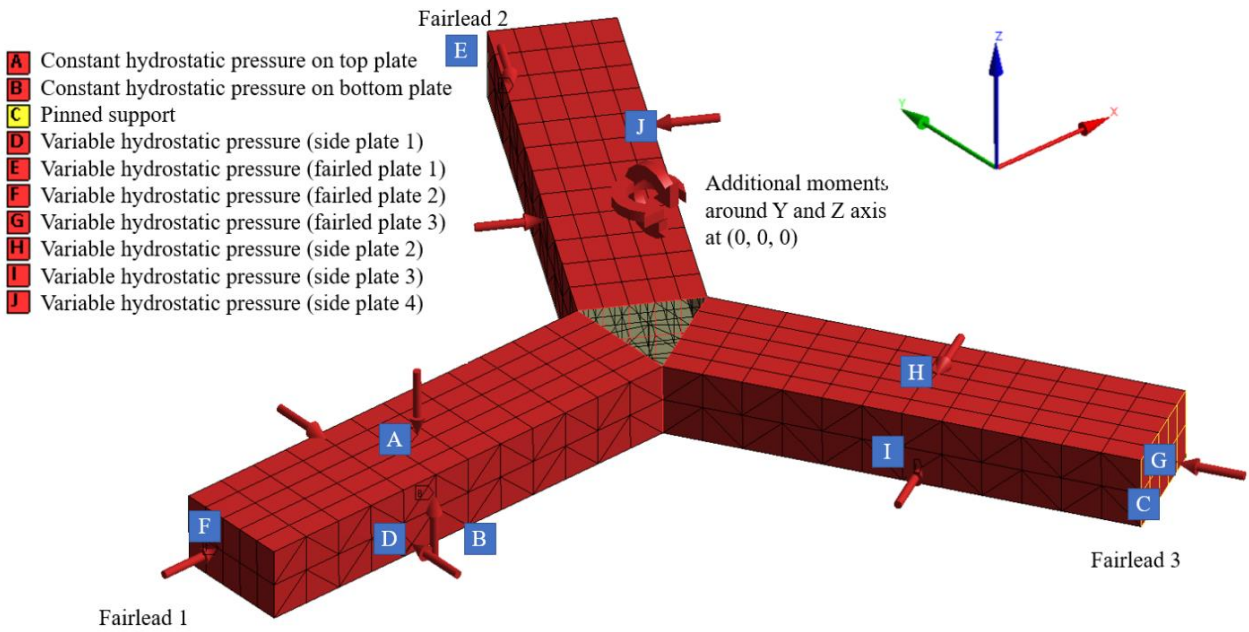
Figure 4.3: The loads and boundary conditions defined for the preliminary hybrid design, configuration (b)  (ANSYS)
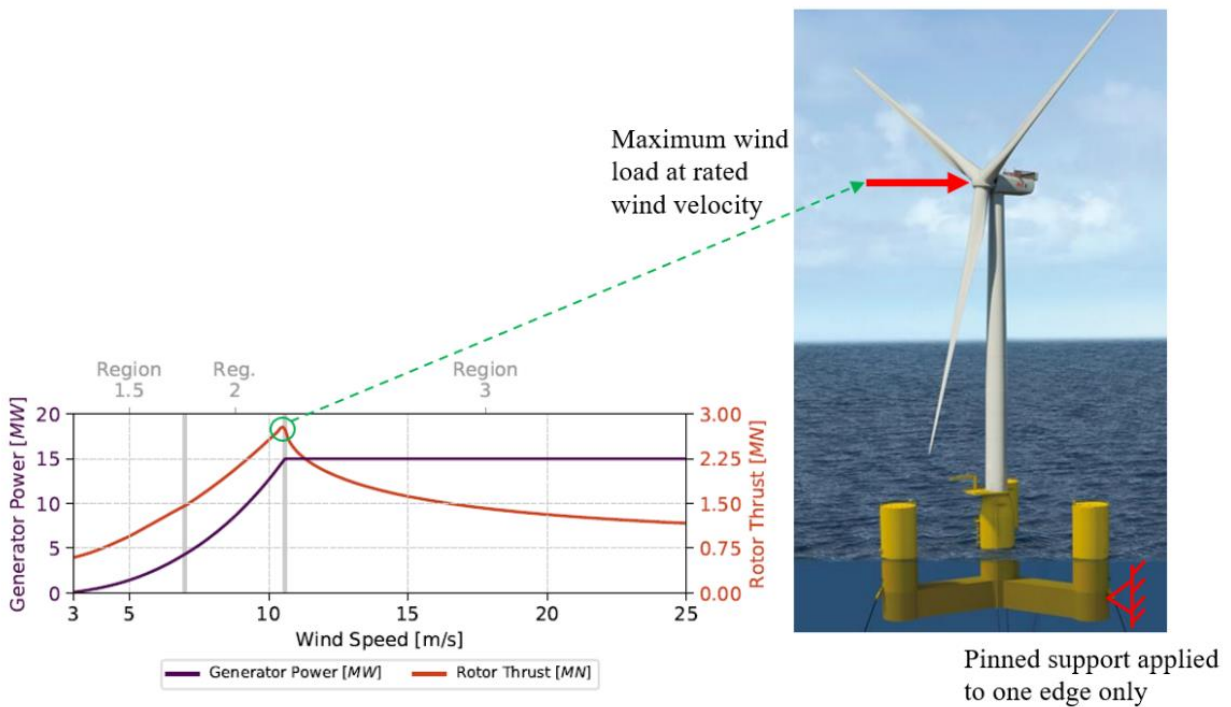


Figure 4.4: Using the 15MW FWT's power and thrust curve to estimate the maximum aerodynamic loading (Gaertner et al., 2020)

To cover the worst-case scenario, it is necessary to study each of the configurations twice (as two cases) since the entire turbine is not symmetric about its y-axis, and different results might yield from changing the location of the pinned support from one column to another. The supported column must be placed in one case on position 1 (where fairlead 1 is located) and in the other case on position 2 or 3 since the turbine is symmetrical about the x-axis, see Figure 2.18. However, to reduce the overall computational time, the pinned support is applied only to position 3 since it is more comprehensive and covers the two remaining pontoons which are non-symmetric.

## 4.1.3 Material properties

To perform the finite element analysis, material properties of isotropic-elastic steel were assigned for the pontoon plates (see Table 4.1).

Table 4.1: Material properties of structural steel assigned to the pontoons' plates

| Property | Value | Unit |
|---|---|---|
| Density | 7850 | kg/m$^3$ |
| Young's Modulus | 2E+11 | Pa |
| Poisson's Ratio | 0.3 | |
| Bulk Modulus | 1.667E+11 | Pa |
| Shear Modulus | 7.692E+11 | Pa |
| Tensile Yield Strength | 2.5E+08 | Pa |
| Compressive Yield Strength | 2.5E+08 | Pa |
| Tensile Ultimate Strength | 4.6E+08 | Pa |
| Compressive Ultimate Strength | 0 | Pa |
| Coefficient of Thermal Expansion | 1.2E-05 | C$^{-1}$ |

Glulam is an anisotropic material. However, it is commonly assumed to be orthotropic in structural design. Figure 4.5 shows the three orthogonal axes L, R, and T (longitudinal, radial, and tangential directions respectively). The properties in R and T directions are identical and refer to the perpendicular to the grain properties, while all the properties in the L direction are different and refer to the parallel to the grain properties (Alvarez & Fernandez, 2016). Therefore, Orthotropic-elastic glulam (strength class Gl30h) with properties as in Table 4.2 was assigned for all the supporting beams.
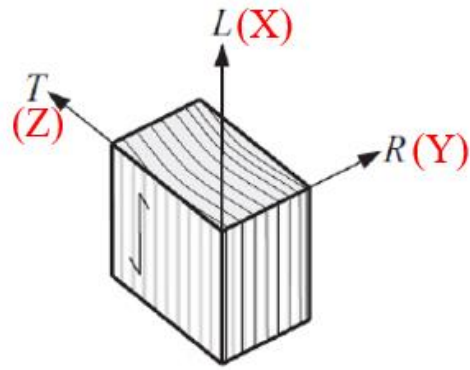
Figure 4.5: Orthogonal (principle) axes for structural glulam design (Alvarez & Fernandez, 2016)

Table 4.2: Material properties of GL30h assigned to pontoon's supporting beams

| Property | Value | Unit |
|---|---|---|
| Density | 480 | kg/m$^3$ |
| Young's Modulus X(L) direction | 1.36E+10 | Pa |
| Young's Modulus Y(R) direction | 3E+08 | Pa |
| Young's Modulus Z(T) direction | 3E+08 | Pa |
| Poisson's Ratio XY | 0.21 | - |
| Poisson's Ratio YZ | 0.21 | - |
| Poisson's Ratio XZ | 0.24 | - |
| Shear Modulus XY | 6.5E+08 | Pa |
| Shear Modulus YZ | 6.5E+08 | Pa |
| Shear Modulus XZ | 6.5E+08 | Pa |
| Tensile Yield Strength | 2.4E+07 | Pa |
| Compressive Yield Strength | 3E+07 | Pa |
| Coefficient of Thermal Expansion X direction | 5E-06 | $C^{-1}$ |
| Coefficient of Thermal Expansion Y direction | 5E-06 | $C^{-1}$ |
| Coefficient of Thermal Expansion Z direction | 5E-06 | $C^{-1}$ |

## 4.1.4 Mesh element types

For the analysis, quadrilateral element types are mainly used since they can capture the geometry behavior accurately and they give a more realistic representation of the deformation. The triangular elements type is avoided because they are relatively stiff and do not accurately

capture the bending moments (Skotny, 2019). All the element types used for analyzing the three configurations are represented in Table 4.3.

Table 4.3: Mesh - Element type details

| Mesh area | Element name IDs | Element shape |
|---|---|---|
| Steel plates | SHELL181 | QUAD4 |
| Glulam beams | BEAM188 | BEAM3 |

## 4.1.5 Mesh convergence studies

Regardless of the element type, size, or order, a mesh convergence study must be performed according to the mesh convergence criteria set by standards. Changing the meshing element size influences the FEA outputs and based on that the mesh must be incrementally refined to the extent where increasing the refining level will have no significant influence on the results obtained. To balance between accuracy and computational time, mesh convergence studies are conducted on all three configurations using five different mesh element sizes. However, only results for configuration (b) are shown since the other two configurations are quite similar. The study begins by evaluating some of the outputs obtained from a very coarse mesh, corresponding to an element size of 0.8 m, and gradually refining it (by re-running with half of the element size) until the results obtained are reasonably stable. Both the maximum von Mises equivalent stress on steel plates and the maximum total bending moment acting on the wooden beams are evaluated against the 5 levels of refinements. The study shows a decrease in the convergence error (relative error) for both cases. At element size 0.1 m (Figure 4.6), the relative error is less than 5% for both outputs and is deemed to be acceptable for the linear analysis case, see Figure 4.7.
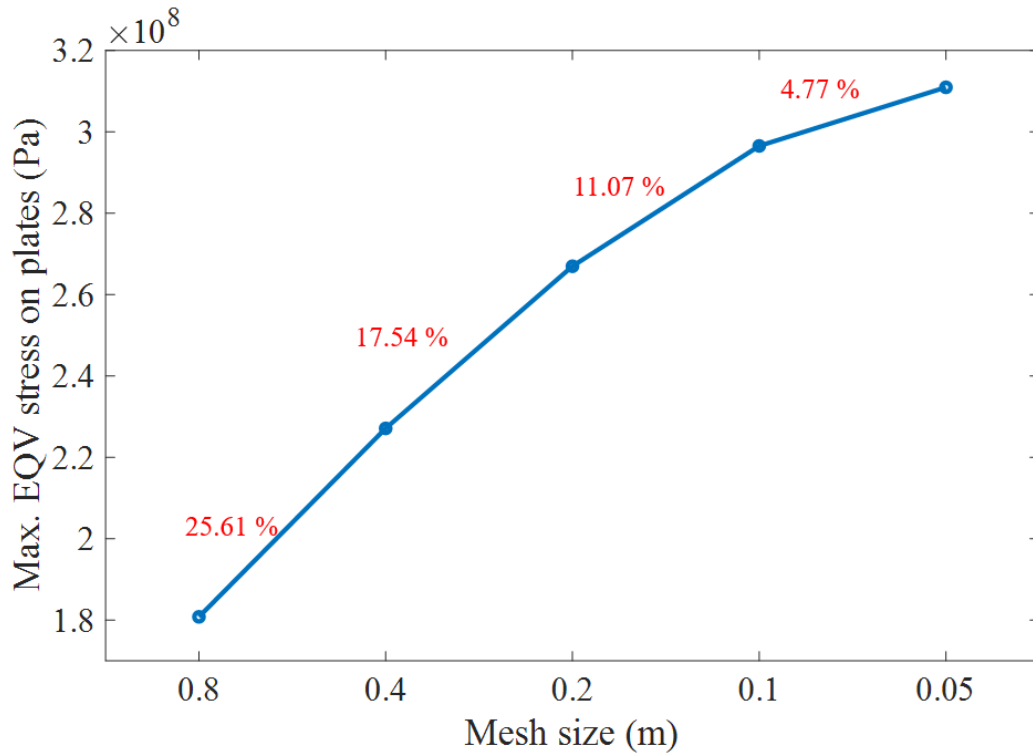
(a)
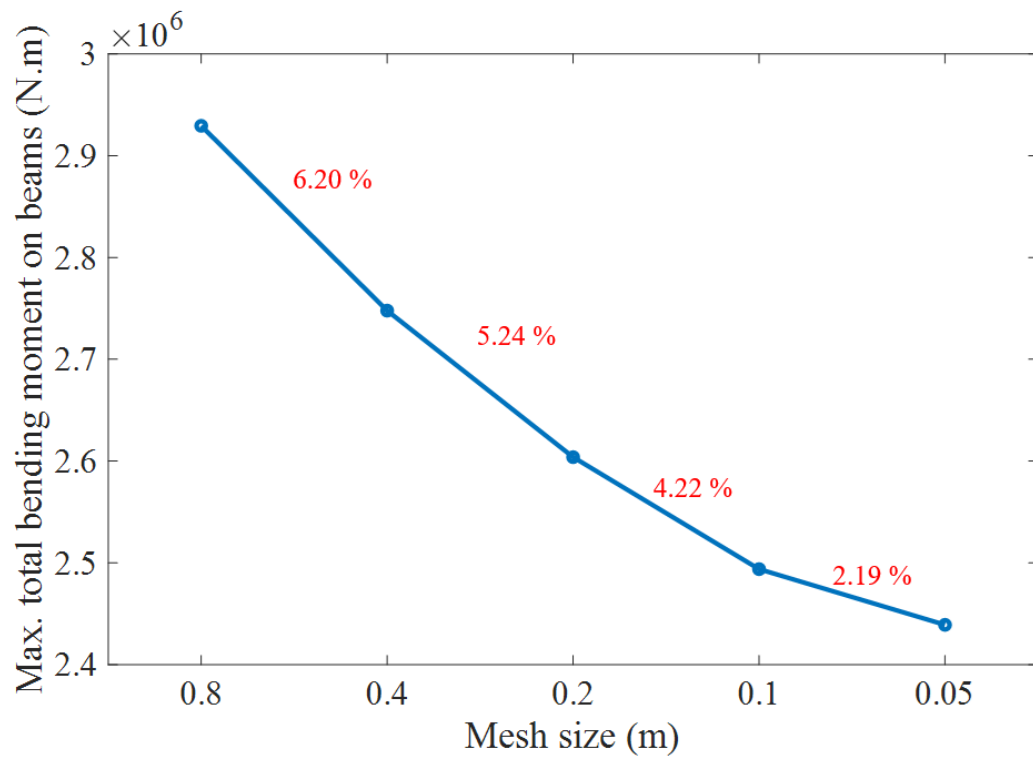


(b)

Figure 4.6: Percentage error based on mesh refinement study for configuration (b) for two outputs; (a) Maximum von Mises equivalent stress on steel plates and (b) Maximum total bending moment acting on glulam beams
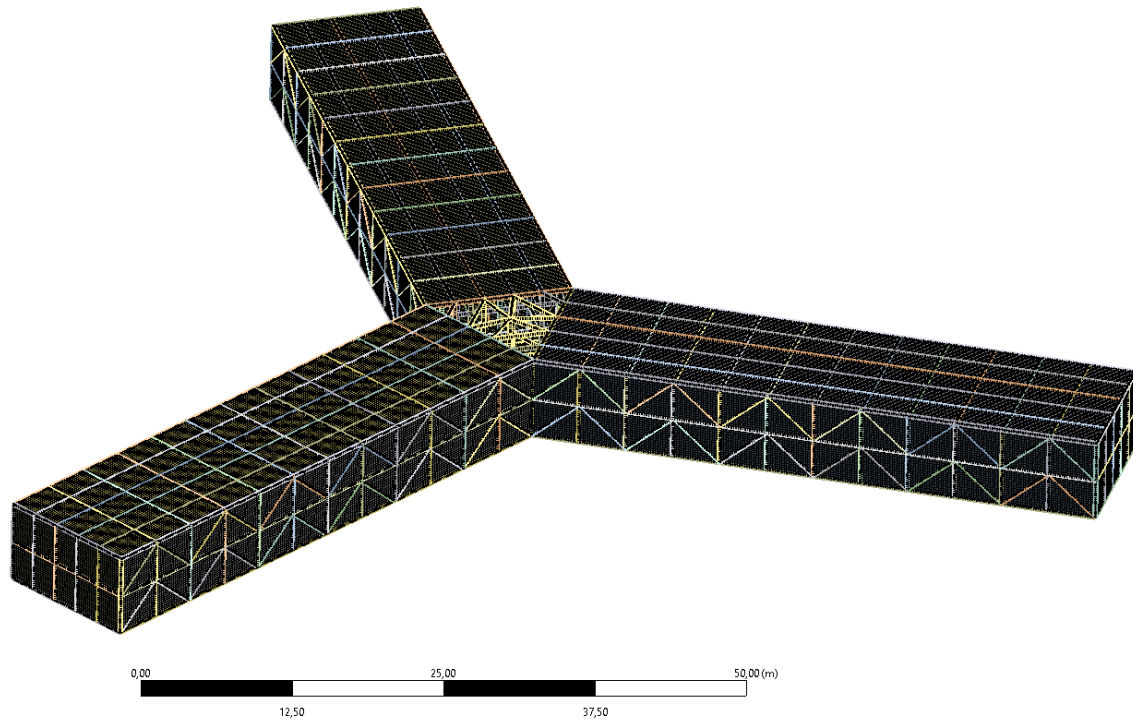
Figure 4.7: ANSYS model showing the visualized mesh details of configuration (b) at 0.05 m element size.

## 4.2 Results and Selection

To have a simpler way to analyze the design, all key stress results were normalized in the same way as in the left side of the 6 design criteria represented in Eq. (3.4), Eq. (3.5), Eq. (3.6), Eq. (3.7), Eq. (3.8) and Eq. (3.22). This normalized version represents the beam's utilization factor (UF) for the corresponding criteria. Figure 4.8 and Figure 4.9 show the utilization factors values obtained for the unsupported pontoons for both 1st and 2nd combined bending and tension criteria for configuration (b). Fairlead 3 is pinned jointed and therefore no utilization factor values are shown for it in the figures. According to these figures, the maximum utilization factor for the beams under combined bending and tension is captured at the bottom of the substructure, and it gradually increases toward the point where all three pontoons intersect. It is important to remember that the negative values signify beams under compression (blue color) which are discarded from consideration for the combined bending and tension case.

The results regarding all utilizations factors (all criteria) for all configurations are provided in Appendix B.
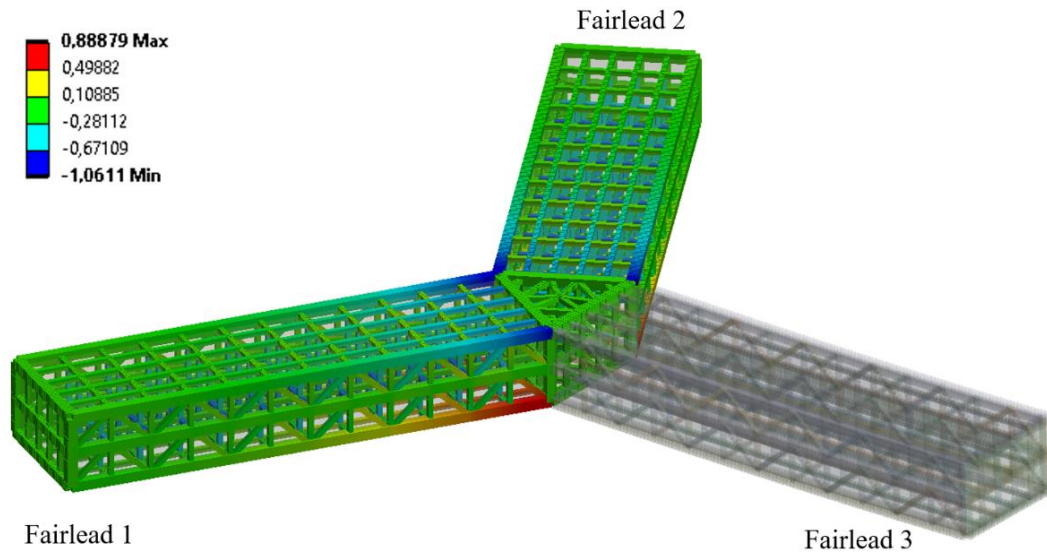
Figure 4.8: Utilization factor corresponding to the 1$^{st}$ combined bending and tension criteria for glulam, configuration (b)
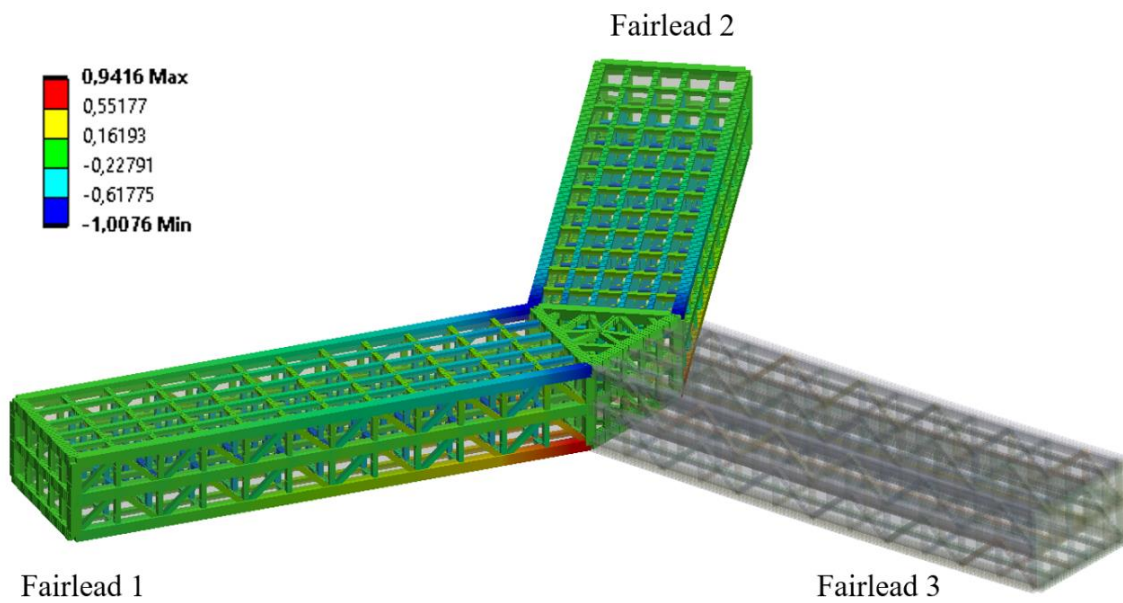


Figure 4.9: Utilization factor corresponding to the 2$^{nd}$ combined bending and tension criteria for glulam, configuration (b)

Table 4.4 presents a comparison of the maximum utilization factor results (corresponding to 6 design criteria) of the three configurations, intending to select the best option to proceed with. Configuration (a) has a maximum utilization factor greater than one for all criteria, which means it cannot be considered further in the design process. Conversely, configurations (b) and (c) show acceptable and similar maximum utilization factors for most of the criteria (conservative

since it is less than 1). However, Configuration (b) has less number of beams (less material), indicating that it is the best option to adopt in the design process.

Table 4.4: Max utilization factor for the three hybrid configurations

| Material | Design criteria | Config. (a) | Config. (b) | Config. (c) |
|---|---|---|---|---|
| Glulam | $UF_{max,\ 1}$ | 1.03 | 0.75 | 0.76 |
| | $UF_{max,\ 2}$ | 1.04 | 0.80 | 0.82 |
| | $UF_{max,\ 3}$ | 5.63 | 0.90 | 0.94 |
| | $UF_{max,\ 4}$ | 5.36 | 0.90 | 0.94 |
| | $UF_{max,\ 5}$ | 1.13 | 0.89 | 0.88 |
| Steel | $UF_{max,\ 6}$ | 3.60 | 0.91 | 0.83 |

# Chapter 5- Hydrodynamic Analysis

After a new design is created, a hydrodynamic analysis must be performed to extract the hydrodynamic properties. However, it is reasonable to adopt the same hydrodynamic properties provided for the UMaine VolturnUS-S semisubmersible platform if the new design has:

- Identical geometry
- Same total mass
- Identical location of the Center of Gravity (CoG)

$$x_{CoG} = \frac{\int X_i \, m_i dm}{M} \tag{5.1}$$

$$y_{CoG} = \frac{\int Y_i \, m_i dm}{M} \tag{5.2}$$

$$z_{CoG} = \frac{\int Z_i \, m_i dm}{M} \tag{5.3}$$

Where, $m_i$ is the mass of each infinitesimally small component of the model, $(X_i, Y_i, Z_i)$ are coordinates of the $i^{th}$ component's CoG in the system, and M is the total mass.

- Identical location of the Center of Buoyancy (CoB). This condition is already implied once the first three conditions are met.
- Identical values for the mass moment of inertia about all the three axis $I_{xx}, I_{yy}, I_{zz}$ to ensure that the distribution of the mass about each axis of rotation is identical. In other words, the model resistance to rotational motion/acceleration about each axis must be the same. Moment of inertia is the sum/integral of the products of the mass of each component in the model with the square of its distance from the axis of rotation:

$$I = \int dI = \int m_i \, r_i^{\,2} \, dm \tag{5.4}$$

Where $r_i$ is the perpendicular distance between the $i^{th}$ component's CoG and the axis of rotation.

To ensure that all 5 conditions are met, the new model is created again using SolidWorks to ensure effective and accurate results and to avoid complex hand calculations as much as possible. The design is simplified and completed by taking the connection part of the platform as a point of mass since no detailed information about the connection design was provided in

the original documentation of the UMaine VolturnUS-S platform (Allen et al., 2020). The conditions are met by adjusting the mass and location of fluid/fixed ballast following the steps below, see Figure 5.1:

1- The total mass and other mass properties of the entire hybrid structure without ballast were calculated.

2- Water mass is assumed to be 11300 t, which is the same as for the original model and it occupies the lower part on the pontoons and the 4 columns.

3- To achieve identical values of $I_{xx}$, $I_{yy}$, $I_{zz}$, three cylindrical ballast masses made of concrete with a density of 2700 kg/m$^3$ were added to each of the three radial columns. The weights of the cylindrical masses were adjusted simultaneously to achieve this goal.

4- To achieve the identical mass condition, the total mass is compared against the UMaine VolturnUS-S mass. Since the calculated total mass was less, a fourth cylindrical concrete mass is added to the central column.

5- The last step is to adjust the vertical location of all 4 cylindrical concrete masses to achieve identical CoG in the z-direction. Both the suggested design and the original design are axisymmetric around the z-axis, and therefore the (y,z) coordinates of their CoGs are (0,0).
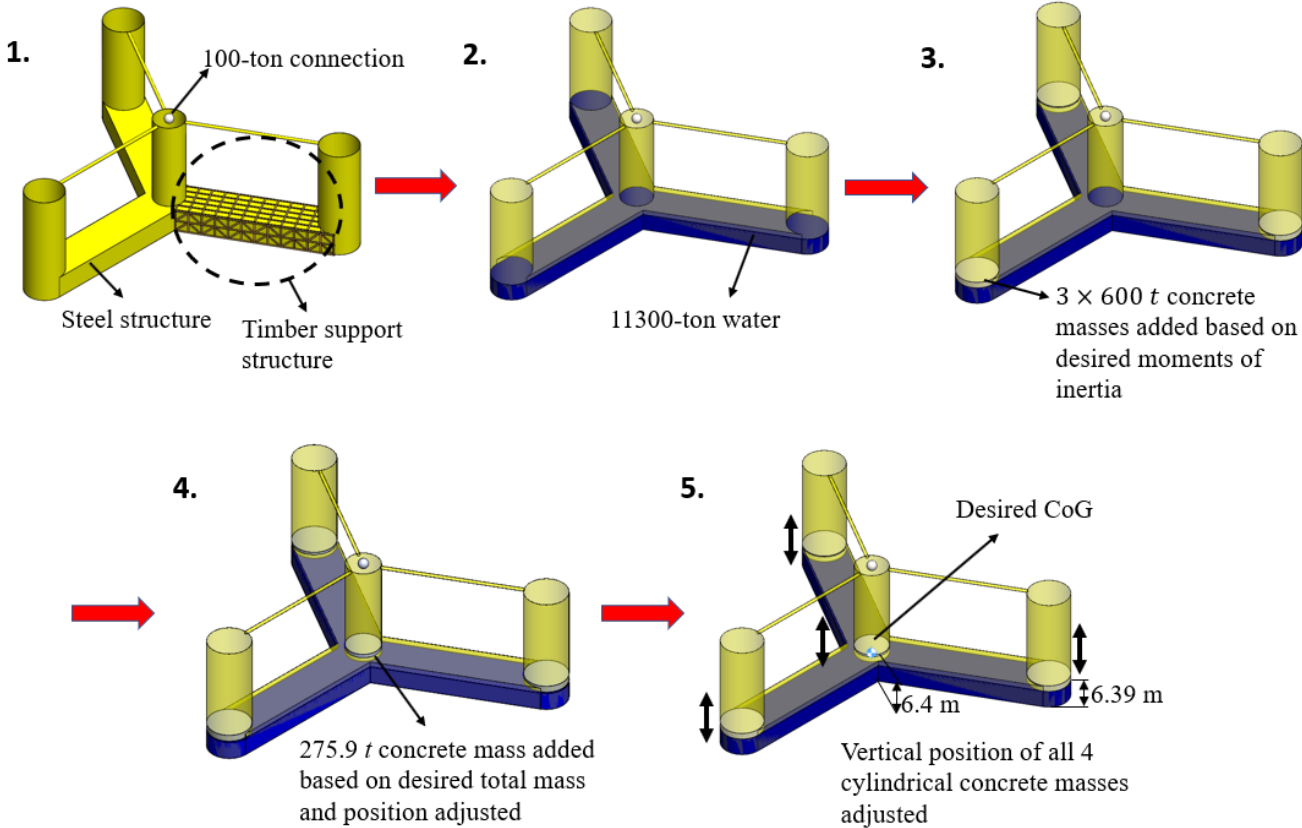


Figure 5.1: The main steps to adjust the hybrid design to have the same hydrodynamic properties as the UMaine VolturnUS-S semisubmersible platform

66

Table 5.1 shows that the hybrid floater and the UMaine VolturnUS-S semisubmersible platforms have identical COB, COG, mass, and moments of inertia with a considerable reduction in the steel and concrete mass, around 590 t and 469 t respectively. Additionally, the external dimensions and geometry of the hybrid floater are the same as for the UMaine VolturnUS-S platform. Based on that, the requirements regarding stability and eigenfrequency are automatically fulfilled and the hydrodynamic properties provided for the UMaine VolturnUS-S platform can be utilized for the analysis of the hybrid floater.

Table 5.2, Table 5.3, and Table 5.4 present the hydrostatic stiffness, infinite frequency added mass, and viscous damping of the hybrid floater based on similarity with the UMaine VolturnUS-S platform, respectively (Allen et al., 2020). The model was also checked to verify that the pontoons have enough available volume to take the 11300 t ballast water in the presence of all timber beams.

Table 5.1: Comparison between the hybrid platform and the UMaine VolturnUS-S platform

| Parameter | UMaine VolturnUS-S platform | Hybrid timber-steel platform | Unit |
|---|---|---|---|
| Total mass | 17854 | 17854.03 | t |
| Hull displacement | 20,206 | 20,206 | $m^3$ |
| Hull steel mass | 3914 | 3323.90 | t |
| Hull timber mass | - | 1053.56 | t |
| Tower interface mass | 100 | 100 | t |
| Ballast mass (fixed/fluid) | 2,544/11,300 | 2075.04 /11,301 | t |
| Draft | 20 | 20 | m |
| Freeboard | 15 | 15 | m |
| Vertical CoG from SWL | -14.94 | -14.94 | m |
| Vertical CoB from SWL | -13.63 | -13.63 | m |
| Roll inertia about CoG | 1.251E+10 | 1.256E+10 | $Kg. m^2$ |
| Pitch inertia about CoG | 1.251E+10 | 1.256E+10 | $Kg. m^2$ |
| Yaw inertia about CoG | 2.367E+10 | 2.363E+10 | $Kg. m^2$ |

Table 5.2: Floater hydrostatic stiffness (N/m, N/rad or N.m/rad) (Allen et al., 2020)

|          | Surge | Sway | Heave    | Roll     | Pitch    | Yaw |
|----------|-------|------|----------|----------|----------|-----|
| **Surge** | 0     | 0    | 0        | 0        | 0        | 0   |
| **Sway**  | 0     | 0    | 0        | 0        | 0        | 0   |
| **Heave** | 0     | 0    | 4.47E+06 | 0        | 0        | 0   |
| **Roll**  | 0     | 0    | 0        | 2.19E+09 | 0        | 0   |
| **Pitch** | 0     | 0    | 0        | 0        | 2.19E+09 | 0   |
| **Yaw**   | 0     | 0    | 0        | 0        | 0        | 0   |

Table 5.3: Floater infinite frequency added mass (kg, kg.m or kg. m$^2$) (Allen et al., 2020)

|          | Surge      | Sway     | Heave    | Roll     | Pitch     | Yaw      |
|----------|------------|----------|----------|----------|-----------|----------|
| **Surge** | 9.64E+06  | 0        | 0        | 0        | -1.01E+08 | 0        |
| **Sway**  | 0         | 9.64E+06 | 0        | 1.01E+08 | 0         | 0        |
| **Heave** | 0         | 0        | 2.48E+07 | 0        | 0         | 0        |
| **Roll**  | 0         | 0        | 0        | 1.16E+10 | 0         | 0        |
| **Pitch** | -1.01E+08 | 0        | 0        | 0        | 1.16E+10  | 0        |
| **Yaw**   | 0         | 0        | 0        | 0        | 0         | 2.01E+10 |

Table 5.4: Floater viscous damping (N.s$^2$/m$^2$ , N.s$^2$, N.s$^2$/m, or N.m.s$^2$) (Allen et al., 2020)

|          | Surge      | Sway      | Heave     | Roll      | Pitch      | Yaw       |
|----------|------------|-----------|-----------|-----------|------------|-----------|
| **Surge** | 9.225E+05 | 0         | 0         | 0         | -8.918E+06 | 0         |
| **Sway**  | 0         | 9.225E+05 | 0         | 8.918E+06 | 0          | 0         |
| **Heave** | 0         | 0         | 2.296E+06 | 0         | 0          | 0         |
| **Roll**  | 0         | 8.918E+06 | 0         | 1.676E+10 | 0          | 0         |
| **Pitch** | -8.918E+06 | 0        | 0         | 0         | 1.676E+10  | 0         |
| **Yaw**   | 0         | 0         | 0         | 0         | 0          | 4.798E+10 |

# Chapter 6- Fully Coupled Dynamic Analysis

## 6.1 OpenFAST

OpenFAST is a multi-physics, nonlinear, open-source tool for modeling the fully coupled dynamic response of wind turbines (National Renewable Energy Laboratory (NREL), n.d.-b). OpenFAST is managed and developed by the National Renewable Laboratory team (NREL) with the intention of making it a community-developed model that can easily be accessed by academic institutions, businesses, and other research labs. OpenFAST is a "glue code"/framework that connects/glues together the calculations obtained from different computational modules to perform nonlinear aero-hydro-servo-elastic simulation in the time domain. The coupling between the different modules used in the IEA 15MW FWT such as ElastoDyn, inflowWind, AeroDyn, ServoDyn, and HydroDyn together with the input from other supporting NREL programs such as MoorDyn and TurbSim is shown in Figure 6.1. More information about OpenFAST and the different modules can be found in OpenFAST's complete documentation, which is available online at the readthedocs website (National Renewable Energy Laboratory (NREL), n.d.-b), in the FAST Forum (National Renewable Energy Laboratory (NREL), n.d.-a), and on GitHub (National Renewable Energy Laboratory (NREL)).
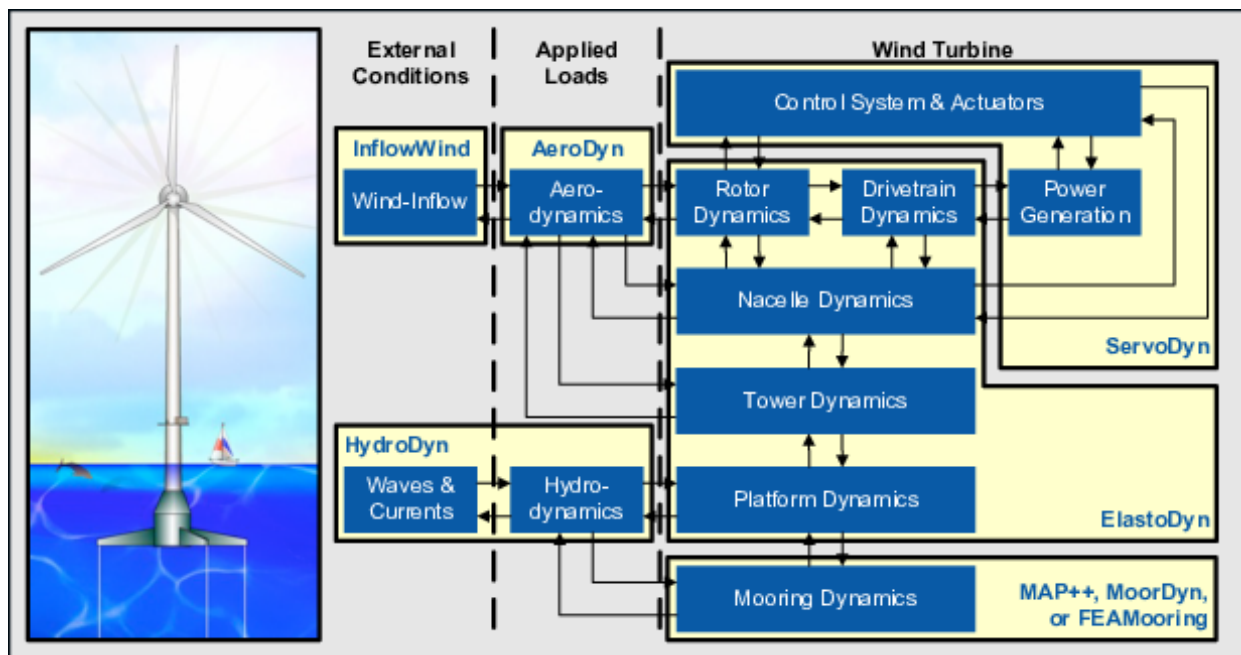


Figure 6.1: OpenFAST schematic (National Renewable Energy Laboratory (NREL), n.d.-b)

The OpenFAST modules used for this work are listed below.

### 6.1.1 AeroDyn V15

AeroDyn is a time-domain unit/module that utilizes the wind field data, obtained by TurbSim and processed by InfowWind, to compute the aerodynamic loads (drag, lift, and pitching moments) on the blades as well as the tower. These aerodynamic loads are determined based on the actuator line theory where a local 2D flow around a cross-section is used to approximately represent the actual flow around a 3D body. Subsequently, the 2D aerodynamic loads are integrated along the entire length to obtain the complete 3D aerodynamic loads. Further information is available on the OpenFAST documentation page (Pedersen & Askheim, 2021).

### 6.1.2 HydroDyn

HydroDyn is a time-domain unit/module that supports different approaches to determine the hydrodynamic loads on offshore structures including potential theory, strip theory, or a hybrid approach that combines both. Waves generated in HydroDyn can be regular (with user-specified phase feature) or irregular (either from Pierson-Moskowitz/ JONSWAP spectrum, from white noise spectrum, or irregular with user-defined spectrum), and short-crested or long-crested. HydroDyn creates these waves analytically for limited depths using first-order (linear Airy) or first-plus-second-order wave theory with the option of providing directional spreading. The calculations of wave kinematics are performed in the region bounded by the horizontal seabed and the SWL. If desired, wave stretching can be used to estimate the wave kinematics and the forces it exerts on all nodes within the fluid region, up to the instantaneous surface elevation, which is above the SWL in a wave crest and below it in a wave trough. The effect of the radiation memory can be obtained either by convolution or by a linear state-space approach with a state-space model. HydroDyn does not only calculate waves but also current (National Renewable Energy Laboratory (NREL), n.d.-b).

For the hybrid platform, the solution for the potential flow theory is applied since the structure is significantly larger than the wavelength. The hydrodynamic loads are obtained based on the transformation from the frequency domain to the time domain and include added mass and damping coefficients from linear wave radiation (free-surface memory effects are considered), linear hydrostatic restoring, and the incident-wave excitation force obtained from first-and second-order diffraction (FK and scattering)). The frequency-dependent hydrodynamic coefficients were taken similar to the one used for the UMaine VolturnUS-S semisubmersible platform which are obtained using the frequency domain panel code (WAMIT). Wave

stretching, current, and $2^{nd}$-order floating platform forces (obtained from the full difference- and sum-frequency quadratic transfer functions (QTFs) or the difference-frequency) were not included in this work.

### 6.1.3 ServoDyn

The module responsible for the control and electrical system dynamics in OpenFAST is called ServoDyn. This model provides models to control nacelle yaw, blade pitch angle, blade-tip brakes, generator torque, and shaft brake. The controller used in the IEA 15 MW FWT is the NREL's Reference OpenSource Controller (ROSCO) (Pedersen & Askheim, 2021).

### 6.1.4 MoorDyn

MoorDyn is an open-source line model that has all the features required to simulate the dynamics of ordinary mooring systems. MoorDyn can be coupled with OpenFAST or it can be utilized alone as a mooring line simulator provided that the motions of fairleads are supplied from another separate data file. MoorDyn is capable of handling many line characteristics, clump weights and floats, and line interconnections. The model takes into account forces such as weight and buoyancy forces, hydrodynamic forces derived from Morison's equation, damping, and inner axial stiffness forces, and vertical spring-damper forces resulting from interaction with the seabed (Hall, 2015).

### 6.1.5 ElastoDyn

ElastoDyn is the module responsible for simulating the structural dynamics of offshore wind turbines including the platform, the tower, and the rotor-nacelle assembly. The main ElastoDyn input file specifies the parameters needed for various parts of the wind turbine with respect to the different degrees of freedom, turbine configuration, initial conditions, mass, inertia, tower, and blade files. The tower and blade files contain information about the distributed properties along the tower and blade. To use ElastoDyn, four tower mode shapes are required (two in the fore-aft direction and two in the side-to-side direction). These are usually expressed as polynomial coefficients which are obtained beforehand using the BModes module. ElastoDyn uses linear Euler-Bernoulli beam theory, which means that there are no axial or torsional degrees of freedom and no shear deformation. Using the Rayleigh-Ritz approach, the mode shapes obtained from BModes can be utilized as shape functions in the nonlinear model (Pedersen & Askheim, 2021).

### 6.1.6 TurbSim

TurbSim is a pre-processor tool for simulating turbulent wind. TurbSim adopts a statistical model to generate time series of three-component wind-velocity vectors that are stochastic, full-field, and time-dependent. These vectors represent wind velocities at various points within a 2D vertical rectangular grid that is fixed in space. TurbSim determines the velocity components' spectra and spatial coherence, which are represented in the frequency domain. The time series is then produced using an inverse Fourier transform (Jonkman, 2016).

### 6.1.7 InflowWind

The InflowWind module is responsible for processing wind inflow data that is produced by TurbSim. Different forms of wind fields, such as uniform, binary TurbSim full-field, binary Bladed-style full-field, or HAWC format, can be processed by InflowWind. An internal steady wind field calculation is also possible. The driver code provides the coordinates of different points to InflowWind, and the module returns the undisturbed wind inflow velocities at those coordinates (Pedersen & Askheim, 2021).

### 6.2 Design Load Cases (DLC)

The performance of the new hybrid floater is evaluated during normal and extreme operating conditions by choosing a subset of IEC design load case conditions (IEC-61400-1, 2005). The load cases, which are given in Table 6.1, were chosen based on the experience of similar systems to reflect the governing conditions for critical FWT components. It is important to note that all simulations were carried out with an aligned wind and wave heading of $0°$, as illustrated in Figure 2.18. The environmental conditions used in the design cases provide a good representation of the U.S. East Coast (Stewart et al., 2016; Viselli et al., 2015). All simulations are run for 720 s. However, there is some initial transient period before reaching the steady-state conditions, and therefore results from the first two minutes are neglected in this study.

Table 6.1: IEC Design Load Case (Allen et al., 2020; IEC-61400-1, 2005)

| DLC number | | Wind condition | $U_{hub}$ (m/s) | $H_s$ (m) | $T_p$ (s) | Gamma shape factor |
|---|---|---|---|---|---|---|
| 1.1 | 1 | NTM | 4.00 | 1.10 | 8.52 | 1.00 |
| | 2 | | 6.00 | 1.18 | 8.31 | 1.00 |
| | 3 | | 8.00 | 1.32 | 8.01 | 1.00 |
| | 4 | | 10.00 | 1.54 | 7.65 | 1.00 |
| | 5 | | 12.00 | 1.84 | 7.44 | 1.00 |
| | 6 | | 14.00 | 2.19 | 7.46 | 1.00 |
| | 7 | | 16.00 | 2.60 | 7.64 | 1.35 |
| | 8 | | 18.00 | 3.06 | 8.05 | 1.59 |
| | 9 | | 20.00 | 3.62 | 8.52 | 1.82 |
| | 10 | | 22.00 | 4.03 | 8.99 | 1.82 |
| | 11 | | 24.00 | 4.52 | 9.45 | 1.89 |
| 1.3 | 12 | ETM | 4.00 | 1.10 | 8.52 | 1.00 |
| | 13 | | 6.00 | 1.18 | 8.31 | 1.00 |
| | 14 | | 8.00 | 1.32 | 8.01 | 1.00 |
| | 15 | | 10.00 | 1.54 | 7.65 | 1.00 |
| | 16 | | 12.00 | 1.84 | 7.44 | 1.00 |
| | 17 | | 14.00 | 2.19 | 7.46 | 1.00 |
| | 18 | | 16.00 | 2.60 | 7.64 | 1.35 |
| | 19 | | 18.00 | 3.06 | 8.05 | 1.59 |
| | 20 | | 20.00 | 3.62 | 8.52 | 1.82 |
| | 21 | | 22.00 | 4.03 | 8.99 | 1.82 |
| | 22 | | 24.00 | 4.52 | 9.45 | 1.89 |
| 1.6 | 23 | NTM | 4.00 | 6.30 | 11.50 | 2.75 |
| | 24 | | 6.00 | 8.00 | 12.70 | 2.75 |
| | 25 | | 8.00 | 8.00 | 12.70 | 2.75 |
| | 26 | | 10.00 | 8.10 | 12.80 | 2.75 |
| | 27 | | 12.00 | 8.50 | 13.10 | 2.75 |
| | 28 | | 14.00 | 8.50 | 13.10 | 2.75 |
| | 29 | | 16.00 | 9.80 | 14.10 | 2.75 |
| | 30 | | 18.00 | 9.80 | 14.10 | 2.75 |
| | 31 | | 20.00 | 9.80 | 14.10 | 2.75 |
| | 32 | | 22.00 | 9.80 | 14.10 | 2.75 |
| | 33 | | 24.00 | 9.80 | 14.10 | 2.75 |

Where:

ETM – Extreme turbulence model

NTM – Normal turbulence model

# Chapter 7- Local Analysis Results

## 7.1 FEA Model

The next step is to re-analyze the hybrid model using the actual loads obtained from OpenFAST. Material properties, mesh type, and mesh refinement are kept with no change. Figure 7.1 illustrates the loads and boundary conditions adopted for the local design including hydrostatic pressure, tower base force, tower base moment, and mooring line tension forces.



A  Pinned support
B  Variable Load: Variable hydrostatic pressure (side plate 6)
C  Constant hydrostatic pressure on top plate: 1,3072e+005 Pa
D  Constant hydrostatic pressure on bottom plate: 2,0111e+005 Pa
E  Variable Load: Variable hydrostatic pressure (side plate 1)
F  Variable Load: Variable hydrostatic pressure (fairled plate 1)
G  Variable Load: Variable hydrostatic pressure (fairled plate 2)
H  Variable Load: Variable hydrostatic pressure (fairled plate 3)
I  Variable Load: Variable hydrostatic pressure (side plate 2)
J  Variable Load: Variable hydrostatic pressure (side plate 3)

TwrBs force (N)
TwrBs moment (N.m)
FAIRTEN2 (N)
FAIRTEN1(N)

Figure 7.1: Actual loads and boundary conditions defined for the hybrid design during local analysis, configuration (b) (ANSYS)

## 7.2 Response Surface Methodology (RSM)

The loads obtained from OpenFAST are usually given in a time series format. To capture the response of the model accurately and to secure the safety of the suggested design, it is necessary to simulate each of the load combinations obtained in the 720 s-long simulation (with time step $\Delta t = 0.025$ s). However, to make the analysis computationally feasible, only worst-case load combinations that yield maximum utilization factor must be considered. The number of the worst-case load combinations can still be large, and RSM can be used to reduce the computational time by avoiding the need for running thousands of simulations based on the different load combinations (obtained at each time step during the simulation length).

RSM is a statistical method that investigates the relationships between several inputs and one or more outputs based on mathematical regression. The approach was first introduced by George E. P. Box and K. B. Wilson in 1951 (Box & Wilson, 1951), and it includes using a sequence of designed experiments to find an optimal response.

In this thesis, a set of design points are produced using the Design of the Experiment technique (DoE) provided in Ansys Workbench 2020 R1. After, a response surface is created to predict the utilization factors at any load combination. Subsequently, a correlation study is conducted to highlight which inputs have significant influence on the output. Based on that, worst-case scenarios, corresponding to the maximum/minimum values for each of the highlighted inputs, are selected to check whether the design criteria are fulfilled or not.

## 7.2.1 Generation of design points (DoE)

There are many ways to produce experimental design points in ANSYS Workbench including optimal space-filling design, Latin hypercube sampling, central composite design, and Box–Behnken design, etc. For this thesis, only the central composite design is considered.

Eight input variables are considered, and 285 design points were produced. The input variables include TwrBsFxt, TwrBsFyt, TwrBsFzt, TwrBsMxt, TwrBsMyt, TwrBsMzt which are the x,y, and z components of the tower base force and moment, and FAIRTEN1, FAIRTEN2 which are the tension forces on the unsupported fairleads. The output variables are the maximum utilization factors for all 6 design criteria represented in Eq. (3.4), Eq. (3.5), Eq. (3.6), Eq. (3.7), Eq. (3.8), and Eq. (3.22), respectively.

The upper and lower bounds were selected by looking into the maximum and minimum values for all DLC, and to include all the values that the input variables might have, see Table 7.1.

Table 7.1: Upper and lower bounds assigned for input variables in DoE

|  | TwrBsFxt | TwrBsFyt | TwrBsFzt | TwrBsMxt | TwrBsMyt | TwrBsMzt | FAIRTEN1 | FAIRTEN2 |
|---|---|---|---|---|---|---|---|---|
| **Lower bound** | -3E+06 | -2E+06 | -3E+07 | -8E+07 | -4E+08 | -4E+07 | 1E+06 | 1E+06 |
| **Upper bound** | 9E+06 | 2E+06 | 3E+07 | 2E+08 | 7E+08 | 4E+07 | 6E+06 | 3E+06 |

## 7.2.2 Zero force/moment problem

Each of the three components of the tower base force or moment fluctuates between positive and negative values, which might create a problem when deciding the upper and lower bounds in the DOE, particularly when using the central composite design option. The complication arises when a negative value is set for the lower bound and a positive value for the upper bound, as the DOE could sample a force or moment value of zero, ultimately causing a failure of the conducted experiment. To avoid this problem, one extra DoE dummy input (marked with *) was created for each of the 6 load components. By having two inputs, the first one is set to represent the component's negative values and the second is to represent its positive values. The DoE layout and the 6 extra dummy components are shown in Figure 7.2.
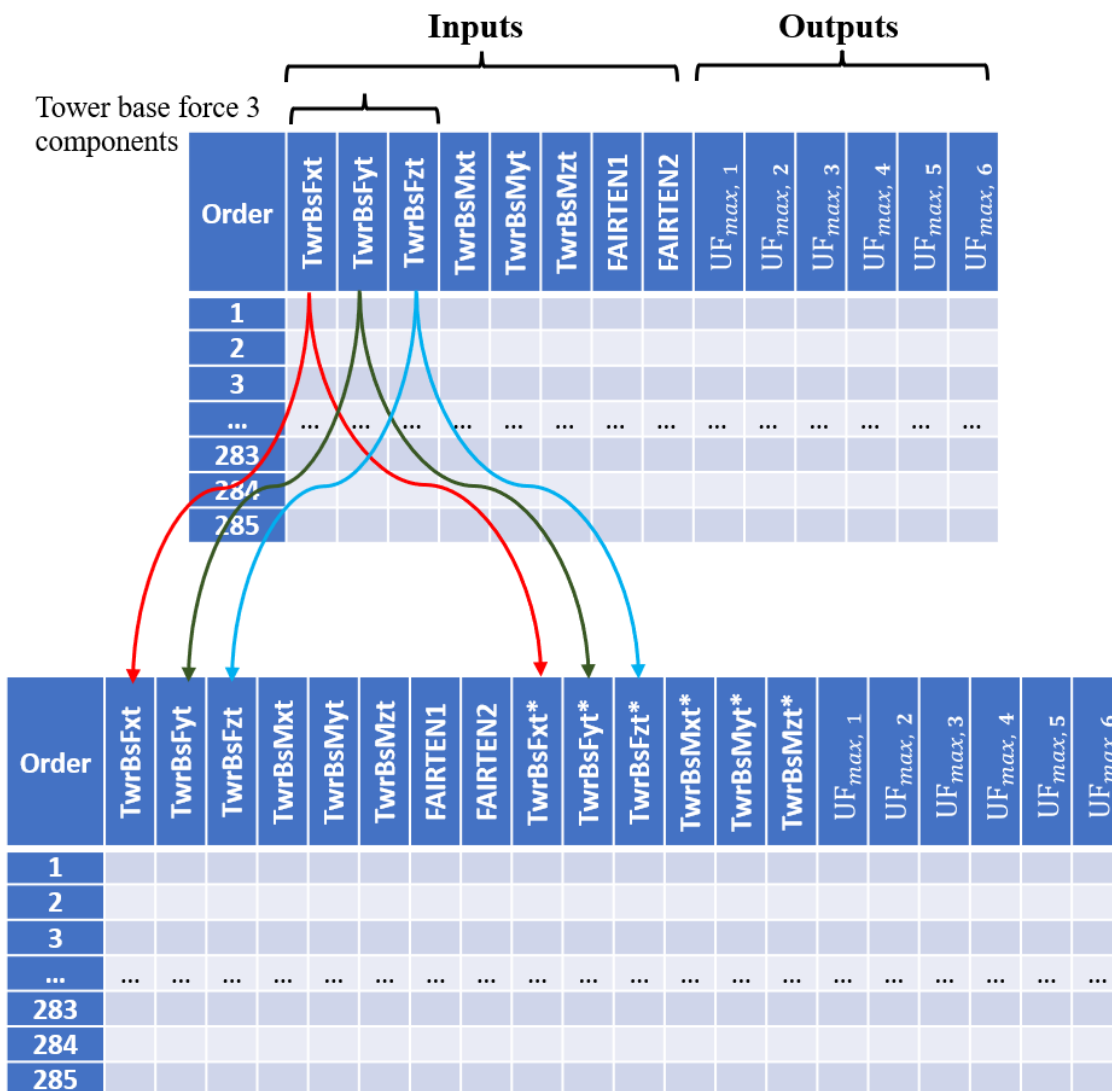


Figure 7.2: Design points table layout for the design of experiment DoE

### 7.2.3 Construction of response surface

There are many ways to construct the response surface within ANSYS Workbench, such as Kriging, standard second-order, non-parametric regression, etc. In this thesis, the response surface is created using generic aggregation, which employs a genetic algorithm to simultaneously solve many types of response surfaces while considering the stability and accuracy of the response surface at the design point. The mathematical representation of the generic aggregation method is given by Eq.(7.1) (ANSYS).

$$\hat{y}_{ens}(x) = \sum_{i=1}^{N_m} w_i \cdot \hat{y}_i(x) \tag{7.1}$$

Where $\hat{y}_{ens}$ is the ensemble prediction, $N_m$ is the total number of used metamodels and $\hat{y}_i$, $w_i$ are the prediction and weight factor of response surface number $i$, respectively.

### 7.2.4 Response surface verification

To check the quality of the response surface, Ansys workbench provides what is called **goodness of fit** criteria which compares the response surface outputs with the DOE results that were used to produce them. Goodness of fit criteria utilizes several matrices to evaluate the response surface such as coefficient of determination, maximum relative residual, root mean square error relative root mean square error, etc, see Eq. (7.2) to (7.5) (ANSYS).

$$\text{Coefficient of Determination} = 1 - \frac{\sum_{i=1}^{N}(y_i - \hat{y}_i)^2}{\sum_{i=1}^{N}(y_i - \bar{y})^2} \tag{7.2}$$

$$\text{Maximum Relative Residual} = Max_{(i=1:N)}\left(Abs\left(\frac{y_i - \hat{y}_i}{y_i}\right)\right) \tag{7.3}$$

$$\text{Root Mean Square Error} = \sqrt{\frac{1}{N}\sum_{i=1}^{N}(y_i - \hat{y}_i)^2} \tag{7.4}$$

$$\text{Relative Root Mean Square Error} = \sqrt{\frac{1}{N}\sum_{i=1}^{N}\left(\frac{y_i - \hat{y}_i}{y_i}\right)^2} \tag{7.5}$$

Table 7.2 shows that the response surface generated using generic aggregation presents a good fit for the model.

Table 7.2: Goodness of fit results

| | $UF_{max,\ 1}$ | $UF_{max,\ 2}$ | $UF_{max,\ 3}$ | $UF_{max,\ 4}$ | $UF_{max,\ 5}$ | $UF_{max,\ 6}$ |
|---|---|---|---|---|---|---|
| Coefficient of Determination (best value=1) | | | | | | |
| Learning Points | 1 | 0.999 | 0.999 | 1 | 0.999 | 1 |
| Cross-Validation on Learning Points | 0.979 | 0.990 | 0.946 | 0.907 | 0.957 | 0.948 |
| Maximum Relative Residual (best value=0%) | | | | | | |
| Learning Points | 0 | 0.208 | 0.055 | 0 | 0.183 | 0 |
| Verification Points | 3.221 | 1.755 | 7.290 | 6.449 | 3.183 | 1.564 |
| Cross-Validation on Learning Points | 2.726 | 2.185 | 7.172 | 8.251 | 4.040 | 1.818 |
| Root Mean Square Error (best value=0) | | | | | | |
| Learning Points | 0 | 0 | 0 | 0 | 0 | 0 |
| Verification Points | 0.017 | 0.009 | 0.027 | 0.032 | 0.014 | 0.006 |
| Cross-Validation on Learning Points | 0.003 | 0.003 | 0.009 | 0.01 | 0.005 | 0.002 |
| Relative Root Mean Square Error (best value=0%) | | | | | | |
| Learning Points | 0 | 0.048 | 0.04 | 0 | 0.059 | 0 |
| Verification Points | 2.164 | 1.188 | 3.907 | 4.253 | 1.667 | 0.797 |
| Cross-Validation on Learning Points | 0.397 | 0.41 | 1.122 | 1.201 | 0.517 | 0.239 |

## 7.3 Parameter Correlation Analysis

To ensure that the design process is effective and time-efficient, it is necessary to perform a parametric correlation study. The hybrid-floater design is relatively complex, and a parameter correlation study is needed to gain a better understanding of how changing a certain input will affect the outputs. More precisely, how changing any of the time-varying loads on the hybrid floater will affect the different design criteria. Based on that, the focus can be shifted to those inputs that have the biggest influence only. This can have a crucial influence on design efficiency for two reasons. Firstly, it allows for the detection of the worst-case load combinations while considering fewer inputs at their maximum/minimum values. Secondly, it simplifies the optimization process and allows us to take informed decisions regarding necessary design modifications. The correlation study outcome is usually represented in a form of an $n \times n$ correlation matrix. This matrix contains correlation coefficients that vary between -1 and +1. A positive correlation coefficient means the output value increases when the input

value increases, and vice versa (Meissner, 2013). Guilford has proposed a categorization of the coefficient of correlation, which is shown in Table 7.3, to indicate how strong the correlation between the parameters is  (Guilford, 1950).

Table 7.3: Categorization of the coefficient of correlation

| Correlation coefficient's value | The strength of the relationship |
|:---:|:---:|
| < 0.2 | negligible correlation |
| 0.2 – 0.4 | low correlation |
| 0.4 – 0.7 | moderate correlation |
| 0.70 – 0.90 | high correlation |
| 0.90 < | very high and dependable correlation |

Table 7.5, Table 7.6, and Table 7.7 show $14 \times 14$ Pearson's correlation matrices for three different design load cases using ANSYS DesignXplorer. Pearson's correlation approach calculates the linear correlation coefficient between two variables $P_1$ and $P_2$ using Eq. (7.6).

$$\rho_{P_1,P_2} = \frac{cov(P_1, P_2)}{\sigma_{P_1} \sigma_{P_2}} \tag{7.6}$$

Where $cov(P_1, P_2)$ is the covariance, $\sigma_{P_1}$ is the standard deviation for variable $P_1$ and $\sigma_{P_2}$ is the standard deviation for variable $P_2$ (Pearson, 1896, 1920).

The results from Table 7.5, Table 7.6, and Table 7.7 illustrate that the correlation coefficients between the load inputs and the output criteria vary significantly between the three cases, especially for the tower base loads. The change in the direction of each load is the key to understanding this phenomenon. In general, all tower base loads are acting on the middle part of the floater and their effect will be limited to the supported pontoon only. However, stresses are still produced in the two remaining pontoons when these time-varying loads act against the mooring line's tension and the correlation with the output criteria will be to a large degree depending on the direction of each of the tower base loads. For instance, if we consider the z-component of tower base force TwBsFzt as the only load acting on the tower base, we can see that this load has a negative correlation with most of the criteria when it is pointing in the positive z-direction. An opposite trend (positive correlation) is captured when TwrBsFzt is pointing in the negative z-direction, see Table 7.4.

The green regions in Table 7.5, Table 7.6, and Table 7.7 show the correlation between input and output (the region of interest). High and very high correlation values are highlighted in red,

while moderate correlation values are highlighted in blue. The results obtained from these tables show that TwrBsFxt, TwrBsFzt, TwrBsMyt, FAIRTEN1, and FAIRTEN2 have correlation coefficients that vary significantly in value and sign. Based on that, it will not be possible to determine the type of correlation (positive or negative) or the strength of the correlation for these loads. However, the fact that these coefficients are changing significantly shows the importance of considering the corresponding load inputs to determine the worst-case load combinations for each DLC.

Table 7.4: The change in correlation as a result of changing the direction of TwrBsFzt force

| TwrBsFzt | $UF_{max,\ 1}$ | $UF_{max,\ 2}$ | $UF_{max,\ 3}$ | $UF_{max,\ 4}$ | $UF_{max,\ 5}$ | $UF_{max,\ 6}$ |
|---|---|---|---|---|---|---|
| $10^2$ | 0.755 | 0.790 | 0.720 | 0.740 | 0.899 | 0.810 |
| $2 \times 10^7$ | 0.750 | 0.781 | 0.720 | 0.737 | 0.897 | 0.810 |
| $2 \times 10^{10}$ | 0.750 | 0.779 | 0.718 | 0.735 | 0.896 | 0.805 |
| $-10^2$ | 0.755 | 0.790 | 0.717 | 0.738 | 0.898 | 0.810 |
| $-2 \times 10^7$ | 0.758 | 0.795 | 0.730 | 0.748 | 0.902 | 0.816 |
| $-2 \times 10^{10}$ | 0.759 | 0.799 | 0.733 | 0.750 | 0.905 | 0.819 |

Table 7.5: Pearson's correlation matrix for DLC (1.1-1)

| | TwrBsFxt | TwrBsFyt | TwrBsFzt | TwrBsMxt | TwrBsMyt | TwrBsMzt | FAIRTEN1 | FAIRTEN2 | $UF_{max,\ 1}$ | $UF_{max,\ 2}$ | $UF_{max,\ 3}$ | $UF_{max,\ 4}$ | $UF_{max,\ 5}$ | $UF_{max,\ 6}$ |
|---|---|---|---|---|---|---|---|---|---|---|---|---|---|---|
| TwrBsFxt | 1 | 0.104 | 0.062 | -0.139 | 0.917 | -0.400 | 0.342 | -0.232 | -0.342 | -0.343 | -0.360 | -0.360 | -0.342 | -0.342 |
| TwrBsFyt | | 1 | -0.082 | -0.990 | 0.113 | -0.269 | -0.114 | -0.131 | 0.114 | 0.112 | 0.121 | 0.230 | 0.114 | 0.240 |
| TwrBsFzt | | | 1 | 0.051 | 0.262 | -0.192 | 0.252 | -0.725 | -0.252 | -0.254 | -0.300 | -0.320 | -0.331 | -0.257 |
| TwrBsMxt | | | | 1 | -0.162 | 0.347 | 0.093 | 0.167 | -0.092 | -0.091 | -0.085 | -0.085 | -0.093 | -0.112 |
| TwrBsMyt | | | | | 1 | -0.554 | 0.613 | -0.542 | -0.613 | -0.618 | -0.711 | -0.713 | -0.801 | -0.613 |
| TwrBsMzt | | | | | | 1 | -0.331 | 0.414 | 0.331 | 0.332 | 0.295 | 0.307 | 0.331 | 0.365 |
| FAIRTEN1 | | | | | | | 1 | -0.710 | -1 | -1 | -0.972 | -0.930 | -0.999 | -0.980 |
| FAIRTEN2 | | | | | | | | 1 | 0.712 | 0.715 | 0.695 | 0.699 | 0.710 | 0.715 |
| $UF_{max,\ 1}$ | | | | | | | | | 1 | 1 | 1 | 1 | 1 | 1 |
| $UF_{max,\ 2}$ | | | | | | | | | | 1 | 1 | 1 | 1 | 1 |
| $UF_{max,\ 3}$ | | | | | | | | | | | 1 | 1 | 1 | 1 |
| $UF_{max,\ 4}$ | | | | | | | | | | | | 1 | 1 | 1 |
| $UF_{max,\ 5}$ | | | | | | | | | | | | | 1 | 1 |
| $UF_{max,\ 6}$ | | | | | | | | | | | | | | 1 |

Table 7.6: Pearson's correlation matrix for DLC (1.3-12)

| | TwrBsFxt | TwrBsFyt | TwrBsFzt | TwrBsMxt | TwrBsMyt | TwrBsMzt | FAIRTEN1 | FAIRTEN2 | $UF_{max,1}$ | $UF_{max,2}$ | $UF_{max,3}$ | $UF_{max,4}$ | $UF_{max,5}$ | $UF_{max,6}$ |
|---|---|---|---|---|---|---|---|---|---|---|---|---|---|---|
| TwrBsFxt | 1 | 0.381 | 0.319 | -0.392 | 0.957 | -0.371 | 0.651 | -0.568 | -0.651 | -0.648 | -0.659 | -0.658 | -0.621 | -0.653 |
| TwrBsFyt | | 1 | -0.028 | -0.980 | 0.269 | -0.259 | -0.018 | -0.150 | 0.017 | 0.017 | 0.018 | 0.018 | 0.019 | 0.013 |
| TwrBsFzt | | | 1 | 0.012 | 0.496 | -0.277 | 0.524 | -0.775 | -0.524 | -0.525 | -0.501 | -0.495 | -0.567 | -0.561 |
| TwrBsMxt | | | | 1 | -0.295 | 0.389 | 0.004 | 0.177 | -0.004 | -0.004 | -0.003 | -0.004 | -0.005 | -0.004 |
| TwrBsMyt | | | | | 1 | -0.432 | 0.809 | -0.760 | -0.809 | -0.812 | -0.900 | -0.850 | -0.952 | -0.815 |
| TwrBsMzt | | | | | | 1 | -0.276 | 0.358 | 0.276 | 0.286 | 0.377 | 0.372 | 0.271 | 0.357 |
| FAIRTEN1 | | | | | | | 1 | -0.868 | -1 | -1 | -0.989 | -0.990 | -0.991 | -0.999 |
| FAIRTEN2 | | | | | | | | 1 | 0.868 | 0.897 | 0.928 | 0.957 | 0.876 | 0.857 |
| $UF_{max,1}$ | | | | | | | | | 1 | 1 | 1 | 1 | 1 | 1 |
| $UF_{max,2}$ | | | | | | | | | | 1 | 1 | 1 | 1 | 1 |
| $UF_{max,3}$ | | | | | | | | | | | 1 | 1 | 1 | 1 |
| $UF_{max,4}$ | | | | | | | | | | | | 1 | 1 | 1 |
| $UF_{max,5}$ | | | | | | | | | | | | | 1 | 1 |
| $UF_{max,6}$ | | | | | | | | | | | | | | 1 |

Table 7.7: Pearson's correlation matrix for DLC (1.6-23)

| | TwrBsFxt | TwrBsFyt | TwrBsFzt | TwrBsMxt | TwrBsMyt | TwrBsMzt | FAIRTEN1 | FAIRTEN2 | $UF_{max,1}$ | $UF_{max,2}$ | $UF_{max,3}$ | $UF_{max,4}$ | $UF_{max,5}$ | $UF_{max,6}$ |
|---|---|---|---|---|---|---|---|---|---|---|---|---|---|---|
| TwrBsFxt | 1 | 0.137 | -0.071 | -0.149 | 0.952 | -0.181 | 0.106 | 0.268 | -0.106 | -0.107 | -0.111 | -0.109 | -0.105 | -0.108 |
| TwrBsFyt | | 1 | 0.038 | -0.982 | 0.139 | -0.335 | -0.116 | -0.048 | 0.116 | 0.120 | 0.351 | 0.324 | 0.242 | 0.0-296 |
| TwrBsFzt | | | 1 | -0.034 | 0.084 | -0.027 | -0.241 | -0.770 | 0.340 | 0.320 | 0.240 | 0.220 | 0.241 | 0.246 |
| TwrBsMxt | | | | 1 | -0.160 | 0.446 | 0.111 | 0.048 | -0.111 | -0.115 | -0.090 | -0.086 | -0.111 | -0.114 |
| TwrBsMyt | | | | | 1 | -0.270 | 0.231 | 0.099 | -0.231 | -0.231 | -0.155 | -0.162 | -0.231 | -0.275 |
| TwrBsMzt | | | | | | 1 | -0.024 | 0.019 | 0.024 | 0.024 | 0.025 | 0.025 | 0.024 | 0.024 |
| FAIRTEN1 | | | | | | | 1 | -0.141 | -0.995 | -0.994 | -1 | -1 | -0.988 | -0.980 |
| FAIRTEN2 | | | | | | | | 1 | 0.149 | 0.156 | 0.260 | 0.230 | 0.115 | 0.140 |
| $UF_{max,1}$ | | | | | | | | | 1 | 1 | 1 | 1 | 1 | 1 |
| $UF_{max,2}$ | | | | | | | | | | 1 | 1 | 1 | 1 | 1 |
| $UF_{max,3}$ | | | | | | | | | | | 1 | 1 | 1 | 1 |
| $UF_{max,4}$ | | | | | | | | | | | | 1 | 1 | 1 |
| $UF_{max,5}$ | | | | | | | | | | | | | 1 | 1 |
| $UF_{max,6}$ | | | | | | | | | | | | | | 1 |

## 7.4 Results and Discussion

Table 7.8 shows the maximum utilization factors obtained from worst-case load combinations for each of the design load cases. All worst-case load combinations corresponding to the minimum or maximum of any of the earlier-mentioned input variables were selected. The response surface is utilized to extract utilization factors for each of the selected combinations. Only the highest value for each of the utilization factors was set in Table 7.8. The results show that glulam beams are utilized up to around 85% and 78% of their capacity as a result of the combined tension and bending, and the combined bending and compression, respectively. However, around 94% of the beams' capacity is utilized under buckling criteria.

The small differences between the results obtained from the different load cases suggest that the hydrostatic pressure that squeezes the glulam beams inside the floater plays an important role in utilizing the beam's capacity.

Table 7.8: Maximum utilization factors expected for each of the design loads

| DLC number | Wind condition | Glulam | | | | | Steel |
|---|---|---|---|---|---|---|---|
| | | $UF_{max,\ 1}$ | $UF_{max,\ 2}$ | $UF_{max,\ 3}$ | $UF_{max,\ 4}$ | $UF_{max,\ 5}$ | $UF_{max,\ 6}$ |
| 1 | | 0.7679 | 0.8175 | 0.7417 | 0.7548 | 0.9085 | 0.8153 |
| 2 | | 0.7855 | 0.8354 | 0.7718 | 0.7716 | 0.9281 | 0.8223 |
| 3 | | 0.7855 | 0.8355 | 0.7719 | 0.7716 | 0.9282 | 0.8223 |
| 4 | | 0.7856 | 0.8355 | 0.7719 | 0.7717 | 0.9282 | 0.8223 |
| 5 | | 0.7856 | 0.8356 | 0.7720 | 0.7717 | 0.9282 | 0.8223 |
| 6 | NTM | 0.7856 | 0.8356 | 0.7720 | 0.7717 | 0.9282 | 0.8223 |
| 7 | | 0.7866 | 0.8364 | 0.7730 | 0.7722 | 0.9291 | 0.8225 |
| 8 | | 0.7879 | 0.8378 | 0.7750 | 0.7735 | 0.9306 | 0.8231 |
| 9 | | 0.7882 | 0.8381 | 0.7756 | 0.7737 | 0.9310 | 0.8232 |
| 10 | | 0.7901 | 0.8404 | 0.7794 | 0.7751 | 0.9338 | 0.8242 |
| 11 | | 0.7908 | 0.8406 | 0.7793 | 0.7763 | 0.9339 | 0.8243 |
| 12 | | 0.7776 | 0.8280 | 0.7581 | 0.7633 | 0.9196 | 0.8194 |
| 13 | | 0.7880 | 0.8379 | 0.7752 | 0.7735 | 0.9307 | 0.8231 |
| 14 | | 0.7880 | 0.8379 | 0.7752 | 0.7735 | 0.9307 | 0.8231 |
| 15 | | 0.7882 | 0.8383 | 0.7758 | 0.7733 | 0.9312 | 0.8232 |
| 16 | | 0.7883 | 0.8382 | 0.7755 | 0.7736 | 0.9310 | 0.8232 |
| 17 | ETM | 0.7883 | 0.8382 | 0.7758 | 0.7738 | 0.9312 | 0.8233 |
| 18 | | 0.7885 | 0.8386 | 0.7765 | 0.7736 | 0.9317 | 0.8234 |
| 19 | | 0.7896 | 0.8400 | 0.7786 | 0.7745 | 0.9333 | 0.8240 |
| 20 | | 0.7897 | 0.8397 | 0.7778 | 0.7749 | 0.9328 | 0.8238 |
| 21 | | 0.7904 | 0.8402 | 0.7786 | 0.7759 | 0.9334 | 0.8241 |
| 22 | | 0.7914 | 0.8414 | 0.7805 | 0.7767 | 0.9349 | 0.8246 |
| 23 | | 0.7834 | 0.8331 | 0.7667 | 0.7690 | 0.9253 | 0.8213 |
| 24 | | 0.7841 | 0.8345 | 0.7688 | 0.7679 | 0.9272 | 0.8223 |
| 25 | | 0.7844 | 0.8347 | 0.7691 | 0.7682 | 0.9274 | 0.8223 |
| 26 | | 0.7853 | 0.8351 | 0.7704 | 0.7706 | 0.9276 | 0.8221 |
| 27 | | 0.7871 | 0.8372 | 0.7739 | 0.7718 | 0.9301 | 0.8229 |
| 28 | NTM | 0.7896 | 0.8384 | 0.7751 | 0.7767 | 0.9313 | 0.8236 |
| 29 | | 0.7907 | 0.8395 | 0.7773 | 0.7780 | 0.9325 | 0.8240 |
| 30 | | 0.7922 | 0.8412 | 0.7797 | 0.7787 | 0.9345 | 0.8247 |
| 31 | | 0.7926 | 0.8420 | 0.7807 | 0.7782 | 0.9353 | 0.8249 |
| 32 | | 0.7926 | 0.8420 | 0.7812 | 0.7785 | 0.9355 | 0.8250 |
| 33 | | 0.7943 | 0.8436 | 0.7834 | 0.7804 | 0.9372 | 0.8256 |

# Chapter 8- Conclusion & Discussion

## 8.1 Conclusion

This work presents a new hybrid timber-steel floating substructure for a 15 MW semisubmersible-type FWT in an effort to examine the possibility of using glulam in the construction of such platforms. A comprehensive design methodology was introduced, containing design basics, design standards, preliminary design selection, and fully coupled analysis. Detailed descriptions of all the design basis, requirements, loads, and criteria are provided. For the floater's pontoons, a comparison between three glulam-supported substructures that differ in layout and dimensions are presented using Ansys workbench 2020 R1. Based on the results of this comparison, configuration (b) was found to fulfill all 6 design criteria with minimal material mass. Therefore, it was selected to continue the study with. About 590 t of steel mass is saved using configuration (b) in comparison to the UMaine VolturnUS-S semisubmersible platform.

Based on the similarity in geometry, mass properties, CoG, and CoB, the hydrodynamic properties provided for the UMaine VolturnUS-S semisubmersible platform were used to perform a fully nonlinear aero-hydro-servo-elastic simulation. The simulation is carried out in the time domain by gluing together HydroDyn, AeroDyn, ElastoDyn, ServoDyn, inflowWind, and MoorDyn codes. Based on that, all platform inertia loads, hydrodynamic loads, tower loads, and mooring line tensions were extracted. RSM and parameter correlation analysis were utilized to reduce the overall computational time and to be able to determine worst-case load combinations (inputs) that yield maximum utilization factors (output) effectively. Results from the parameter correlation study showed a strong varying correlation between TwrBsFxt, TwrBsFzt, TwrBsMyt, FAIRTEN1, and FAIRTEN2 and the resulting utilization factors. Based on that, worst load combinations were identified to evaluate the performance of the new hybrid floater during normal and extreme operating conditions. The final results showed that all criteria were fulfilled with utilization factors that vary between 0.74-0.94.

The study carries original contributions to the floating wind energy development by:

- Investigating the main design criteria that must be considered when glulam is used in the construction of offshore platforms.
- Introducing a robust hybrid timber-steel design that passes the 6 design criteria determined in beforehand.

## 8.2 Future Work

The use of glulam in FWT is a new and young field, with great potential for improvement and innovation. Some of the many natural extensions to this work are suggested below:

**General structural design recommendations**

- Improve the layout of the floater pontoons according to the stress distribution shown in the figures in Appendix B. For example, the tension and bending stress on beams (criteria 1, and criteria 2) are maximum in the center part where all pontoons meet and decrease towards the radial columns. The same applies to the equivalent stress on plates. Based on that, trapezoid-like pontoons with a height that decrease towards the radial columns might be a better option than the current configuration.

- Improve the layout by having thicker steel plates at the bottom to account for the higher stress due to hydrostatic pressure.

- Improve the layout to include truss elements instead of beam elements to eliminate bending stress which is a main contributor to most design criteria. For this purpose, SolidWorks was used to illustrate how a glulam pinned joint looks like, see Figure 8.1

- Joints are especially important in timber construction, especially for the serviceability limit condition, and are often weaker than the beams/trusses being linked. Therefore, a more thorough examination is needed to find a joint design that can bear all load combinations. Other factors that must be considered during the design of the joint include cost efficiency, production process, visual appeal, and the preferences and erection technique of the involved structural engineers (Natterer et al., 1991).

- The buckling of the steel plates is another area that was not covered in this work but must be investigated.

**Design validation recommendations**

- To ensure the integrity of the FWT, it is necessary to check the design against the complete set of design load cases defined in IEC (IEC-61400-1, 2005).

- To validate the design, it is necessary to check the design for the other three remaining design limit states, namely Fatigue FLS, Serveciability SLS, and Accidental ALS limit states.

- Other aspects must also be considered such as the economic feasibility, the assembly procedure, and water-protection technologies to protect glulam beams.
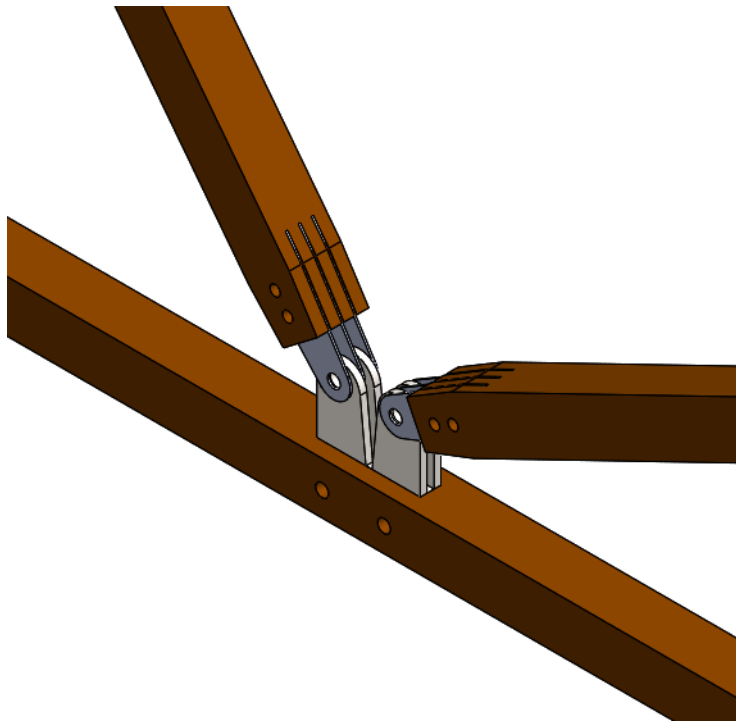
Figure 8.1: Pinned joint as a part of glulam truss frame (SolidWorks)

# References

Abrahamsen, R. (2017). Mjøstårnet-Construction of an 81 m tall timber building. *Internationales Holzbau-Forum IHF*.

Allen, C., Viscelli, A., Dagher, H., Goupee, A., Gaertner, E., Abbas, N., Hall, M., & Barter, G. (2020). *Definition of the UMaine VolturnUS-S reference platform developed for the IEA Wind 15-megawatt offshore reference wind turbine*.

Alvarez, A. C., & Fernandez, D. C. (2016). *Conceptual design and FE analysis of a CLT wind turbine tower*.

ANSYS. *DesignXplorer User's Guide* (19.3 Academic ed. ed.). ANSYS.

Bak, C., Zahle, F., Bitsche, R., Kim, T., Yde, A., Henriksen, L., Natarajan, A., & Hansen, M. (2013). Description of the DTU 10 MW reference wind turbine Tech. rep. *DTU Wind Energy*.

Blaß, H. J., & Sandhaas, C. (2017). *Timber engineering-principles for design*. KIT Scientific Publishing.

Bortolotti, P., Tarres, H. C., Dykes, K. L., Merz, K., Sethuraman, L., Verelst, D., & Zahle, F. (2019). *IEA Wind TCP Task 37: Systems engineering in wind energy-WP2. 1 Reference wind turbines*.

Box, G., & Wilson, K. (1951). On the experimental designs for exploring response surfaces. *Ann Math Stat*, *13*, 1-45.

Buchanan, A. (2007). Energy and CO2 advantages of wood for sustainable buildings. Institute of Professional Engineers Convention.

Bywaters, G., John, V., Lynch, J., Mattila, P., Norton, G., Stowell, J., Salata, M., Labath, O., Chertok, A., & Hablanian, D. (2004). Northern Power Systems WindPACT drive train alternative design study report. *NREL, Golden, Colorado, Report No. NREL/SR-500-35524*.

C.D. Smith Construction. (2021). *Mass Timber Construction*. https://www.cdsmith.com/mass-timber-construction

Chipindula, J., Botlaguduru, V. S. V., Du, H., Kommalapati, R. R., & Huque, Z. (2018). Life cycle environmental impact of onshore and offshore wind farms in Texas. *Sustainability*, *10*(6), 2022.

Colling, F. (1990). *Tragfähigkeit von Biegeträgern aus Brettschichtholz in Abhängigkeit von den festigkeitsrelevanten Einflussgrößen* (Reports of the Versuchsanstalt für Stahl, Holz und Steine of Karlsruhe University, Issue 22).

Crozier, A. (2011). *Design and Dynamic Modeling of the Support Structure for a 10 MW Offshore Wind Turbine* Norwegian University of Science and Technology (NTNU)]. Trondheim.

Desmond, C., Murphy, J., Blonk, L., & Haans, W. (2016). Description of an 8 MW reference wind turbine. Journal of Physics: Conference Series.

Det Norske Veritas (DNV). (2010a). DNV-RP-C201: Buckling Strength of Plated Structures. In. Norway.

Det Norske Veritas (DNV). (2010b). Recommended Practice DNV-RP-C205: Environmental Conditions and Environmental Loads. In.

Det Norske Veritas (DNV). (2011). DNV-OS-C101: Design of Offshore Steel Structures General (LRFD Method). In.

Det Norske Veritas (DNV). (2018). Offshore Standards; DNVGL-OS-E301: Position Mooring. In.

Det Norske Veritas DNV-GL. (2013). DNV-OS-J103: Design of Floating Wind Turbine Structures. In. Oslo.

Diamond, K. E. (2012). Extreme weather impacts on offshore wind turbines: lessons learned. *Nat. Resources & Env't*, *27*, 37.

Dowling, N. E. ( 2007). *Engineering Methods for Deformation, Fracture, and Fatigue* (3rd ed.). Pearson.

ETIPWind. ((2020). Floating offshore wind: delivering climate neutrality. https://etipwind.eu/files/reports/ETIPWind-floating-offshore-wind-factsheet.pdf

European Commission. (2019). *Communication from the Commission to the European Parliament, the European Council, the Council, the European Economic and Social Committee and the Committee of the Regions–The European Green Deal* (Document 52019DC0640, Issue.

European Commission. (2020). *Boosting Offshore Renewable Energy for a Climate Neutral Europe.*

European Commission. (2020a). *Communication from the Commission to the European Parliament, the Council, the European Economic and Social Committee and the Committee of the Regions - an EU Strategy to Harness the Potential of Offshore Renewable Energy for a Climate Neutral Future*.

European Commission. (2020b). *The EU Blue Economy Report*. https://op.europa.eu/it/publication-detail/-/publication/83843365-c18d-11ea-b3a4-01aa75ed71a1

European Commission. (2021). *Communication from the Commission to the European Parliament, the Council, the European Economic and Social Committee and the Committee of the Regions - on a New Approach for a Sustainable Blue Economy in the EU Transforming the EU's Blue Economy for a Sustainable Future*.

European Committee for Standardization CEN. (2006). Eurocode 5: Design of timber structures - Part 1-1: General -Common rules and rules for buildings. In. Brussels, Belgium.: EN.

European Committee for Standardization CEN. (2013). NS-EN 14080: 2013+ NA: 2016 Timber structures-Glued laminated timber and glued solid timber Requirements. In.

Faltinsen, O. (1993). *Sea loads on ships and offshore structures* (Vol. 1). Cambridge university press.

Frese, M. (2006). *Die Biegefestigkeit von Brettschichtholz aus Buche. Experimentelle und numerische Untersuchungen zum Laminierungseffekt* [Dissertation, Universität Karlsruhe (TH)].

Froeyd, L. (2009). *Control System on a Wind Turbine.* Norwegian University of Science and Technology (NTNU)]. Trondheim.

Gaertner, E., Rinker, J., Sethuraman, L., Zahle, F., Anderson, B., Barter, G. E., Abbas, N. J., Meng, F., Bortolotti, P., & Skrzypinski, W. (2020). *IEA wind TCP task 37: definition of the IEA 15-megawatt offshore reference wind turbine*.

Glulam Beams. *What is Glulam?* https://glulambeams.co.uk/about-glulam/what-is-glulam/

Griffith, D. T., & Ashwill, T. D. (2011). The Sandia 100-meter all-glass baseline wind turbine blade: SNL100-00. *Informe Técnico, Sandia National Laboratories*.

Guilford, J. P. (1950). Fundamental statistics in psychology and education.

Hall, M. (2015). MoorDyn user's guide. *Department of Mechanical Engineering, University of Maine: Orono, ME, USA*, *15*.

IEC-61400-1. (2005). IEC 61400-1: Wind Tubines - Part 1: Design Requirements. In: Geneva, Switzerland: IEC.

International Electrotechnical Commission (IEC). (2009). Wind Turbine Standard IEC-61400-3. In.

International Energy Agency (IEA). (2019). *Offshore Wind Outlook 2019*. https://www.iea.org/reports/offshore-wind-outlook-2019

Jonkman, B. (2016). Turbsim user's guide: Version 2.00. 00. *National Renewable Energy Laboratory (NREL): Golden, CO, USA*.

Jonkman, J., Butterfield, S., Musial, W., & Scott, G. (2009). *Definition of a 5-MW reference wind turbine for offshore system development*.

Jonkman, J., & Sclavounos, P. (2006). Development of fully coupled aeroelastic and hydrodynamic models for offshore wind turbines. 44th AIAA aerospace sciences meeting and exhibit.

Kettle, A. (2020). Storm Xaver over Europe in December 2013: Overview of energy impacts and North Sea events, Adv. Geosci., 54, 137–147. In.

Krogstad, P. A. (2010). *Aerodynamics lecture notes: TEP4545*

Maestrale. (2022). available at: https://maestrale.interreg-med.eu/ (Accessed March 17, 2023).

Manwell, J. F., McGowan, J. G., & Rogers, A. L. (2010). *Wind energy explained: theory, design and application*. John Wiley & Sons.

Meissner, G. (2013). *Correlation risk modeling and management: An applied guide including the Basel III correlation framework-with interactive models in Excel/VBA*. John Wiley & Sons.

Modvion. *Tower potential*. https://modvion.com/the-product/

Modvion. (29 April 2020). *The first wooden wind power tower has been erected in Sweden* https://modvion.com/news/the-first-wooden-wind-power-tower-has-been-erected-in-sweden/

National Renewable Energy Laboratory (NREL). *OpenFAST repository*. https://github.com/OpenFAST/openfast

National Renewable Energy Laboratory (NREL). (n.d.-a). *FAST forum*. https://wind.nrel.gov/forum/wind/viewforum.php?f=4&sid=f53aea05293a7ffb0d0fa40f1ad52caa

National Renewable Energy Laboratory (NREL). (n.d.-b). *OpenFAST Documentation*. Retrieved 12.04.2023 from https://openfast.readthedocs.io/en/dev/index.html

Natterer, J., Herzog, T., & Volz, M. (1991). Holzbau Atlas Zwei. *Auflage. Düsseldorf: Arbeitsgemeinschaft Holz eV*.

Newman, J. (1977). Marine Hydrodynamics, | The MIT Press. *Cambridge, MA*.

Obhrai, C. (2022). OFF610_Lecture 1 - Introduction to offshore wind power. In U. o. Stavanger (Ed.), *OFF610/OFF615*.

Pantusa, D., Francone, A., & Tomasicchio, G. R. (2020). Floating offshore renewable energy farms. A life-cycle cost analysis at Brindisi, Italy. *Energies*, *13*(22), 6150.

Pantusa, D., & Tomasicchio, G. (2019). Large-scale offshore wind production in the Mediterranean Sea. *Cogent Engineering*, *6*(1), 1661112.

Pearson, K. (1896). VII. Mathematical contributions to the theory of evolution.—III. Regression, heredity, and panmixia. *Philosophical Transactions of the Royal Society of London. Series A, containing papers of a mathematical or physical character*(187), 253-318.

Pearson, K. (1920). Notes on the history of correlation. *Biometrika*, *13*(1), 25-45.

Pedersen, D. M., & Askheim, H. (2021). *Implementation of seismic soil-structure interaction in OpenFAST and application to a 10MW offshore wind turbine on jacket structure* Norwegian University of Science and Technology (NTNU)].

Porteous, J., & Kermani, A. (2013). *Structural timber design to Eurocode 5*. John Wiley & Sons.

Pulselli, R., Maccanti, M., Bruno, M., Sabbetta, A., Neri, E., Patrizi, N., & Bastianoni, S. (2023). Benchmarking Marine Energy Technologies Through LCA: Offshore Floating Wind Farms in the Mediterranean. Front. *Perspectives for marine energy in the mediterranean area volume II*, *16648714*, 18.

Roach, K. L., Lackner, M. A., & Manwell, J. F. (2023). A New Methodology for Upscaling Semi-submersible Platforms for Floating Offshore Wind Turbines. *Wind Energy Science Discussions*, *2023*, 1-33.

Raadal, H. L., Vold, B. I., Myhr, A., & Nygaard, T. A. (2014). GHG emissions and energy performance of offshore wind power. *Renewable Energy*, *66*, 314-324.

Sacchi, R., Besseau, R., Pérez-López, P., & Blanc, I. (2019). Exploring technologically, temporally and geographically-sensitive life cycle inventories for wind turbines: A parameterized model for Denmark. *Renewable Energy*, *132*, 1238-1250.

Skotny, Ł. (2019). *Why is a Triangular Element Stiffer?* [www.enterfea.com](www.enterfea.com)

Staschus, K., Kielichowska, I., Lejarreta, A. V., Sijtsma, L., Ramaekers, L., Vree, B., Yeomans, G. R., Wouters, C., Lindroth, S., & Krönert, F. (2020). Study on the offshore grid potential in the Mediterranean region. *DOI*, *10*, 742284.

Stewart, G. M., Robertson, A., Jonkman, J., & Lackner, M. A. (2016). The creation of a comprehensive metocean data set for offshore wind turbine simulations. *Wind Energy*, *19*(6), 1151-1159.

Storaenso. (2022). *Stora Enso forms partnership with Voodin Blades to develop sustainable wind turbine blades from wood*. [https://www.storaenso.com/en/newsroom/press-releases/2022/11/stora-enso-forms-partnership-with-voodin-blades-to-develop-sustainable-wind-turbine-blades-from-wood](https://www.storaenso.com/en/newsroom/press-releases/2022/11/stora-enso-forms-partnership-with-voodin-blades-to-develop-sustainable-wind-turbine-blades-from-wood)

Studiengemeinschaft Holzleimbau e.V. (1998). Argumente für BS-Holz. Informationsblatt zum Brettschichtholz des Informationsdienstes Holz. In. Düsseldorf.

Van Der Tempel, J. (2006). Design of support structures for offshore wind turbines.

Viselli, A. M., Dagher, H. J., & Goupee, A. J. (2014). Volturnus 1: 8-Design and Testing of the first grid-connected offshore wind turbine in the USA. SNAME 19th Offshore Symposium.

Viselli, A. M., Goupee, A. J., & Dagher, H. J. (2015). Model test of a 1: 8-scale floating wind turbine offshore in the gulf of maine. *Journal of Offshore Mechanics and Arctic Engineering*, *137*(4).

Viselli, A. M., Goupee, A. J., Dagher, H. J., & Allen, C. K. (2016). Design and model confirmation of the intermediate scale VolturnUS floating wind turbine subjected to its extreme design conditions offshore Maine. *Wind Energy*, *19*(6), 1161-1177.

Wang, Q., Yu, Z., Ye, R., Lin, Z., & Tang, Y. (2019). An ordered curtailment strategy for offshore wind power under extreme weather conditions considering the resilience of the grid. *IEEE Access*, *7*, 54824-54833.

WindEurope. ( 2019). *Our energy, our future; How offshore wind will help Europe go carbon-neutral.*

WindEurope. ( 2021). *WindEurope Annual Statistics 2020.* https://windeurope.org/intelligence-platform/product/wind-energy-in-europe-2020-statistics-and-the-outlook-for-2021-2025/

World Steel Association. (2016). *Steel's contribution to a low carbon future and climate resilient societies*. World Steel Association.

Zhao, Z., Shi, W., Wang, W., Qi, S., & Li, X. (2021). Dynamic analysis of a novel semi-submersible platform for a 10 MW wind turbine in intermediate water depth. *Ocean Engineering*, *237*, 109688.

# Appendix A: Main Dimensions
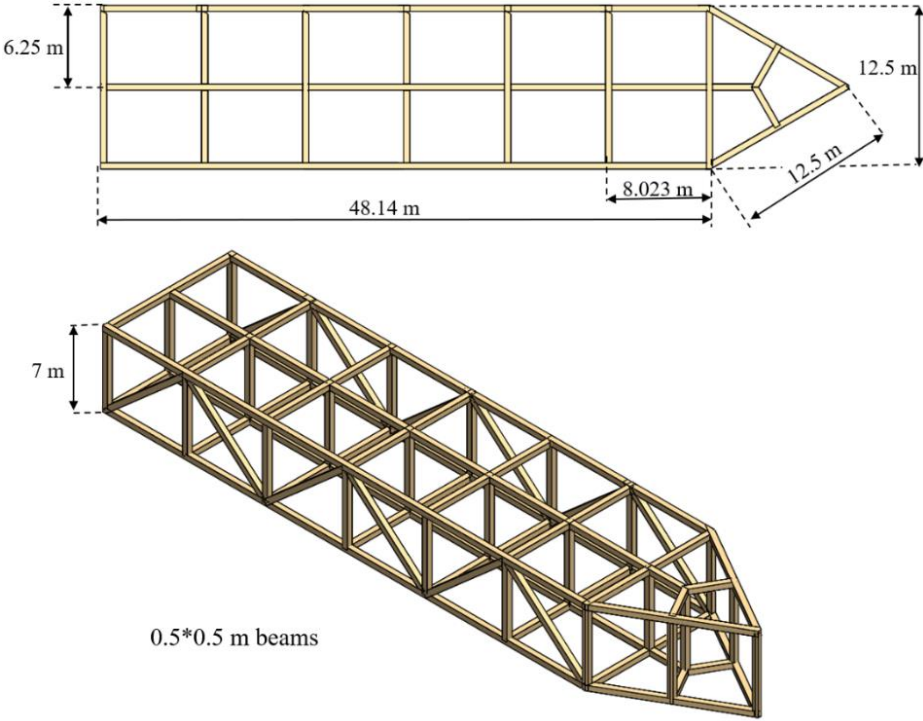


Configuration (a) main dimensions
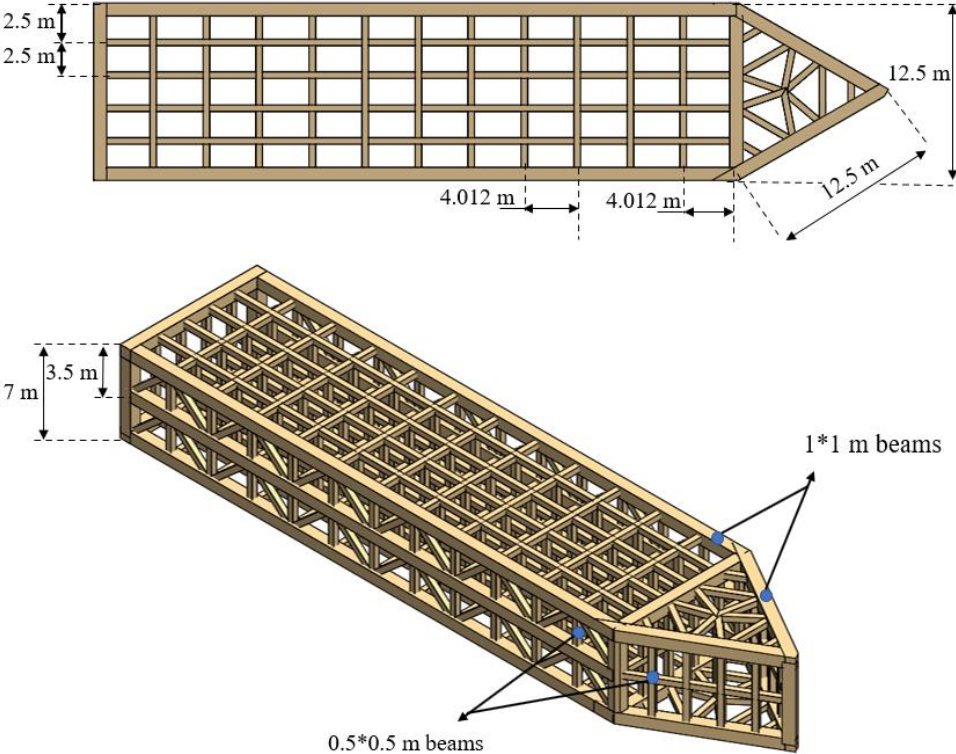


Configuration (b) main dimensions
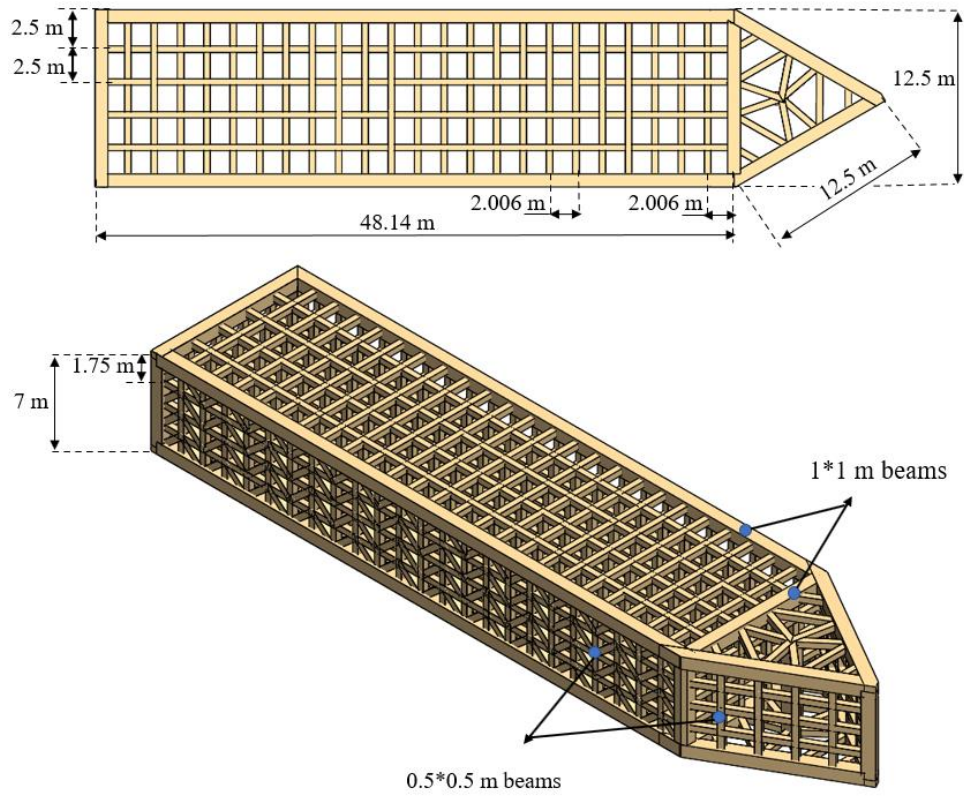
Configuration (c) main dimensions

# Appendix B: Results

Configuration (a)

| Combined bending and axial tension | |
|---|---|
| **Criteria 1**: $\left(\frac{\sigma_{t,0,d}}{f_{t,0,d}} + \frac{\sigma_{m,y,d}}{f_{m,y,d}} + k_m \cdot \frac{\sigma_{m,z,d}}{f_{m,z,d}}\right)$  | **Criteria 2**: $\left(\frac{\sigma_{t,0,d}}{f_{t,0,d}} + k_m \cdot \frac{\sigma_{m,y,d}}{f_{m,y,d}} + \frac{\sigma_{m,z,d}}{f_{m,z,d}}\right)$  |
| **Combined bending and axial compression** | |
| **Criteria 3**: $\left(\left(\frac{\sigma_{c,0,d}}{f_{c,0,d}}\right)^2 + \frac{\sigma_{m,y,d}}{f_{m,y,d}} + k_m \cdot \frac{\sigma_{m,z,d}}{f_{m,z,d}}\right)$  | **Criteria 4**: $\left(\left(\frac{\sigma_{c,0,d}}{f_{c,0,d}}\right)^2 + k_m \cdot \frac{\sigma_{m,y,d}}{f_{m,y,d}} + \frac{\sigma_{m,z,d}}{f_{m,z,d}}\right)$  |
| **Beam stability due to combined bending and compression** | **Yield of plates** |
| **Criteria 5**: $\left(\left(\frac{\sigma_{m,d}}{k_{crit} \cdot f_{m,d}}\right)^2 + \frac{\sigma_{c,0,d}}{k_{c,z} \cdot f_{c,0,d}}\right)$  | **Criteria 6**: $\left(\gamma_m \frac{\sqrt{\sigma_{x,d}^2 + \sigma_{y,d}^2 - \sigma_{x,d} \cdot \sigma_{y,d} + 3\tau_d^2}}{R_k}\right)$  |

Configuration (b)

## Combined bending and axial tension

**Criteria 1:** $\left(\dfrac{\sigma_{t,0,d}}{f_{t,0,d}} + \dfrac{\sigma_{m,y,d}}{f_{m,y,d}} + k_m \cdot \dfrac{\sigma_{m,z,d}}{f_{m,z,d}}\right)$

**Criteria 2:** $\left(\dfrac{\sigma_{t,0,d}}{f_{t,0,d}} + k_m \cdot \dfrac{\sigma_{m,y,d}}{f_{m,y,d}} + \dfrac{\sigma_{m,z,d}}{f_{m,z,d}}\right)$



## Combined bending and axial compression

**Criteria 3:** $\left(\left(\dfrac{\sigma_{c,0,d}}{f_{c,0,d}}\right)^2 + \dfrac{\sigma_{m,y,d}}{f_{m,y,d}} + k_m \cdot \dfrac{\sigma_{m,z,d}}{f_{m,z,d}}\right)$

**Criteria 4:** $\left(\left(\dfrac{\sigma_{c,0,d}}{f_{c,0,d}}\right)^2 + k_m \cdot \dfrac{\sigma_{m,y,d}}{f_{m,y,d}} + \dfrac{\sigma_{m,z,d}}{f_{m,z,d}}\right)$



## Beam stability due to combined bending and compression

**Criteria 5:** $\left(\left(\dfrac{\sigma_{m,d}}{k_{crit} \cdot f_{m,d}}\right)^2 + \dfrac{\sigma_{c,0,d}}{k_{c,z} \cdot f_{c,0,d}}\right)$

## Yield of plates

**Criteria 6:** $\left(\gamma_m \dfrac{\sqrt{\sigma_{x,d}^2 + \sigma_{y,d}^2 - \sigma_{x,d}.\sigma_{y,d} + 3\tau_d^2}}{R_k}\right)$

Configuration (c)

**Combined bending and axial tension**

**Criteria 1:** $\left(\frac{\sigma_{t,0,d}}{f_{t,0,d}} + \frac{\sigma_{m,y,d}}{f_{m,y,d}} + k_m \cdot \frac{\sigma_{m,z,d}}{f_{m,z,d}}\right)$

**Criteria 2:** $\left(\frac{\sigma_{t,0,d}}{f_{t,0,d}} + k_m \cdot \frac{\sigma_{m,y,d}}{f_{m,y,d}} + \frac{\sigma_{m,z,d}}{f_{m,z,d}}\right)$



**Combined bending and axial compression**

**Criteria 3:** $\left(\left(\frac{\sigma_{c,0,d}}{f_{c,0,d}}\right)^2 + \frac{\sigma_{m,y,d}}{f_{m,y,d}} + k_m \cdot \frac{\sigma_{m,z,d}}{f_{m,z,d}}\right)$

**Criteria 4:** $\left(\left(\frac{\sigma_{c,0,d}}{f_{c,0,d}}\right)^2 + k_m \cdot \frac{\sigma_{m,y,d}}{f_{m,y,d}} + \frac{\sigma_{m,z,d}}{f_{m,z,d}}\right)$



**Beam stability due to combined bending and compression**

**Criteria 5:** $\left(\left(\frac{\sigma_{m,d}}{k_{crit} \cdot f_{m,d}}\right)^2 + \frac{\sigma_{c,0,d}}{k_{c,z} \cdot f_{c,0,d}}\right)$

**Yield of plates**

**Criteria 6:** $\left(\gamma_m \frac{\sqrt{\sigma_{x,d}^2 + \sigma_{y,d}^2 - \sigma_{x,d} \cdot \sigma_{y,d} + 3\tau_d^2}}{R_k}\right)$

# Appendix C – Appended paper

A novel design of a hybrid glulam-steel substructure for the IEA 15-MW floating wind turbine

Hassan Hasan Yousef, Yihan Xing, Karan Sandipkumar Patel, Yucong Ma

# A novel design of a hybrid glulam-steel substructure for the IEA 15-MW floating wind turbine

**H H Yousef[1], Y Xing[1*], K S Patel[1] , and Y Ma[1]**

[1] University of Stavanger, Norway

[*] Yihan.xing@uis.no

**Abstract**. Wind energy has emerged as one of the most promising renewable energy sources. Furthermore, floating offshore wind turbines have enabled increased power generation in intermediate (45-150 m) and deep water (>150 m). However, the production, installation, and operation of wind turbines can produce considerable amounts of greenhouse gas emissions. This paper proposes a new hybrid glulam-steel floating substructure design for the IEA 15 MW floating wind turbine as an attempt to enhance the floating wind energy development with minimal cost and CO2 footprint. The new design aims to replace steel with glued laminated timber (glulam) and presents a modified version of the UMaine VolturnUS-S semisubmersible platform that was initially developed for the IEA 15 MW turbine. First, Ansys workbench 2020 R1 is utilized to assess and then choose amongst three preliminary hybrid timber-steel models based on a set of criteria gathered from relevant timber and steel standards. In comparison to the UMaine VolturnUS-S semisubmersible platform, the selected hybrid design saves about 590 t of steel mass. Following that, a fully coupled aero-hydro-servo-elastic dynamic study is performed using OpenFAST to validate the chosen model. Only the ultimate limit state design (ULS) under normal and extreme operating conditions is considered. The results reveal that the glulam supporting structure is a good load-bearing solution for the IEA 15 MW turbine, with a utilization factor ranging from 74 to 94%.

## 1. Introduction

Engineers will be able to accomplish the net-zero emission target by 2050 if they develop more efficient wind turbines [1]. Most wind turbines installed offshore are bottom-fixed monopile wind turbines. As 80% of wind turbines are found in waters deeper than 60m, the bottom fixed wind turbine is not economical [2] whereas floating offshore wind turbine (FOW) has an excellent advantage in deep waters. Floating wind turbines are designed to withstand extremely stochastic environmental loads for at least 20 years, according to International Electrotechnical Commission (IEC) specifications, see [3]. As the world shifts to renewable energy sources, more offshore wind farms are being built, necessitating the reduction of engineering, procurement, maintenance costs, and CO2 footprint.

According to [4], the Carbon Intensity of Electricity (CIE), which ranges from 26.1 to 78.7 CO2eq/kWh1 for a 6 MW raft-buoy wind turbine and a 6 MW spar buoy wind turbine, is found to be significantly dependent on the materials employed in both the manufacturing and maintenance procedures. The same study emphasizes the importance of creating new technologies to minimize the total steel mass to improve the turbine's environmental performance.

Glued laminated timber (glulam) is a strong, environmental-friendly, stable, and corrosion-resistant timber material that outperforms steel in many aspects including cost, strength-to-weight ratio, and

prefabrication possibility. Centuries of experience in shipbuilding and building industries provide us with more knowledge regarding joint selection, limitations, and faster processes to construct glulam with [5]. In 2019, the Mjøstårnet 18-storey building was completed to be the highest in the world which is made completely of glulam [6]. In 2020, Modvion erected a 30-m-tall wooden tower in Björkö (Sweden) [7]. Recently, two firms (Stora Enso, a biomaterials and wood building firm, and Voodin Blade Technology GmbH, a German startup manufacturing wind turbine rotor blades) began partnering to produce wooden wind turbine blades to replace heavier non-renewable wind turbine blades.

The aim of this paper is to propose a new hybrid glulam-steel substructure for the IEA 15 MW wind turbine semisubmersible-type, see Figure 1. The selection of IEA 15 MW is based on the fact that it is a reference wind turbine that provides a solution that is viable today and, in the future [8]. First, 3 different hybrid models are modeled and analysed using ANSYS Workbench 2020 R1. The three configurations are compared to find the best solution that provides acceptable utilization factors at minimal material mass. Following that, a fully coupled aero-hydro-servo-elastic dynamic analysis is performed using OpenFAST to validate the chosen model. Only the ultimate limit state (ULS) design for the turbine under extreme and typical operating circumstances is examined.
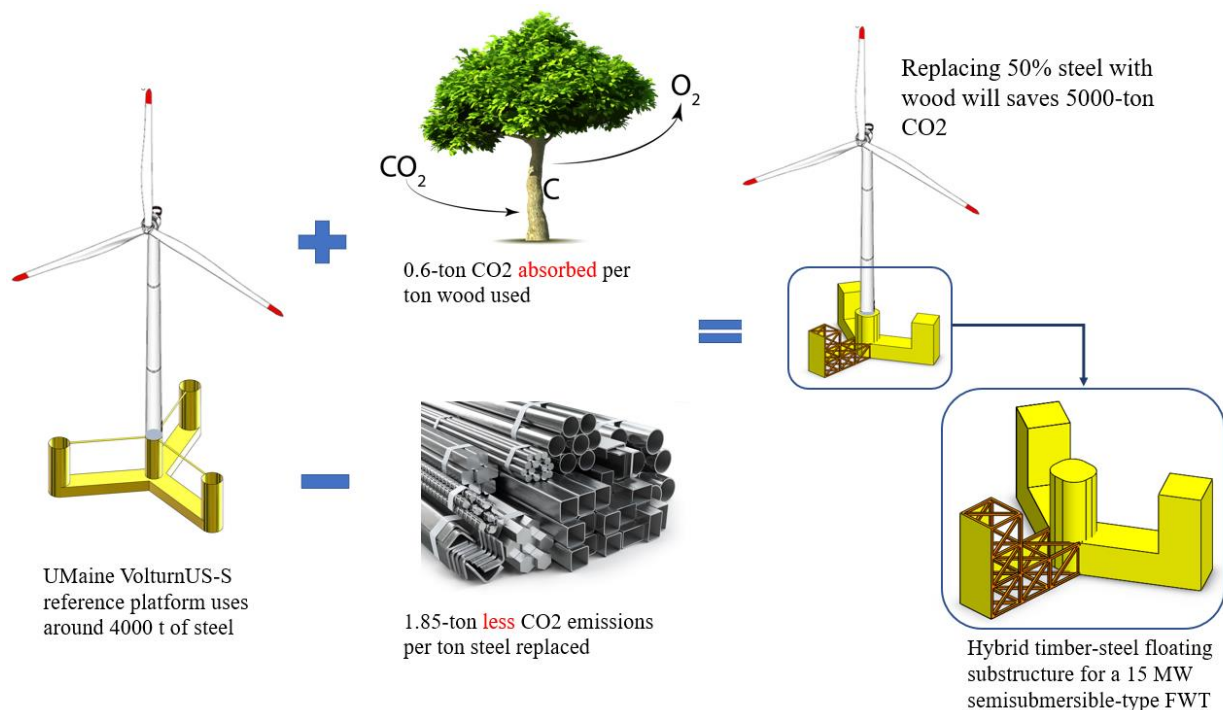


**Figure 1.** The environmental impact of using wood as a replacement for steel

## 2. System Description

The IEA 15-MW floating wind turbine (FWT) system [9] is used in this work. The FWT system will be expounded in two parts in the following sections. Firstly, the reference wind turbine will be described, then the properties of the original UMaine VolturnUS-S semisubmersible platform and the mooring system will be introduced.

### 2.1. IEA Wind 15-Megawatt reference FWT

In this paper, a 15-MW reference wind turbine (RWT) is used, the wind turbine was designed by International Electrotechnical Commission (IEC) Class 1B wind regime and is a conventional three-bladed, clockwise rotation-upwind turbine, equipped with a variable speed and collective pitch control system. The summary of the DTU 10-MW RWT is shown in Table 1.

**Table 1.** General parameters of IEA Wind 15-MW RWT (Allen et al., 2020; Gaertner et al., 2020)
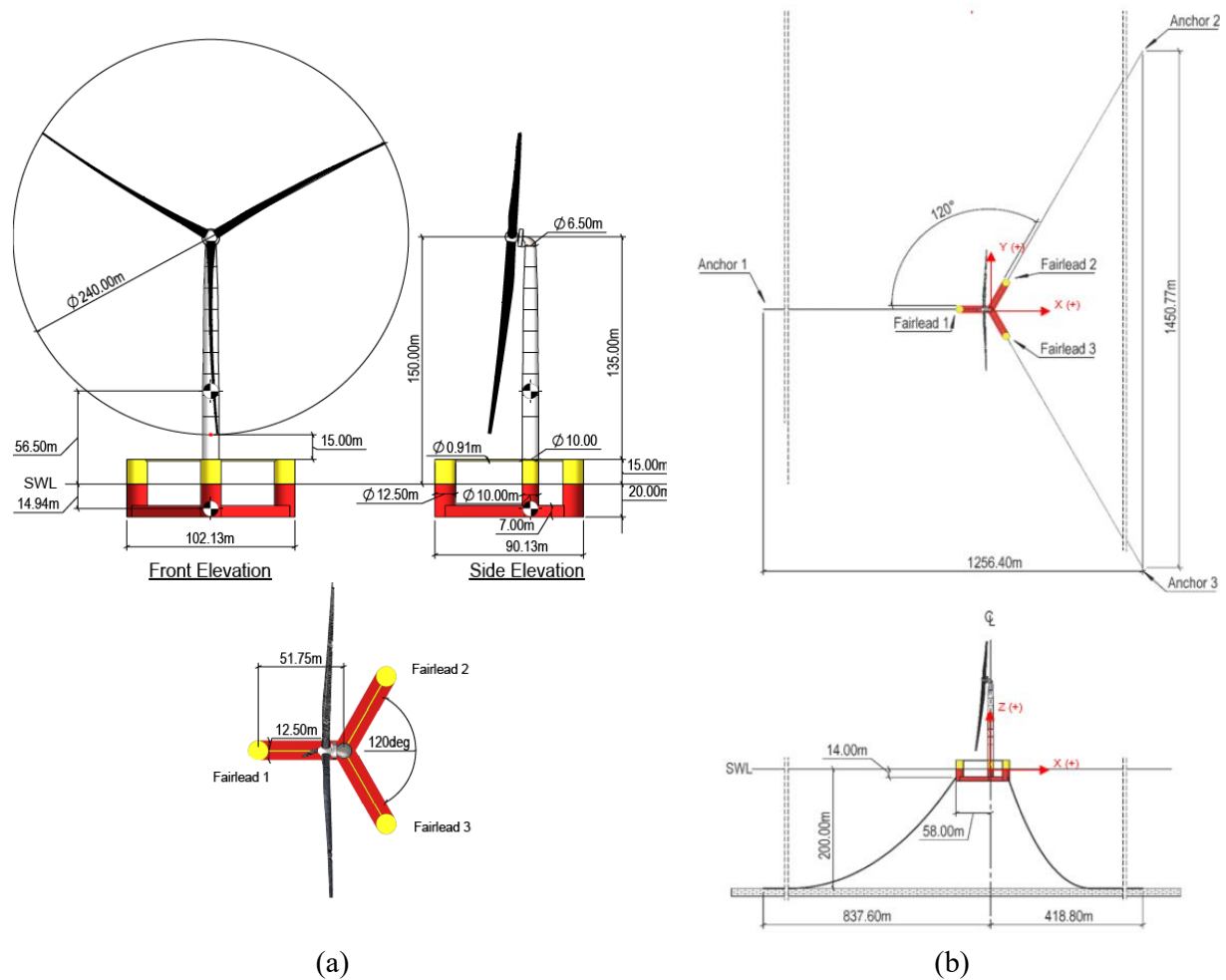
| Parameter | Value | Units |
|---|---|---|
| Power rating | 15 | MW |
| Rotor orientation, configuration | Upwind, 3 blades | - |
| Control | Variable speed, collective pitch | - |
| Drivetrain | Low-speed, direct drive | |
| Cut-in, rated, cut-out wind speed | 3, 10.59, 25 | m/s |
| Rotor, hub diameter | 240, 7.94 | m |
| Hub height | 150 | m |
| Design tip-speed ratio | 9 | - |
| Minimum rotor speed | 5 | rpm |
| Maximum rotor speed | 7.56 | rpm |
| Maximum tip speed | 95 | m/s |
| Water depth | 200 | m |
| Total system mass | 20,093 | t |
| Platform mass | 17,839 | t |
| Rotor nacelle assembly mass | 991 | t |
| Tower mass | 1,263 | t |
| Tower base diameter | 10 | m |

## 2.2. UMaine VolturnUS-S reference semisubmersible platform

This work utilizes the UMaine VolturnUS-S semi-submersible floating structure that is used to support the 15-MW RWT as a starting point to establish the new hybrid design. The floater comprises 3 columns that spread around a fourth central column. The columns are mounted on a star-shaped pontoon with a triangular cross-section at the bottom. The columns are also connected using three 0.9-m-diameter radial struts at the top. Three catenary mooring lines are used to maintain the floater in position, see Figure 2 (b). More details of the UMaine VolturnUS-S semi-floater and the mooring system are shown in Table 2 and Table 3, respectively.

**Table 2.** Semisubmersible Platform Properties (Allen et al., 2020)

| Parameter | Value | Units |
|---|---|---|
| Hull displacement | 20,206 | $m^3$ |
| Hull steel mass | 3,914 | t |
| Tower interface mass | 100 | t |
| Ballast mass (fixed/fluid) | 2,540/11,300 | t |
| Draft | 20 | m |
| Freeboard | 15 | m |
| Vertical center of gravity from SWL | -14.94 | m |
| Vertical center of buoyancy from SWL | -13.63 | m |
| Roll inertia about the center of gravity | 1.251E+10 | $Kg.\,m^2$ |
| Pitch inertia about the center of gravity | 1.251E+10 | $Kg.\,m^2$ |
| Yaw inertia about the center of gravity | 2.367E+10 | $Kg.\,m^2$ |

(a)                                                                                    (b)

**Figure 2.** (a) Main dimensions of the UMaine VolturnUS-S floater of the 15-MW wind turbine; (b) Sketch of the mooring system in the 15-MW FWT

**Table 3.** Mooring system's properties (Allen et al., 2020)

| Parameter | Value | Units |
|---|---|---|
| System type & number of lines | Chain Catenary & 3 Lines | - |
| Line type | Studless R3 Chain | - |
| Line breaking strength | 22.286 | kN |
| Fairlead depth | 14 | m |
| Dry line linear density | 685 | kg/m |
| Extensional stiffness | 3270 | MN |
| Line unstretched length | 850 | m |
| Fairlead pretension | 2,437 | kN |
| Fairlead angle from SWL | 56.4 | deg |

## 3. Finite Element Analysis of Three Concept Configurations

Three configurations are proposed for this work, see Figure 3. Since the floater is axisymmetric, the figure shows only the layout of the glulam supporting system for one pontoon and the central part where

all 3 pontoons meet. Each of the configurations has similar external dimensions to the UMaine platform, and the consists of 0.05 mm steel plates supported by different glulam supporting structures. More information regarding detailed dimensions is provided in Appendix A.



|  (a)  |  (b)  |  (c)  |
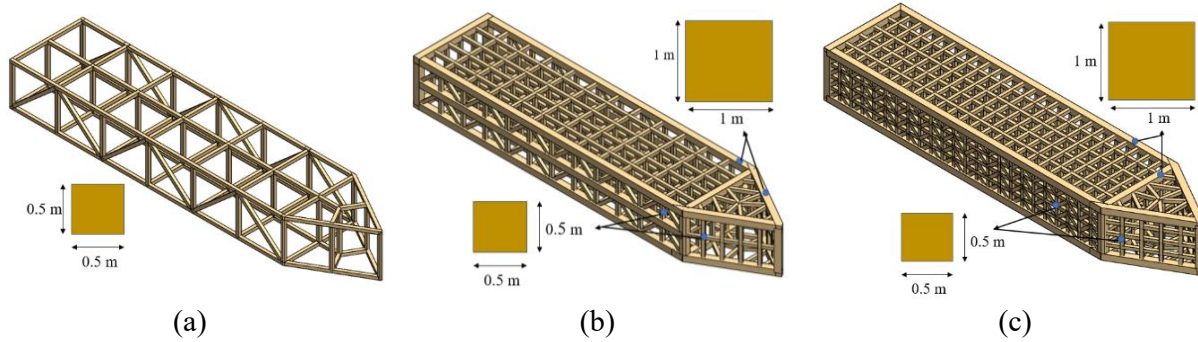
**Figure 3.** Glulam-based supporting structures for the three proposed configurations

### 3.1. Load and boundary conditions
To simplify the complexity of the design process, only the maximum aerodynamic load at rated wind velocity and hydrostatic pressure are considered. One pinned support was applied to one of the radial columns to simulate the behavior of the floater and allow for rotational motions only. Based on that, only the results obtained from the other two unsupported pontoons are valid. More information about loads and boundary conditions can be found in [10].

### 3.2. Material properties
Table 4 shows the material properties that were assigned for steel and glulam GL30h [11].

**Table 4.** Material properties of the plate's steel and glulam Gl30h assigned for the beams [11]

| Property | Glulam G30h for beams | Steel for plates | Unit |
|---|---|---|---|
| Density | 480 | 7850 | kg/m³ |
| Young's Modulus X(L) direction | 1.36E+10 |  | Pa |
| Young's Modulus Y(R) direction | 3E+08 | 2E+11 | Pa |
| Young's Modulus Z(T) direction | 3E+08 |  | Pa |
| Poisson's Ratio XY | 0.21 |  | - |
| Poisson's Ratio YZ | 0.21 | 0.3 | - |
| Poisson's Ratio XZ | 0.24 |  | - |
| Shear Modulus XY | 6.5E+08 |  | Pa |
| Shear Modulus YZ | 6.5E+08 | 7.692E+11 | Pa |
| Shear Modulus XZ | 6.5E+08 |  | Pa |
| Tensile Yield Strength | 2.4E+07 | 2.5E+08 | Pa |
| Compressive Yield Strength | 3E+07 | 2.5E+08 | Pa |

### 3.3. Mesh element type
For the meshing of each model, quadrilateral element types are used instead of triangular because of their ability to capture the geometry response accurately and to give a good representation of the actual deformation. Details regarding the type of the element used are provided in Table 5.

**Table 5.** Element type details

| Part | Element name IDs | Element shape |
|------|------------------|---------------|
| Plates | SHELL181 | QUAD4 |
| Beams | BEAM188 | BEAM3 |

*3.4. Design criteria*

To ensure the robustness of the hybrid design, the following criteria must be fulfilled:

- Glulam under combined bending and axial tension criteria [12]

**Criteria 1**
$$\frac{\sigma_{t,0,d}}{f_{t,0,d}} + \frac{\sigma_{m,y,d}}{f_{m,y,d}} + k_m \cdot \frac{\sigma_{m,z,d}}{f_{m,z,d}} \leq 1 \tag{1}$$

**Criteria 2**
$$\frac{\sigma_{t,0,d}}{f_{t,0,d}} + k_m \cdot \frac{\sigma_{m,y,d}}{f_{m,y,d}} + \frac{\sigma_{m,z,d}}{f_{m,z,d}} \leq 1 \tag{2}$$

$\sigma_{t,0,d}$ is the design tensile stress along the grain, $\sigma_{m,y,d}$ and $\sigma_{m,z,d}$ are the design bending stresses around the y and z axes, $f_{t,0,d}$ is the design tensile stress along the grain, $f_{m,y,d}$, and $f_{m,z,d}$ are the corresponding design bending strengths, and $k_m$ is a factor that makes allowance for the re-distribution of stresses and the effect of inhomogeneities of the material, and is 0.7 for glulam with a rectangular cross-section.

- Glulam under combined bending and axial compression criteria [12]

**Criteria 3**
$$\left(\frac{\sigma_{c,0,d}}{f_{c,0,d}}\right)^2 + \frac{\sigma_{m,y,d}}{f_{m,y,d}} + k_m \cdot \frac{\sigma_{m,z,d}}{f_{m,z,d}} \leq 1 \tag{3}$$

**Criteria 4**
$$\left(\frac{\sigma_{c,0,d}}{f_{c,0,d}}\right)^2 + k_m \cdot \frac{\sigma_{m,y,d}}{f_{m,y,d}} + \frac{\sigma_{m,z,d}}{f_{m,z,d}} \leq 1 \tag{4}$$

Where $\sigma_{c,0,d}$ is the design compressive stress along the grain, $f_{c,0,d}$ is the design's compressive strength along the grain.

- Glulam beam stability criteria [12]

**Criteria 5**
$$\left(\frac{\sigma_{m,d}}{k_{crit} \cdot f_{m,d}}\right)^2 + \frac{\sigma_{c,0,d}}{k_{c,z} \cdot f_{c,0,d}} \leq 1 \tag{5}$$

Where $\sigma_{m,d}$ is the design bending stress, $k_{crit}$ is a factor that considers the reduced bending strength due to lateral buckling, and $k_{c,z}$ is an instability factor. The values of $k_{crit}$ and $k_{c,z}$ can be calculated based on equations given in EN 1995-1-1 standard [12].

- Steel plates yielding criteria [13]

**Criteria 6**
$$\gamma_m \frac{\sigma_{j,d}}{R_k} \leq 1 \tag{6}$$

$\sigma_{j,d}$ is von Mises equivalent design stress, $R_k$ is the characteristic strength, and $\gamma_m = 1.15$ taken for plated structures.

In order to simplify the analysis of the design, only 6 output variables corresponding to the left side of each of the six design criteria are evaluated. The left side of each of the criteria represents the beam's utilization factor (UF).

Figure 4 shows the utilization factor according to the 1st criteria for configuration (b), while Table 6 presents a comparison between the maximum utilization factor for each configuration based on the above-mentioned criteria. The results show that configuration (b) provides an accepted utilization factor with minimal glulam mass. Therefore, all further results will be presented for configurations (b) only.
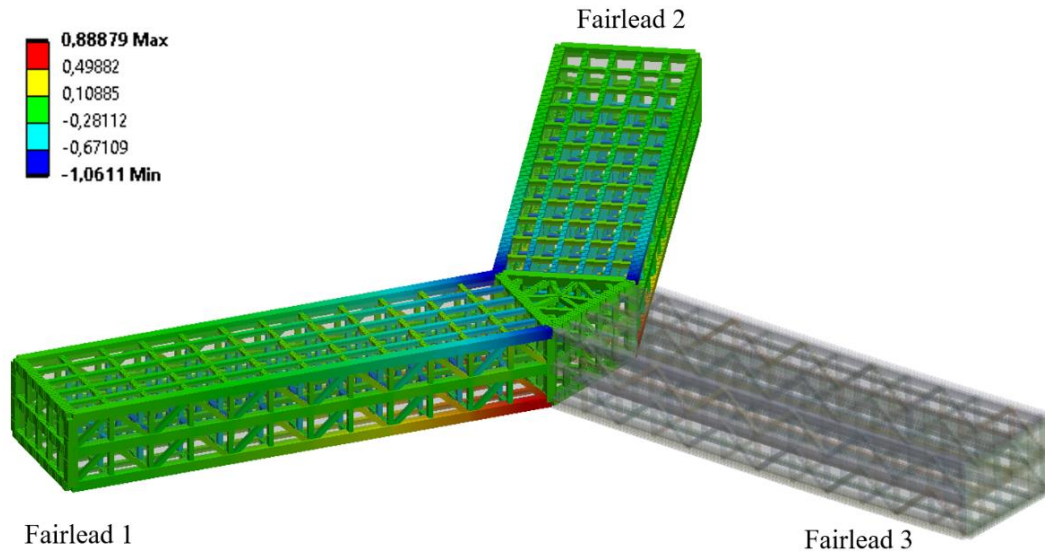


**Figure 4.** Utilization factor corresponding to the 1st combined bending and tension criteria for glulam, configuration (b)

**Table 6.** Max utilization factor for three hybrid configurations

| Material | Design criteria | Config. (a) | Config. (b) | Config. (c) |
|---|---|---|---|---|
| | $UF_{max, \, 1}$ | 1.03 | 0.75 | 0.76 |
| | $UF_{max, \, 2}$ | 1.04 | 0.80 | 0.82 |
| **Glulam** | $UF_{max, \, 3}$ | 5.63 | 0.90 | 0.94 |
| | $UF_{max, \, 4}$ | 5.36 | 0.90 | 0.94 |
| | $UF_{max, \, 5}$ | 1.13 | 0.89 | 0.88 |
| **Steel** | $UF_{max, \, 6}$ | 3.60 | 0.91 | 0.83 |

## 4. Hydro-Servo-Aero-Elastic analysis using OpenFAST

OpenFAST, an open-source simulation tool developed by the National Renewable Energy Laboratory (NREL), is utilized in this work for the fully coupled aero-hydro-elastic-servo dynamic analysis of the 15-MW FWT. The OpenFAST code couples together several computer codes such as AeroDyn [14], HydroDyn [15], ServoDyn, ElastoDyn, TurbSim, InflowWind, and MoorDyn [16], to account for the aerodynamic loads on rotor blades, hydrodynamic loads on floaters, control dynamics, structural dynamics, and mooring system dynamics.

According to Yousef [10], the hybrid floater has COB, COG, mass, and moments of inertia identical to the UMaine VolturnUS-S platform with a significant decrease in the mass of steel and concrete. Additionally, the hybrid floater's external dimensions and geometry are identical to those of the UMaine VolturnUS-S platform. Based on that, the requirements for stability and eigenfrequency are automatically satisfied, and the hydrodynamic properties, that are already provided for the UMaine VolturnUS-S platform [9], can be directly used for the analysis of the hybrid floater configuration (b).

### 4.1. Design load cases (DLC)

The performance of the hybrid floater is evaluated using a subset of IEC design load cases that presents the U.S. East Coast [17, 18]. All simulations were carried out for 720 sec assuming that both wind and wave are aligned at 0 degree, see Table 7.

**Table 7.** IEC Design load cases

|  | DLC number | Wind condition | $U_{hub}$ (m/s) | $H_s$ (m) | $T_p$ (sec) | Gamma shape factor |
|---|---|---|---|---|---|---|
| **1.1** | 1 | NTM | 4.00 | 1.10 | 8.52 | 1.00 |
|  | 2 |  | 24.00 | 4.52 | 9.45 | 1.89 |
| **1.3** | 3 | ETM | 4.00 | 1.10 | 8.52 | 1.00 |
|  | 4 |  | 24.00 | 4.52 | 9.45 | 1.89 |
| **1.6** | 5 | NTM | 4.00 | 6.30 | 11.50 | 2.75 |
|  | 6 |  | 24.00 | 9.80 | 14.10 | 2.75 |

Where ETM is the Extreme turbulence model and NTM is the Normal turbulence model.

Using OpenFAST, all the total time-varying loads on the tower base and mooring line tension such as TwrBsFxt, TwrBsFyt, TwrBsFzt, TwrBsMxt, TwrBsMyt, TwrBsMzt, FAIRTEN1, FAIRTEN2 are obtained.

## 5. Local Analysis

### 5.1. FEA Model

Using the results obtained from OpenFAST, model (b) is re-analyzed using the actual loads, see Figure 5.
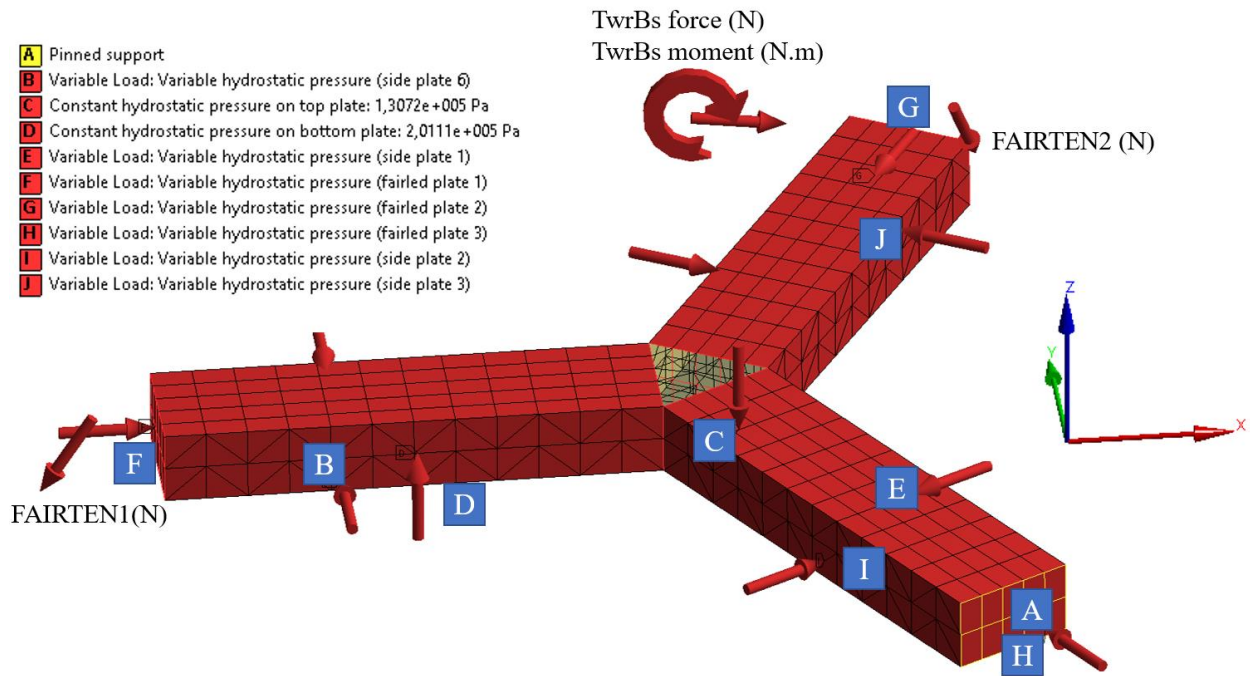
**Figure 5.** Actual loads acting on the hybrid design, configuration (b) (ANSYS)

## 5.2. Response Surface Methodology (RSM)

Response surface methodology (RSM) is a statistical method that can investigate the relationships between several inputs and one or more outputs based on mathematical regression. Response surface reduces the computational time by avoiding the need for running thousands of simulations based on the different load combinations (obtained at each time step $\Delta t$ during the simulation length).

### 5.2.1. Design of experiment (DoE)

In ANSYS Workbench, there are many approaches to generate experimental design points, such as the Box-Behnken design, central composite design, optimal space-filling design, etc. Only the central composite design is taken into consideration for this paper. A set of 285 design points is generated based on the upper and lower bound presented in Table 8.

**Table 8.** Upper and lower bounds assigned for input load variables

|  | TwrBsFxt | TwrBsFyt | TwrBsFzt | TwrBsMxt | TwrBsMyt | TwrBsMzt | FAIRTEN1 | FAIRTEN2 |
|---|---|---|---|---|---|---|---|---|
| **Lower bound** | -3E+06 | -2E+06 | -3E+07 | -8E+07 | -4E+08 | -4E+07 | 1E+06 | 1E+06 |
| **Upper bound** | 9E+06 | 2E+06 | 3E+07 | 2E+08 | 7E+08 | 4E+07 | 6E+06 | 3E+06 |

### 5.2.2. Construction of response surface

In ANSYS Workbench, the response surface can be built in a variety of ways, including Kriging, conventional second-order regression, non-parametric regression, etc. This paper uses generic aggregation to generate the response surface, which uses a genetic algorithm to simultaneously solve

many response surfaces while considering the stability and correctness of the response surface at the design point. Eq. (7) (ANSYS) provides the mathematical description of the generic aggregation approach.

$$\hat{y}_{ens}(x) = \sum_{i=1}^{N_m} w_i \cdot \hat{y}_i(x) \qquad (7)$$

Where $\hat{y}_{ens}$ is the ensemble prediction, $N_m$ is the total number of metamodels used and $\hat{y}_i$, $w_i$ are the prediction and weight factor of the $i-th$ response surface.

The results obtained from goodness of fit option available in ANSYS workbench show that the generated response surface provides a good fit to the model studied, see Table 9.

**Table 9.** Goodness of fit results

|  | $\text{UF}_{max,\ 1}$ | $\text{UF}_{max,\ 2}$ | $\text{UF}_{max,\ 3}$ | $\text{UF}_{max,\ 4}$ | $\text{UF}_{max,\ 5}$ | $\text{UF}_{max,\ 6}$ |
|---|---|---|---|---|---|---|
| Coefficient of Determination (best value=1) | | | | | | |
| Learning Points | 1 | 0.999 | 0.999 | 1 | 0.999 | 1 |
| Cross-Validation on Learning Points | 0.979 | 0.990 | 0.946 | 0.907 | 0.957 | 0.948 |
| Maximum Relative Residual (best value=0%) | | | | | | |
| Learning Points | 0 | 0.208 | 0.055 | 0 | 0.183 | 0 |
| Verification Points | 3.221 | 1.755 | 7.290 | 6.449 | 3.183 | 1.564 |
| Cross-Validation on Learning Points | 2.726 | 2.185 | 7.172 | 8.251 | 4.040 | 1.818 |
| Root Mean Square Error (best value=0) | | | | | | |
| Learning Points | 0 | 0 | 0 | 0 | 0 | 0 |
| Verification Points | 0.017 | 0.009 | 0.027 | 0.032 | 0.014 | 0.006 |
| Cross-Validation on Learning Points | 0.003 | 0.003 | 0.009 | 0.01 | 0.005 | 0.002 |
| Relative Root Mean Square Error (best value=0%) | | | | | | |
| Learning Points | 0 | 0.048 | 0.04 | 0 | 0.059 | 0 |
| Verification Points | 2.164 | 1.188 | 3.907 | 4.253 | 1.667 | 0.797 |
| Cross-Validation on Learning Points | 0.397 | 0.41 | 1.122 | 1.201 | 0.517 | 0.239 |

### 5.3. Parameter correlation study

The aim of the correlation study is to reduce the total computational time by detecting which of the inputs have the greatest influence on the output. This makes it possible to identify the worst-case load combinations while considering fewer inputs at their maximum/minimum values.

Results from the correlation study showed that the correlation coefficients between the load input variables and the output stress variables vary significantly based on the direction of each individual load [10]. However, the study highlighted that some inputs such as TwrBsFxt, TwrBsFzt, TwrBsMyt, FAIRTEN1, FAIRTEN1, and FAIRTEN2 have significant influence in the output, and must be considered during the process of selecting the worst-case load combinations, see [10].

*5.4. Results*

The maximum utilization factors for each of the design load cases are shown in Table 10 based on the worst-case load combinations. Each worst-case load combination corresponds to the maximum/minimum value for one of the input load variables. Then, the 6 utilization factors for each of the selected load combinations are extracted using the response surface. The results show that the utilization of glulam beams reaches up to 85% as a result of the combined bending and tension, and up to 78% as a result of combined bending and compression. However, the beams reach 94% of their capacity while resisting buckling.

**Table 10.** The maximum utilization factors expected for each of the design loads

| DLC number | Wind condition | Glued laminated timber | | | | | Steel |
|---|---|---|---|---|---|---|---|
| | | $UF_{max,\ 1}$ | $UF_{max,\ 2}$ | $UF_{max,\ 3}$ | $UF_{max,\ 4}$ | $UF_{max,\ 5}$ | $UF_{max,\ 6}$ |
| 1 | NTM | 0.7679 | 0.8175 | 0.7417 | 0.7548 | 0.9085 | 0.8153 |
| 2 | | 0.7908 | 0.8406 | 0.7793 | 0.7763 | 0.9339 | 0.8243 |
| 3 | ETM | 0.7776 | 0.8280 | 0.7581 | 0.7633 | 0.9196 | 0.8194 |
| 4 | | 0.7914 | 0.8414 | 0.7805 | 0.7767 | 0.9349 | 0.8246 |
| 5 | NTM | 0.7834 | 0.8331 | 0.7667 | 0.7690 | 0.9253 | 0.8213 |
| 6 | | 0.7943 | 0.8436 | 0.7834 | 0.7804 | 0.9372 | 0.8256 |

## 6. Conclusion

This paper presents a new hybrid timber-steel floating substructure for a 15 MW semisubmersible-type FWT. Based on a set of assumptions, A preliminary design study was conducted by modelling and comparing the 3 FE model using ANSYS Workbench 2020 R1. The results show that configuration (b) offers acceptable utilization factors with minimal glulam mass (cost). Furthermore, the selected hybrid design saves about 590 t of steel mass in comparison to the UMaine VolturnUS-S semisubmersible platform. Based on the similarity in geometry, mass properties, CoG, and CoB, the hydrodynamic properties provided for the UMaine VolturnUS-S semisubmersible platform [9] were utilized to perform a fully nonlinear aero-hydro-servo-elastic simulation of the hybrid model (b). Subsequently, Model (b) was re-analyzed using the actual loads produced by OpenFAST. Response surface methodology is then used to minimize the overall calculation time. To detect worst-case load combinations (inputs) that provide maximum utilization factors (outputs), a parameter correlation study was conducted. The parameter correlation study's findings revealed a substantial varying correlation between TwrBsFxt, TwrBsFzt, TwrBsMyt, FAIRTEN1, FAIRTEN1, FAIRTEN2, and the resulting utilization factors. The final results show that glulam can offer a good alternative for structural steel for IEA 15 MW with a utilization factor that varies between 0.74-0.94 for the different criteria under normal and extreme operating conditions. The insignificant difference in the utilization factor values among the different DLC emphasizes the importance of hydrostatic pressure as a design-driving load.

**Reference**
[1]     I. E. Agency, "World energy outlook 2020. OECD Publishing," 2020.
[2]     WindEurope, *Floating offshore wind energy-a policy blueprint for europe floating offshore wind energy* 2018.
[3]     J. Igba, K. Alemzadeh, C. Durugbo, and K. Henningsen, "Performance assessment of wind turbine gearboxes using in-service data: Current approaches and future trends," *Renewable and Sustainable Energy Reviews,* vol. 50, pp. 144-159, 2015-10-01, 2015.

[4]     R. Pulselli, M. Maccanti, M. Bruno, A. Sabbetta, E. Neri, N. Patrizi, and S. Bastianoni, "Benchmarking Marine Energy Technologies Through LCA: Offshore Floating Wind Farms in the Mediterranean. Front," *Perspectives for marine energy in the mediterranean area volume II,* vol. 16648714, pp. 18, 2023.

[5]     J. Porteous, and A. Kermani, *Structural timber design to Eurocode 5*: John Wiley & Sons, 2013.

[6]     R. Abrahamsen, "Mjøstårnet-Construction of an 81 m tall timber building."

[7]     Modvion, "The first wooden wind power tower has been erected in Sweden," 29 April 2020.

[8]     E. Gaertner, J. Rinker, L. Sethuraman, F. Zahle, B. Anderson, G. E. Barter, N. J. Abbas, F. Meng, P. Bortolotti, and W. Skrzypinski, *IEA wind TCP task 37: definition of the IEA 15-megawatt offshore reference wind turbine*, National Renewable Energy Lab.(NREL), Golden, CO (United States), 2020.

[9]     C. Allen, A. Viscelli, H. Dagher, A. Goupee, E. Gaertner, N. Abbas, M. Hall, and G. Barter, *Definition of the UMaine VolturnUS-S reference platform developed for the IEA Wind 15-megawatt offshore reference wind turbine*, National Renewable Energy Lab.(NREL), Golden, CO (United States); Univ. of …, 2020.

[10]    H. H. Yousef, "Design and analysis of a hybrid timber-steel floating substructure for a 15 MW semisubmersible-type FWT," 2023.

[11]    European Committee for Standardization CEN, "NS-EN 14080: 2013+ NA: 2016 Timber structures-Glued laminated timber and glued solid timber Requirements," 2013.

[12]    European Committee for Standardization CEN, "Eurocode 5: Design of timber structures - Part 1-1: General -Common rules and rules for buildings," EN, 2006.

[13]    Det Norske Veritas (DNV), "DNV-OS-C101: Design of Offshore Steel Structures General (LRFD Method)," 2011.

[14]    P. J. Moriarty, and A. C. Hansen, *AeroDyn Theory Manual,* NREL/TP-500-36881, National Renewable Energy Lab., Golden, CO (US), 2005.

[15]    National Renewable Energy Laboratory (NREL). "OpenFAST Documentation," 12.04.2023; https://openfast.readthedocs.io/en/dev/index.html.

[16]    M. Hall, "MoorDyn user's guide," *Department of Mechanical Engineering, University of Maine: Orono, ME, USA,* vol. 15, 2015.

[17]    A. M. Viselli, A. J. Goupee, and H. J. Dagher, "Model test of a 1: 8-scale floating wind turbine offshore in the gulf of maine," *Journal of Offshore Mechanics and Arctic Engineering,* vol. 137, no. 4, 2015.

[18]    G. M. Stewart, A. Robertson, J. Jonkman, and M. A. Lackner, "The creation of a comprehensive metocean data set for offshore wind turbine simulations," *Wind Energy,* vol. 19, no. 6, pp. 1151-1159, 2016.